Impurity Behavior and Weld Joint Properties of Low Activation Vanadium Alloys for Fusion Reactor

NAM-JIN HEO

DOCTOR OF PHILOSPHY

Department of Fusion Science

School of Mathematical and Physical Science

The Graduate University for Advanced Studies

2003

Impurity Behavior and Weld Joint Properties of Low Activation Vanadium Alloys for Fusion Reactor

By

NAM-JIN HEO

Department of Fusion Science

School of Mathematical and Physical Science

The Graduate University for Advanced Studies

CONTENTS

CHAPTER 1. INTRODUCTION

1-1. Requirements of a fusion reactor ····· 2
1-2. Fusion reaction and structural materials ····· 4
1-3. Candidate structural materials for a fusion reactor ····· 7
1-4. Status of the research for vanadium alloys ····· 13
1-4-1. Manufacture of the large heats ····· 13
1-4-2. Welding/Joint technology ····· 21
1-5. Objectives of the present study ····· 27

CHAPTER 2. EFFECT OF IMPURITIES ON THE RECRYSTALLIZATION AND THE PRECIPITATION BEHAVIOR

2-1. Behavior of recrystallization and precipitation in vanadium alloys after cold rolling ····· 29
2-1-1. Experimental procedures ····· 29
2-1-2. Effect of the heat treatment temperatures ····· 29
2-1-3. Discussions: Optimum heat treatment temperature for cold-rolled vanadium alloys ····· 41
2-1-4. Summary ····· 42

2-2. Effect of the impurity level on the precipitation behavior ····· 44
2-2-1. Preparation of the model alloys with the various oxygen and nitrogen levels ····· 44
2-2-2. Effect of the annealing temperature on hardness change and microstructural developments ····· 46
2-2-3. Discussions: Impurity behavior in V-4Cr-4Ti alloys ····· 57
2-2-4. Summaries ····· 59

2-3. Summary of the impurity behavior in vanadium alloys ····· 60

CHAPTER 3. ESTABLISHMENT OF THE WELDING TECHNOLOGY FOR VANADIUM ALLOYS USING YAG LASER

3-1. Development of the laser welding technology for pure vanadium and its alloys 64
3-1-1. Control of welding environments ····· 64
3-1-2. Effect of environmental control on the contaminations during the welding 66
3-1-3. Discussions: Estimations on the contamination with impurities during the welding process ····· 74
3-1-4. Summary ····· 76

3-2. Estimation of the mechanical properties of the weldments ····· 77
3-2-1. Bead appearances with welding parameters ····· 77
3-2-2. Impurity behavior in the weld zone ····· 83
3-2-3. Effect of the input power on the mechanical properties of the weld metal · 86
3-2-4. Discussions ····· 91
3-2-5. Summary ····· 93

CHAPTER 4. CONCLUSIONS
4-1. Impurity behavior ····· 95
4-2 Development of the high-grade laser welding technology ····· 96
REFERENCES ····· 97
PAPERS
PRESENTATIONS
ACKNOWLEDGES

CHAPTER1

Introduction

1-1. Requirements of a fusion reactor

It is recognized that the world energy demand will keep increasing, and the world will face the energy shortage in the near future. Fig. 1-1 shows energy demand scenario based on IPCC IS92a [1]. This is modeled and calculated in using LDNE21 [2] (Linearized Dynamic New Earth 21) model. This model includes various energy supply and CO_2 mitigation technologies. The energy flow is also taken into account of production of primary and secondary liquid energies (hydrogen/methanol and CO_2 recoveries/sequestrations), world trades/transportations of energy goods, energy conversions (chemical plants and electricity generations), and energy conservation in end-use sectors.

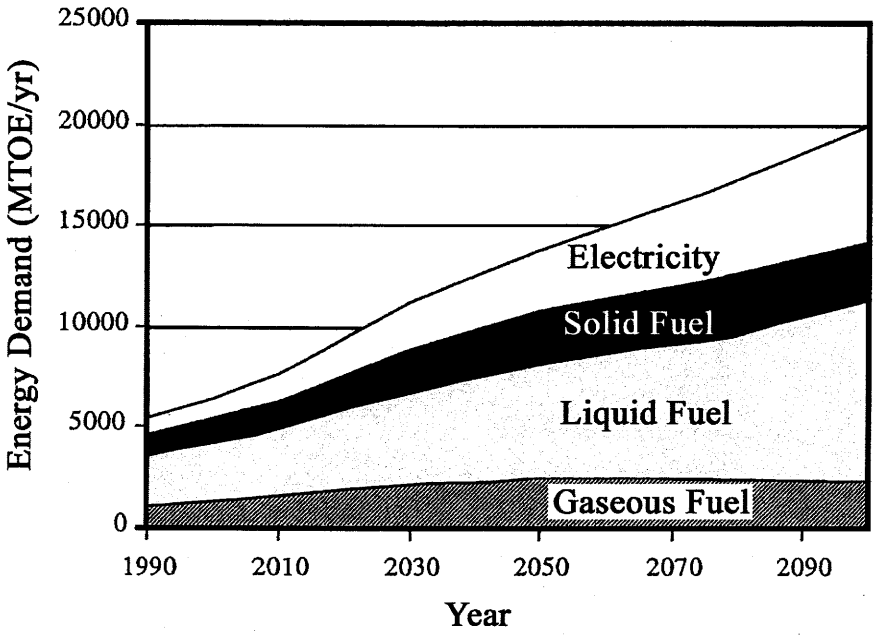

Fig. 1-1 Energy demand scenario [1].

Up to now Energy production is primarily based on fossil fuels (oil, coal and gas). The fossil fuels, such as coal, oil and natural gas, have some limited deposits. The fossil fuel supply will be exhausted in the future. However, their use will preferably be reduced before this time because of air pollution and discharge of CO_2, resulting in the global warming. Chemical power plants to the Annex-I countries face two constraints:

one is Kyoto COP3 Protocol at 2010 year, and the other is 20% CO_2 reduction to 1990-year-level CO_2 emission after 2020 year [3].

In this century the world will face the need for new energy sources. Both rules of the cheap and stable energy supply, and the preservation of environment will be required for new power plants. In other words, it is necessary to supply the enough energy cheaply and safely without a shortage of raw materials and without significant detrimental effects on the environments.

A hydraulic, geothermal and solar energy power plant is thought to be alternative energy sources in the near future. Their possibility of supply was already certified technologically. In the cases of a hydraulic power plant and a geothermal power plant, their detrimental effects on the environments are thought to be small. Solar energy power system is an attractive future energy source, but the cost, the stability of the supply and the necessary technical progress for its escalation are the remaining issues. Renewable energy sources (solar, wind and wave power, hydraulic power, biological fuels and geothermical power) cannot replace the fossil fuels on their own because of their limiting total energy supply, but are mainly of local use due to their regional dependence. Now fission power generations are in large fraction of the power sources. They do not have significant environmental effects such as air pollution and CO_2 generation. However, their safety in performance and the disposal of high level radioactive waste are critical.

Fusion reactors are one of the most attractive long term energy sources. Key features of fusion reactor relate primarily to potential advantages associated with safety and environmental considerations and exhaustless supply of fuel.

A model calculation using LDNE21 showed that we will obtain the benefits of reduced annual energy system cost and mitigated carbon tax (shadow price of carbon) under the CO2 concentration constraint by introducing the fusion energy in middle of 21^{st} century [4]. For realization of the fusion energy, however, both scientific and technological progress is crucial.

1-2. Fusion reaction and structural materials

The first generation of fusion power plants will use the D-T fusion reaction, shown schematically in Fig. 1-2. Nuclei of two isotopes of hydrogen, **deuterium** (D) and **tritium** (T) react to produce a **helium** (He) nucleus and a **neutron** (n). In each reaction, 17.6 MeV of energy (2.8 pJ) is released.

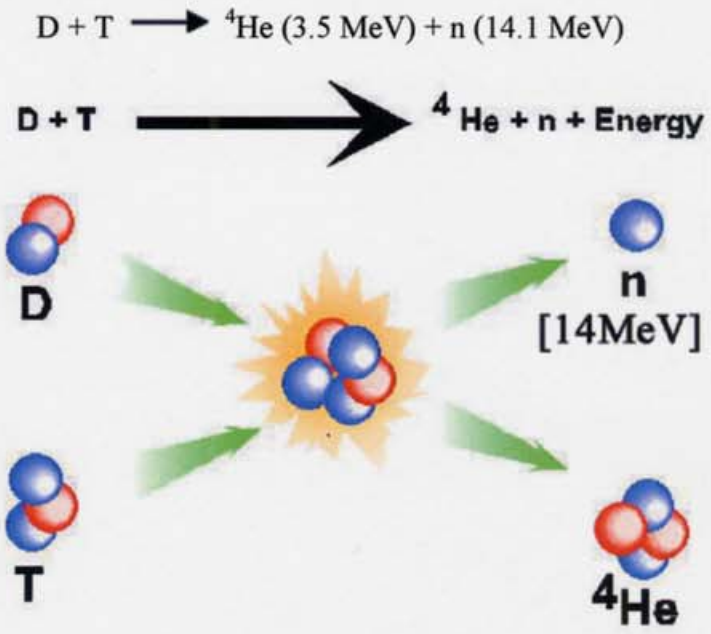

Fig. 1-2 Schematic drawing of a D-T fusion reaction.

A D-T reactor will experience unprecedented neutron radiation damage. Especially, the first wall and blanket structural materials will be exposed under high 14MeV neutron flux and thermal stress. The neutron irradiation can cause large changes in the properties of structural materials. At low temperatures, the main concern is radiation hardening and embrittlement. At higher temperature, there is a phenomenon called radiation creep, which exceeds the thermal creep and can limit the amount of stress that is allowed to be applied to the structure. Volumetric swelling is also a significant concern for certain materials at intermediate temperatures. At very high temperatures, there can be pronounced helium embrittlement.

As in most power generations, the operating limits of structural materials result in a primary constraint to the performance of fusion reactors. High-performance fusion

power reactors will be required to be an economically competitive energy generation. Important factors related to high performance structural materials include high temperature operation, a large operating window and a long operating lifetime. The structural materials should be safe under accidental conditions, environmentally friendly, and able to resist radiation damage. For high performance and safe operation, which is required to be economically competitive with fossil and nuclear power plants and acceptable to the public, the structural components must be made of low activation materials, which will either be activated to lower levels or reduce their activity quickly after the neutron irradiation. The materials will also be subject to high flux of particles and heat. Since high operating temperatures with repeated applied stress will cause the thermal creep and fatigue, the structural materials need to have a high resistance to the thermal creep and fatigue.

A wide range of structural materials have already been investigated for ITER [5-6] and DEMO [7-9]. Table 1-1 indicates the list of the common structural materials [10-11]. They includes conventional materials (austenitic stainless steels, copper alloys, titanium alloys and nickel base alloys), low activation structural materials (ferritic/martensitic steels including Oxide-Dispersive-Strengthened (ODS) steels, vanadium alloys, and ceramic composites). Recently, high temperature refractory metal alloys (Cr, Nb, Ta, Mo and W alloys) have been added to the candidate structural materials [10, 12]. However, the discussion on the selection criteria for structural materials needs careful analyses of the system requirements, including

(i) material availability, cost, fabricability, joining technology
(ii) unirradiated mechanical and thermophysical properties
(iii) operating temperature limits
(iv) radiation resistance
(v) nuclear properties (low activation)
(vi) high heat flux capability
(vii) chemical compatibility and corrosion properties

There are only a few structural materials that can potentially satisfy the criteria. The present candidates under investigation are ferritic/martensitic steel, vanadium-based alloys, and SiC/ SiC composites. Their properties will be discussed in details in the following sections.

Table 1-1 Common structural materials with examples of their applications [10-11]

Category	Example of materials	Present or projected application examples
Aluminum alloys	2014, 2024, 6061	Pool type reactor vessels, aeronautics
Copper alloys	CuCrZr, DS-Cu	ITER heat sink and divertor
Titanium alloys	Ti-6Al-4V	ITER and aeronautics
F/M steels	F82H, JLF, Eurofer	ITBM, DEMO
ODS steels	Fe-Y_2O_3	FBR, fusion
Stainless steels	316, 304, 321	ITER, LWR and LMFBR
Nickel base alloys	In. 718, 625, 623	ITER, HTGR
Superalloys	Hastalloys, Haynes series	Aerospace, space reactors
Vanadium alloys	V-4Cr-4Ti	DEMO, FPR
Molybdenum alloys	Mo, TZM, Mo-Re	Aerospace, space reactors
Niobium alloys	Cb275, FS85, Nb-1%Zr	Aerospace, nuclear industry
Tantalum alloys	Ta-8W-2Hf	Space reactors
Tungsten alloys	W, W-Re, W-THO_2	ITER
Ceramic composites	SiC/SiC, CFC	Fusion and aeronautics

1-3. Candidate structural materials for a fusion reactor

(i) Operation window of the candidate materials

Performance temperature limits for the materials will be in most cases determined by the thermal creep rate and the degradation of properties as a function of the neutron irradiation fluence. Fig. 1-3 shows the radiation properties of SS 316 and its design window [13]. In unirradiated conditions, type SS 316LN, selected as a structural material for international thermonuclear experimental reactor (ITER), is very ductile and maintains its high ductility and toughness even after prolonged aging. However, when irradiated at low temperatures in the range of 200-300 °C, its ductility and toughness decrease with increasing irradiation dose. At about 500 °C, the change in the mechanical properties is small, but void swelling occurs significantly with the increase in the neutron wall loading by above 1 MW/m^2, as shown in Fig. 1-3. As a result the design window of the SS316 is very limited as shown in Fig. 1-3.

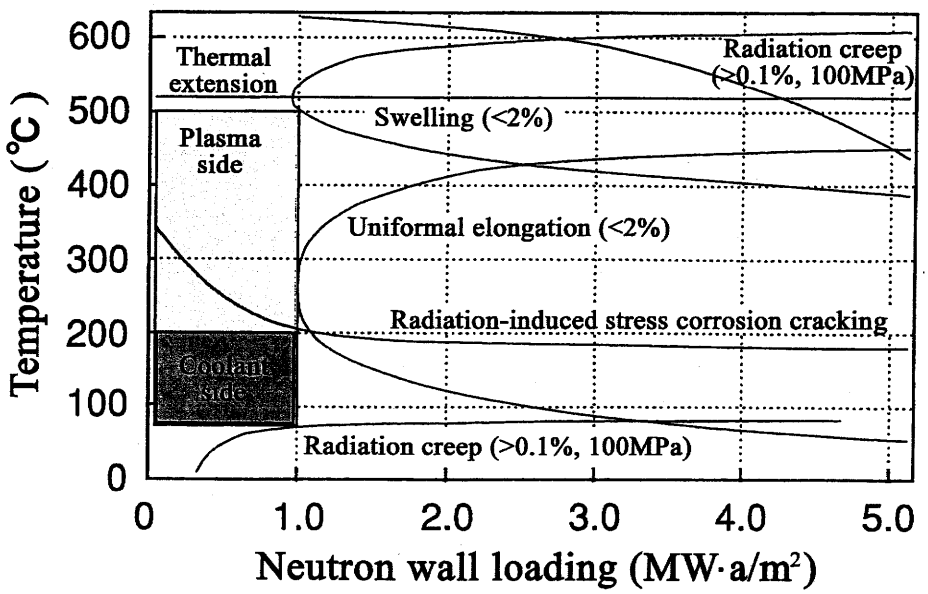

Fig. 1-3 Radiative properties and design window of SS 316 [13].

There is the impact of low activation material on fusion reactor design: to reduce radioactive impact to the environment in case of severe accident, to reduce decay heat in case of loss of cooling accident, to reduce gamma-ray dose during the maintenance and

to reduce the amount and lower the level of radioactive waste. SS316 cannot fulfill these low activation criteria. For ITER, it is expected that the neutron wall loading on the first wall is about 1 MW/m^2. For DEMO and commercial reactors, however, the neutron wall loading will be much higher than that for the ITER and the low activation requirement will be crucial [14]. Therefore, SS316 cannot be used as structural materials for DEMO and commercial reactors. In order to the demand of high performance and safe operation, the structural materials must be made of advanced low activation materials.

Attention to the first wall and blanket component materials for advanced fusion systems is being focused on high temperature materials, including F/M and ODS steels, vanadium alloys and SiC/SiC, as primary candidate structural materials [15-16].

Fig. 1-4 shows the radiation properties and design windows of the three candidate materials [17]. In the cases of body-centered cube (BCC), including ferritic steels and vanadium alloys, lower temperature limits will be determined by radiation hardening and embrittlement, and upper temperature limits will be determined by thermal creep, helium embrittlement, chemical compatibility, etc. In BCC radiation hardening at low temperatures resulted in increase in the ductile to brittle transition temperature (DBTT) [18-21]. To improve the performance limits in vanadium alloys, it will be significantly effective to decrease in impurity level, because the pickup of impurities leads to the degradation properties [22-24].

On the other hand, the lower operating temperature limit for SiC/SiC composites will be determined by degradation of the thermal conductivity, and the upper operating temperature will be determined by void swelling or chemical compatibility, as shown in Fig. 1-4. Major blanket concepts and their performance temperature limits for three candidate structural materials were summarized in Table 1-2 [11, 25-26].

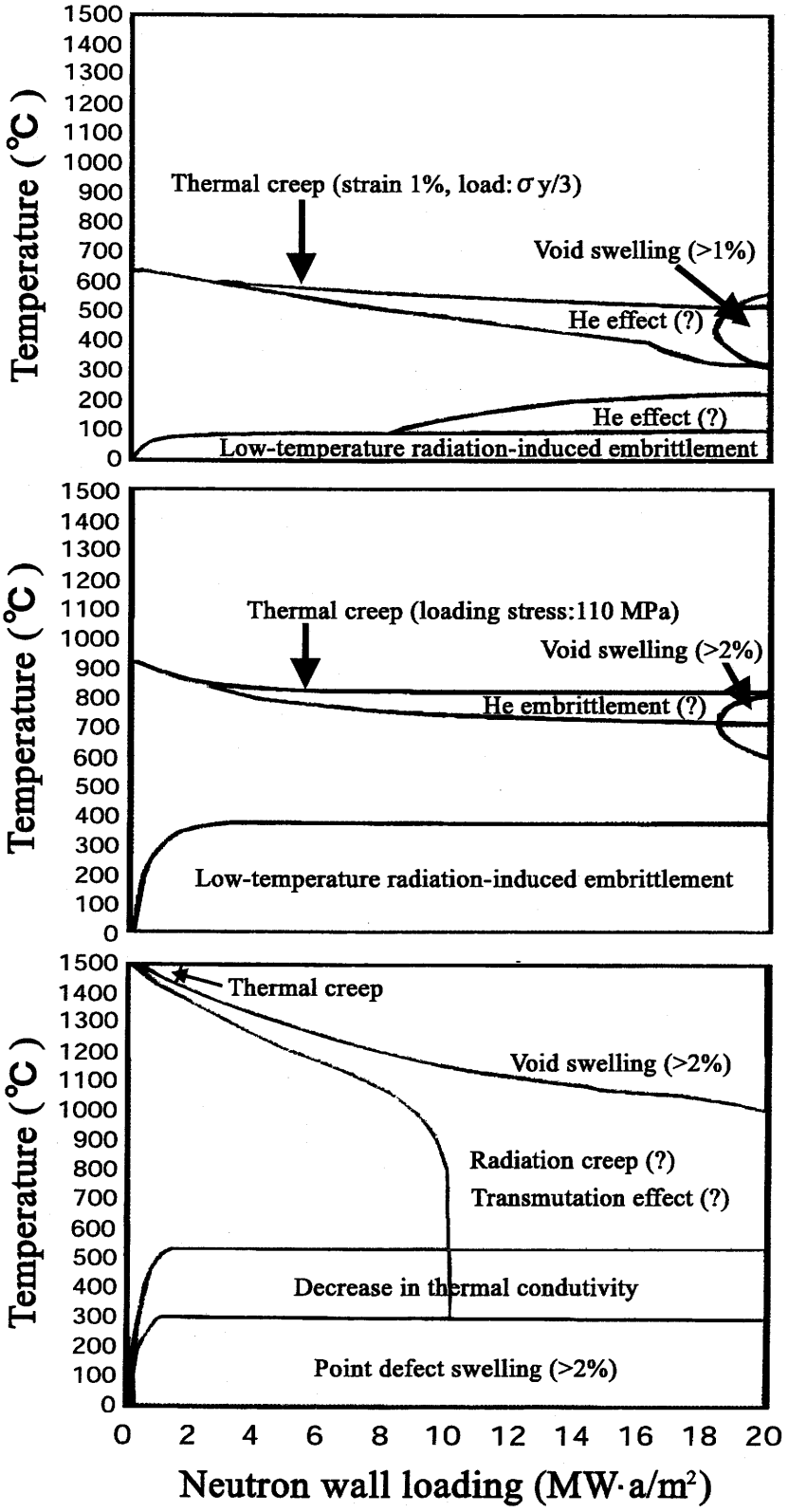

Fig. 1-4 Radiation properties and design windows of the three candidate materials [17].

Table 1-2 Major breeding blanket concepts for the candidate structural materials [11, 25-26]

Concepts	Coolant	Breeding material	Structural material	Neutron maltiplier	Operation conditions	
					Temperature (°C)	Pressure (MPa)
	He	LiPb	F/M steel	Be	250-550	5-20
	H_2O	Pb-Li	F/M steel	Pb-Li	250-550	12-15
	Li	Li	Vanadium	Li	350-750	~1
	He	LiPb	SiC/SiC	Be	450-950	5-20

(ii) Ferritic/martenstic steels

The ferritic/martenstic steels show the lowest in the performance temperature, as shown in Table 1-2. However, they have the most advanced technology base of the three candidate materials and a broad industrial experience in fabrication, process and welding as materials in fossil and nuclear energy plants.

Recently, from the viewpoint of low activation, F82H (Fe-8%Cr-2%W-VTaB) [27], JLF-1 (Fe-9%Cr-2%W-VTaN) [28], and OPTIFER [29], using tungsten as a replacement for Mo, and V and Ta as the carbide formation elements, were developed in Japan and Europe. They show reasonably good thermophysical and mechanical properties, good compatibility with the coolants and breeding materials and a low swelling and a low sensitivity to helium embrittlement. Research for establishing the design database of these alloys is being carried out under domestic and international collaboration programs.

One of the key issues of these alloys is the radiation induced hardening and embrittlement at the low temperature, i.e. radiation induced increase in yield stress and increase in DBTT [18-20]. Enhancing the fracture toughness in unirradiated and irradiated conditions is crucial for extending the design window to lower temperature. The upper operating temperature for ferritic/martenstic steels would be limited to ~550°C, according to high temperature strength properties. At temperature higher than 650 °C their thermal creep strength decreases sharply [11]. The irradiation will enhance the creep deformation at low temperature. Other important issues are the effects of helium and hydrogen transmutations, the effect of ferromagnetism on plasma stability, and welding technology development (Their welded joints have to be post-welded heat treated).

To increase the attractiveness of the ferritic/martensitic steels as a structural material, the development of the ODS ferritic steels will be an option. ODS ferritic steels exhibit high creep rupture properties [30-32], and are thus potential to increase the upper operating temperature to about 750 °C. However, the ODS ferritic steels have some feasibility issues such as homogeneity of microstructure, isotropy of properties, joint and fabrication technology.

(iii) Vanadium alloys

Vanadium-base alloys have been identified as an attractive promising structural material for the first-wall and blanket of fusion power plants, due to their outstanding high-temperature strength, low neutron activation and rapid activation decay, and their compatibility with lithium, which is the self-cooled tritium breeding material [33-36]. Vanadium alloys based on V-Cr-Ti constituents have a favorable combination of thermophysical properties and high creep strength [34].

Pickup of the interstitial elements such as oxygen, carbon, nitrogen and hydrogen in vanadium alloys can seriously degrade the mechanical properties and the radiation properties. Although the importance of interstitial impurities on the behavior of vanadium alloys has long been recognized, many aspects of the behavior are remaining as key research issues. Interstitial elements can be introduced into the alloys during fabrication, working process, and welding and joining. Therefore, welding and joining technologies should be developed as well as the fabrication processes controlling the impurity pickups.

The most attractive blanket for vanadium alloys is a self-cooled liquid lithium concept due to the chemical compatibility of vanadium and lithium [35-36], resulting in the excellent heat transfer characteristics of a liquid metal coolant, the reasonable high temperature operation, and thus high thermal efficiency. A self-cooled liquid lithium/vanadium concept has high tritium breeding property, and a simple structure blanket with low substitution frequency can be designed.

A liquid metal cooled concept requires electrical insulation on the surface of the coolant channels, in which the flow direction is perpendicular to the magnetic field, for the purpose of reducing pressure drops associated with magnetohydrodynamic (MHD)

forces [37-38]. Thus development of insular coatings is one of the key issues for the liquid lithium coolant/ breeding blanket concepts.

(iv) SiC/SiC

SiC/SiC composites have potentially a number of advantages in term of low radioactivity, low decay heat at short and intermediate cooling times, and high operating temperature resulting in the high thermodynamic efficiency because of their high temperature strength, strength to weight ratio and high corrosion resistance. However, their development for a structural material shows the most difficult challenge in three advanced structural materials [39-40]. To apply these materials to a fusion reactor, critical issues are remaining such as fabrication, cost, joining and hermeticity. The reduction of thermal conductivity by irradiation poses a serious limitation to the surface heat load capability of SiC/SiC composites. The effects of very high hydrogen and helium formation on swelling and the mechanical properties are also of concern.

1-4. Status of the research for vanadium alloys

1-4-1. Manufacture of the large heats

(i) Optimization of alloying elements

Vanadium base alloys were investigated and developed as fuel cladding for fast breeder reactors in the 1960s and 1970s. Recently, vanadium-base alloys are expected as an attractive promising structural material for the first-wall and blanket of fusion power plants, as mentioned in the previous sections.

Yield strengths of V-Cr-Ti alloy are shown in Fig. 1-5 [41] as a function of (Cr+Ti) contents. In all the specimens Ti and the combined impurity (C+N+O) contents were 4-5 wt% and 360-770 mass ppm, respectively. For all test temperatures, the yield and ultimate tensile strengths increased linearly with the increase in combined contents of Cr and Ti, indicating the predominant role of Cr and Ti on tensile strength. On the other hand, the DBTT for V-Cr-Ti alloys decreased drastically with the combined contents of Cr and Ti exceeding10 wt% [33-34].

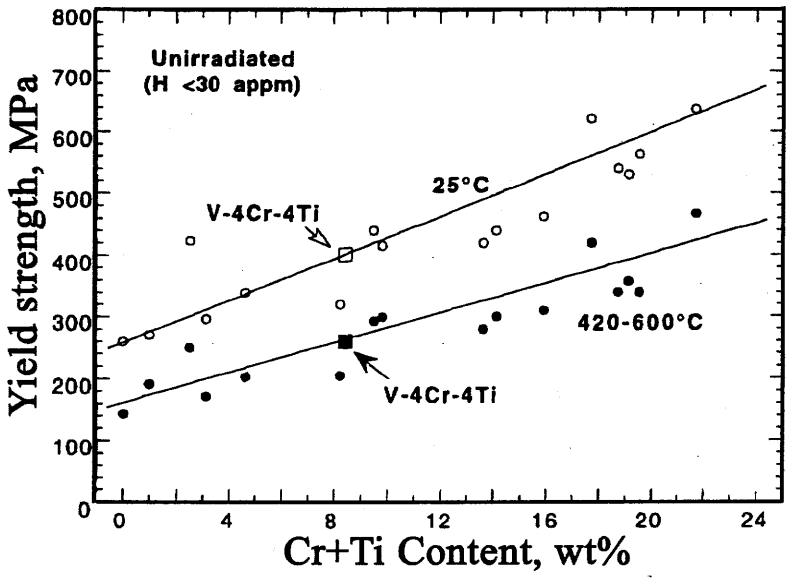

Fig. 1-5 Effect of (Cr + Ti) content on the yield strength of vanadium based alloys [41].

Fig. 1-6 shows the dependence of DBTT in vanadium alloys on the combined (Cr + Ti) contents [33]. The DBTT for unirradiated, irradiated and hydrogenated V-Cr-Ti alloys containing combined (Cr + Ti) contents of 4.6 to 8.4 wt% is lower. After irradiation at various conditions, the ductility loss and swelling of V-4Cr-4Ti alloy was still low [42]. Based on these results a V-4Cr-4Ti alloy was determined as a reference composition [43].

Recently, oxidation and corrosion resistance were recognized as important issues for the practical use. Development of the alloys enhancing these properties has been investigated, with maintaining the excellent properties of V-4Cr-4Ti alloys. It was reported that oxidation and corrosion resistance for vanadium alloys were improved significantly by adding a small amount of Si, Al and Y [44-48]. Research on the mechanical and radiation properties for these alloys is carried out extensively [44-47].

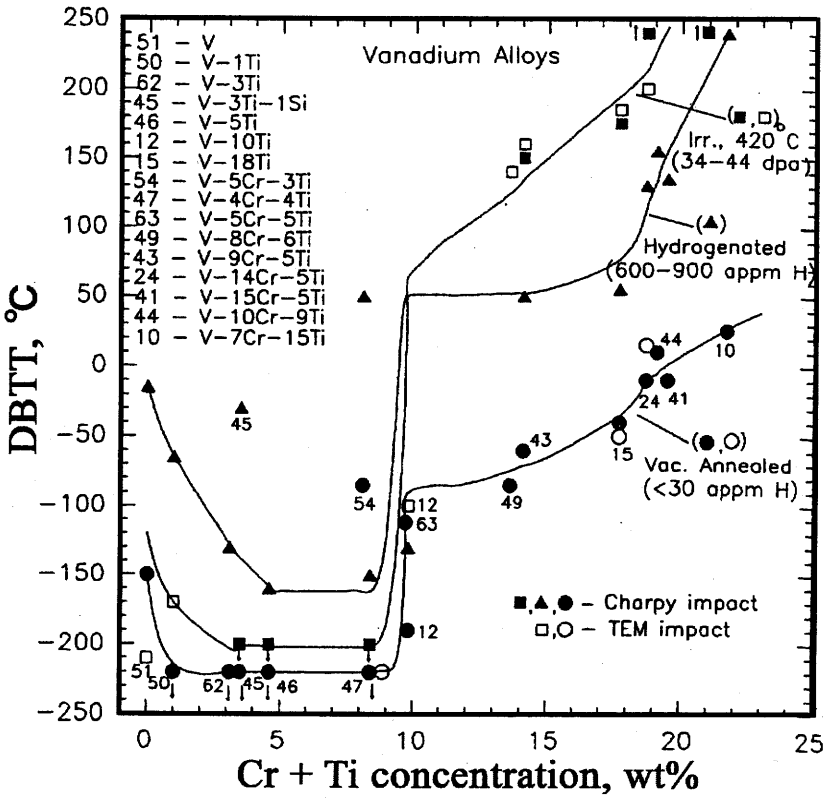

Fig. 1-6 Dependence of DBTT for vanadium alloys on (Cr + Ti) content [33].

(ii) Impurity effects

Some large heats have been fabricated in the US [49-50], Japan (NIFS-HEATs) [51-53] and Russia [54]. In the cases of the NIFS-HEATs, the properties are expected to be improved due to the lower interstitial impurities levels. In vanadium alloys, their process into various product forms is relatively easy such as rolling and tubing [50, 53]. However, properties of vanadium alloys are degraded by the pickup of interstitial impurities, such as H, C, N and O. Fig. 1-7 shows the effect of nitrogen and oxygen contents on hardness of vanadium. Hardness increased linearly in the same slope with the increase in oxygen and nitrogen contents: for the as-melted and as-rolled conditions. The hardening coefficient of nitrogen is, however, almost twice larger than that of oxygen [55].

Fig. 1-8 shows the effect of the hydrogen level on the impact absorption energy in vanadium based alloys [33]. The DBTTs for the vanadium based alloys were increased with increasing the hydrogen levels.

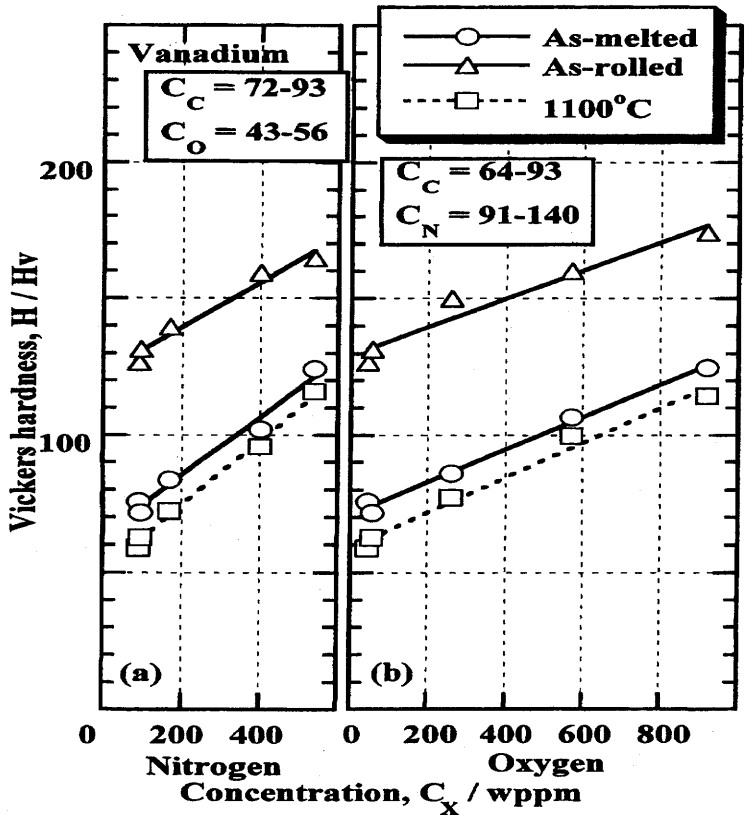

Fig. 1-7 Effect of: (a) nitrogen and (b) oxygen on the hardness of unalloyed vanadium [55].

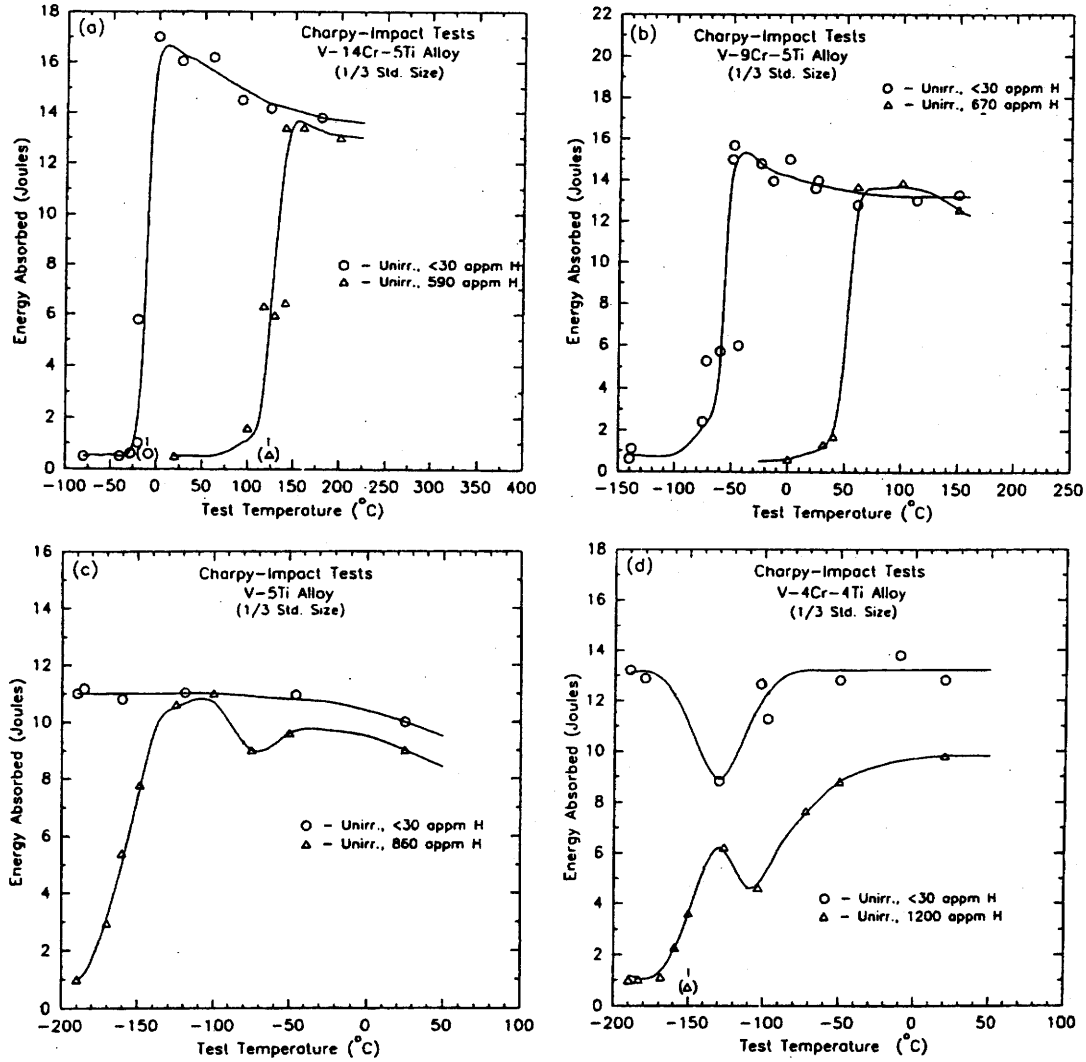

Fig. 1-8 Effect of the hydrogen level on the impact absorption energy [33].

These interstitial impurities also resulted in the decrease in the mechanical properties of the weld metal [24, 56]. Fig. 1-9 indicates the change of the absorption energy with the test temperatures for the weld metal with different impurity levels [56]. Fig. 1-9 presents that the decrease in the impurity levels of the weld metal improved the impact properties drastically.

Change of the dose rates as a function of cooling time after the use in a fusion reactor is given for some vanadium alloys in Fig. 1-10 [57], where Simple V4Cr4Ti means the theoretically pure V-4Cr-4Ti alloy without any impurities. The impurity compositions for the three alloys, NIFS-HEAT-1, 2 and US 832665, is shown in Table

1-3. Assuming that we can handle them at the contact dose level of 10 μSv/h, we can recycle the pure ternary alloy by hands-on after 100 year cooling. According to the figure a hands-on recycling of the other alloys with impurities seems to be difficult. However, with the decrease in some critical impurities, especially Nb in the case of the three alloys [57], the cost for recycling is expected to be reduced significantly.

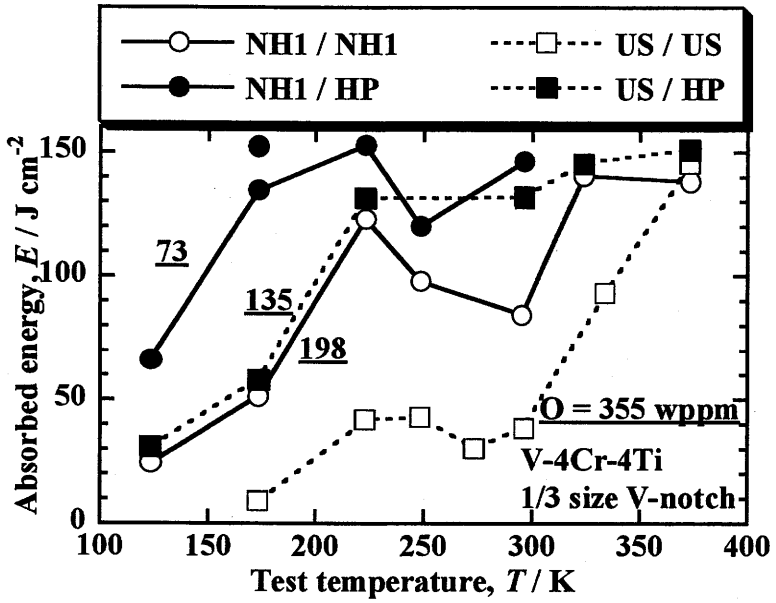

Fig. 1-9 Improvement of an absorption energy of the weld metal by high purity alloy [56].

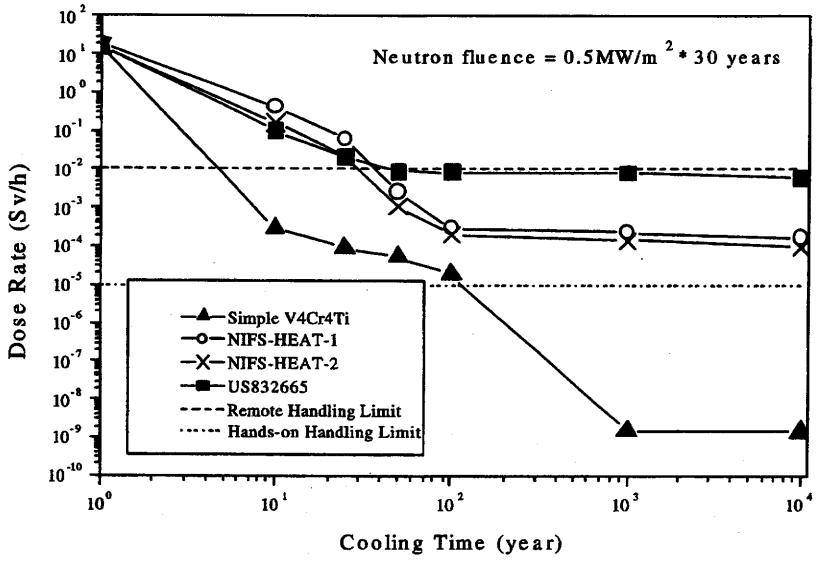

Fig. 1-10 Dose rate as a function of cooling time for the vanadium alloys [57].

Table 1-3 Impurity levels of three V- alloys and the required control level for recycling [57].

Impurity	NIFS-HEAT-1	NIFS-HEAT-2	US 832665
Co	2	0.7	0.295
Nb	1.4	0.8	60
Ag	<0.05	<0.05	0.0775
Mo	23	24	315
Al	119	59	355
Ni	13	7	9.6
Mn	<1	<1	0.21
Fe	80	49	205
Cu	4	2	0.84
Si	280	270	785
Na	17	<1	0.012
Ta	58	13	19
Sn	<1	<1	0.24
Sb	<1	<1	0.17
W	<1	<1	25
As	1	<1	1.4
N	103	122	100
C	56	69	170
O	181	148	330
Zr	<10	2.5	46
P	16	7	33
S	9	3	16.5
Ca	3	12	0.26
Mg	<1	<1	0.17
B	7	5	3.7

Thus, the reduction of critical impurities will enhance the irradiation resistance and the recycling and waste management capability of the vanadium alloys. Therefore, one of the key issues for fabrication of vanadium alloys is to eliminate the pickup of the critical impurities from the atmosphere during the fabrication and working process.

(iii) Effects of the heat treatment temperature

Fig. 1-11 shows the recovery of hardness for vanadium based alloys annealed at 180 to 1200 °C for one hour after cold working to 85% [58]. Three hardness peaks were observed in the hardness curves for all the specimens. The peak of hardness at 180-250 °C would seem to be due to the impurities [59]. It was reported that the hardness peak at 420-800 °C may be attributed to the formation of precipitates such as Ti (C, N, O),

V_6O_{13}, VS_4 and V_4C_3 [60], and the hardness peak at 1050 to 1200 °C was related to the formation of additional precipitates, Ti_5Si_3, redistribution of impurities, and thermal evaporation of alloy contents. The hardening above 1000 °C was reported by other papers as well [61-62].

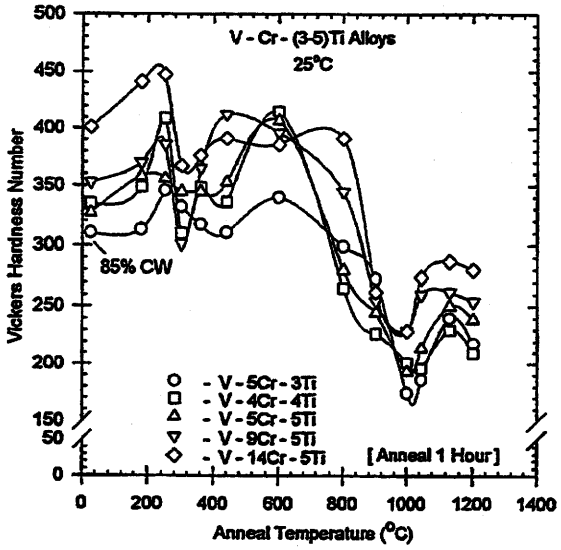

Fig. 1-11 Recovery of hardness for vanadium based alloys after cold working [58].

Table 1-4 presents the effect of heat treatment history on the properties [63]. Change of the grain size by the HT 2 was negligible, but the HT 2 produced significantly higher density of the precipitates, containing higher Ti, than HT 1. On the other hand, auger electron microscopy analysis showed significant sulfur enrichment (6 at%) on grain boundaries in the specimen for HT 1, but additional annealing at 890 °C resulted in the decrease in the sulfur concentration to 0.9 at%. The fracture toughness and the DBTT by HT 2 were enhanced more than that by HT 1, as shown in Table 1-4.

Table 1-4 Effect of heat treatment history on the properties [63]

Heat Treatment	Grain size (μm)	Fracture toughness (J_{IQ}, kJ/m^2)				DBT T (°C)	Precipitate density
		-50 °C	RT		100 °C		
HT 1	45	NM	52	IG & Cl	485	>RT	Few
HT 2	45	45	1100	Dimple	NM	-100	Many

HT 1: Annealing at 1125 °C for one hour and then furnace cooling
HT 2: HT 1 + Annealing at 890 °C for 24 hours and furnace cooling
NM: Not measured
IG & Cl: intergranular and cleavage

Fractography revealed that the specimen for HT 1 fractured with a mixture of intergranular and cleavage modes, which means that the grain boundary strength became low. These results indicates that enhancement of the properties could be expected by the heat treatment temperature due to reduced sulfur concentration on grain boundaries and the formation of impurity-induced precipitates such as Ti (C, N, O).

Fig. 1-12 is the results of a recent study on the DBTT [36]. In the case for V-(4-5)% Cr-(4-5)% Ti alloys annealed at 950 to 1000 °C, the DBTTs were lower, and increased with increasing the annealing temperature above 1000 °C, which agreed with the previous studies [34, 64-69]. The DBTT increased approximately linearly with increasing combined (Cr + Ti) contents above 10%, which is slightly different from the stepwise increase shown in Fig. 1-6, and increased with increasing the annealing temperature.

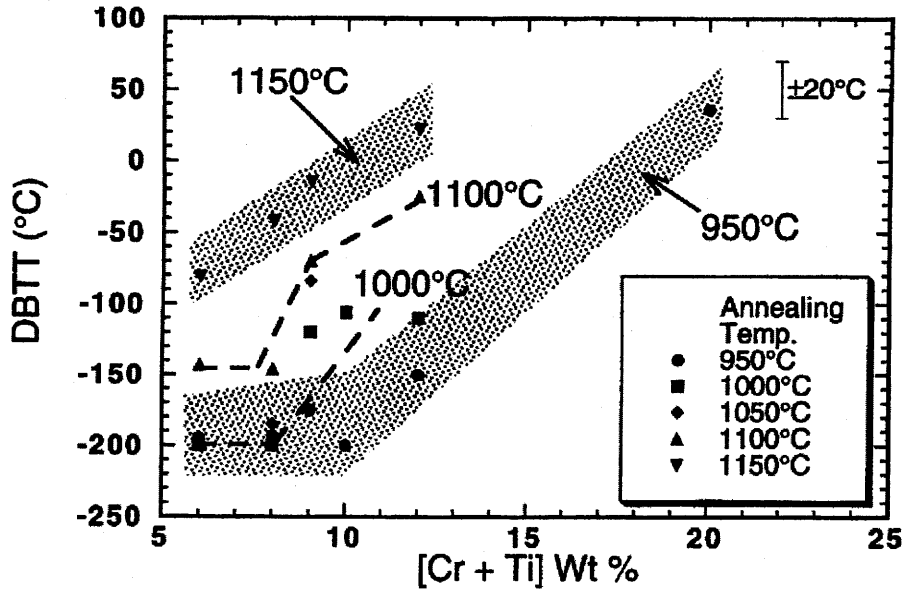

Fig. 1-12 Effect of annealing temperature and solute additions on the DBTT [36].

Fig. 1-13 demonstrates the effect of the post-welded heat treatment (PWHT) for the gas-tungsten-arc (GTA) welded vanadium alloy [24]. The DBTT in the as-welded conditions was above 200 °C. On the contrary, the PWHT at 950 °C for 2 hours reduced the DBTT by about 200 °C. Decrease in the DBTT was caused by the formation of the precipitates identified as $Ti_7(O_4N_2C)$after the PWHT. These results indicates that the

PWHT for precipitation will not be necessary, if the impurity levels of the materials are low before the welding and contamination with the impurities is negligible during the welding process.

These results indicate that even if the initial impurity content is rather high, the enhanced properties could be acquired by optimal heat treatment resulting in the formation of the precipitates with the impurities. Thus, to determine the optimal heat treatment for vanadium alloys, impurity behaviors with heat treatment history have to be investigated and clarified.

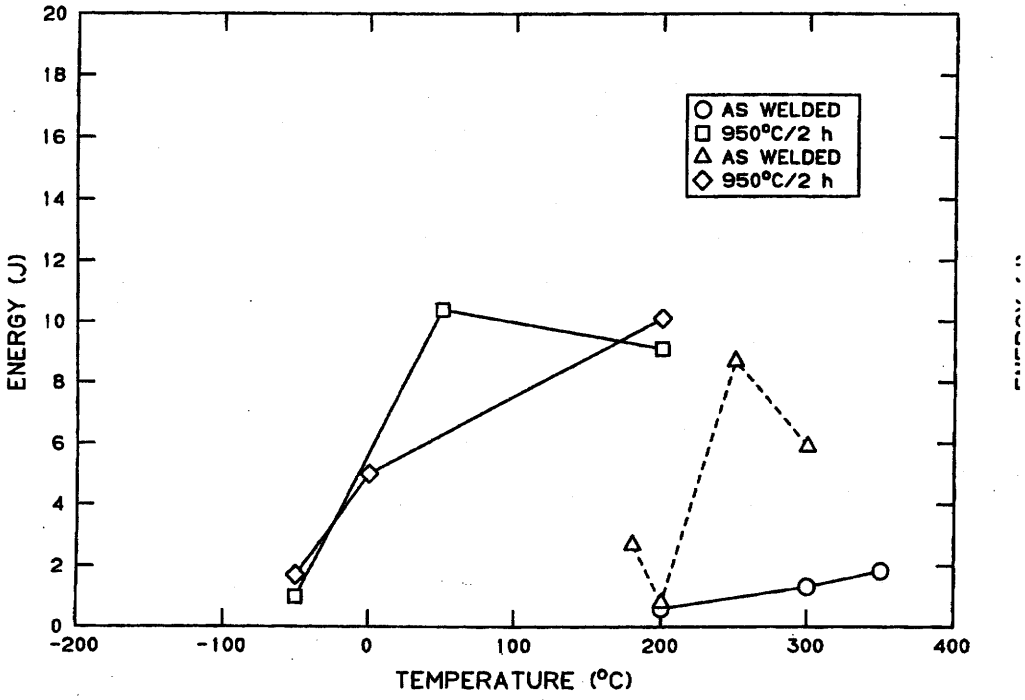

Fig. 1-13 Effect of the PWHT on the absorption energy for GTA welds [24].

1-4-2. Welding/Joint technology

(i) Key issues of welding/joint for vanadium alloys

In constructing large structures, welding/joint is one of the must technologies for structural materials after large scale heat production. The components for first wall/blanket of a fusion reactor are extremely large and require development of

manufacturing and welding/joint technologies. Although vanadium alloys have many advantages as a candidate structural material for fusion reactors, as mentioned in section 1.3, fusion reactors can not be successfully constructed unless the alloys can be welded without the degradations of their properties.

Recently, various welding/joint methods are under investigation, including GTA welding [24, 57], laser welding [23, 66-69] and electron beam welding (EB) [23, 69]. Welding/bonding vanadium alloys to other metals such as Inconel 625 [70] and SS 304 [71] are also preformed according to their purposes, using resistance welding, friction welding, explosive bonding and brazing. Development of welding/joint techniques for vanadium alloys is mainly focused on preventing contamination with the interstitial impurities.

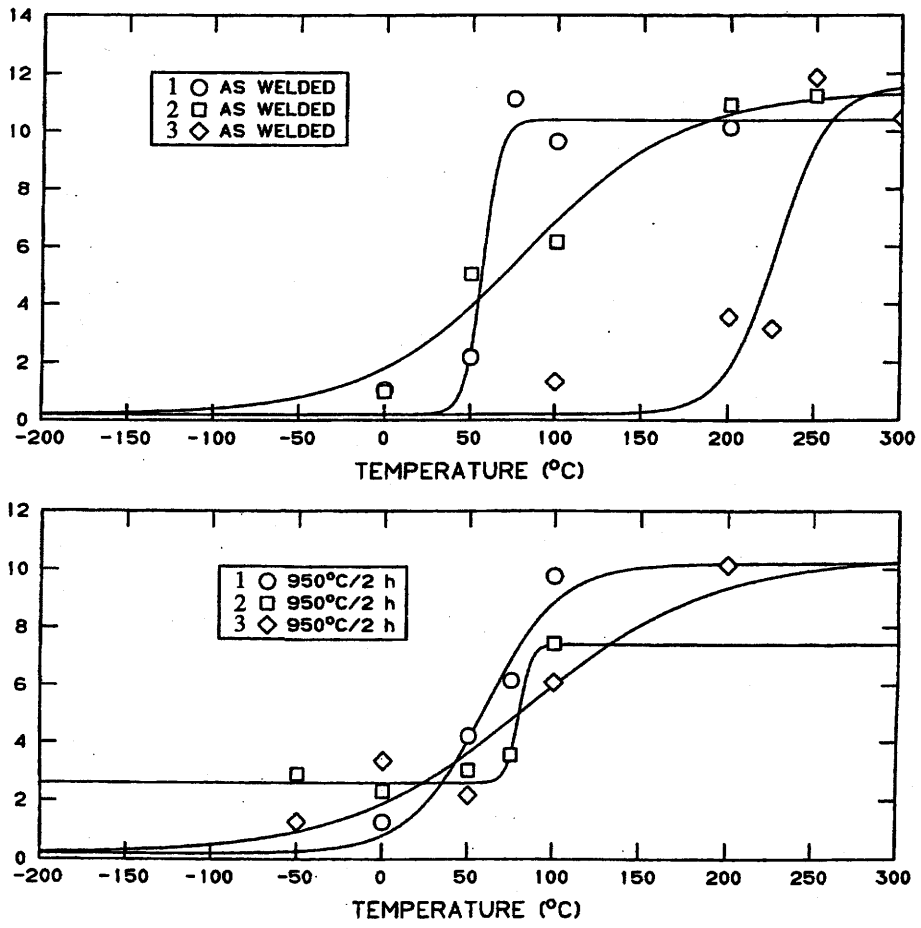

Fig. 1-14 Effect of the welding atmospheres on the impact absorption energy [24].

Table 1-5 Dependence of the welding atmosphere on impurity concentration

(mass ppm) [24]

	Welding atmosphere		Impurity concentration of fusion zone			DBTT
	Oxygen	Moisture	Oxygen	Nitrogen	Hydrogen	(°C)
1	4	23	374	104		57
2	14	84	352	110	21	82
3	27	260	412	146	15	228

Fig. 1-14 shows the effect of the welding atmospheres on the impact absorption energy of the GTA welded V-4Cr-4Ti alloy [24]. The welding atmospheres and impurity levels after GTA welding are listed in Table 1-5. Impurity concentration in the fusion zone varied with the welding atmosphere. The DBTT increased with the increase in the impurity level. In the two cases with relatively lower impurities, there was little change in the DBTT before and after the PWHT at 950 °C for two hours. On the contrary, PWHT at 950 °C for two hours resulted in the drastic shift of the DBTT from 228 to 86 °C in the case with higher impurities.

Table 1-6 Dependence of welding atmosphere on impurity concentration (mass ppm) [72]

	Base metal			Filler metal			Atmos.		Impurity level			DBTT (°C)
	O	N	H	O	N	H	O	H_2O	O	N	H	
JPN-JPN	180	88		180	110	3.7	0.75	6	198	108		-89
JPN-JPNHP	180	88		36	89	4.8	0.75	6	73	97	49	-145
US-US	310	73	4.3	370	110		0.75	6			69	6
US-JPNHP	310	73	4.3	36	89	4.8	0.75	6	135		59	-83

Table 1-6 indicates the DBTT and the impurity composition before and after improved GTA welding, using high-purity filler metal [72]. US, JPN and JPNHP indicate US 832665, NIFS-HEAT-1 and high-purity filler metal, respectively. The welding was carried out in a high-purity argon glove box to control the welding atmosphere. Although welded at the same atmosphere condition, the DBTT for the low oxygen base metal was lower. Moreover, the DBTT was decreased significantly, using

the high-purity filler metal, JPNHP, regardless of the impurity levels of the base metals.

Another critical issue is to suppress the grain growth and width of the weld zone, which includes the weld metal and the heat-affected zone (HAZ). The effect of grain size on the DBTT has been demonstrated by electron beam welded vanadium alloy. The weld metal with a factor of two larger grain sizes was produced by defocusing the electron beam; this resulted in an increase in the DBTT by about 150 °C [73]. It is also reported that the grain size had a significant effect on the ductility of vanadium alloys [74]. The grain size of a V-5Cr-5Ti alloy annealed at 1125 °C ranged ASTM 5 to 6. This specimen was seriously embrittled with relatively low levels of hydrogen and oxygen. On the other hand, the specimen annealed at 1050 °C (ASTM grain size 9) showed ductility above 19% (total elongation) at similar impurity levels. Although annealed at 1125 °C, the V-5Cr-5Ti alloy with a grain size of ASTM 9 showed only a small decrease in the ductility at the same impurity levels. The fractography for these specimens revealed that the coarser-grained specimens exhibited primarily intergranular fractures, while the finer-grained specimens showed mainly ductile cleavage. From these results, the embrittlement is shown to be strongly related to grain size of vanadium alloys.

Initial purity, welding atmosphere and grain size are significantly important parameters in the welding for vanadium alloys. For development the welding/joint technology for vanadium alloys, efforts should be made to prevent the impurity contaminations and to control the grain growth in the weld zone. In the case for GTA welding, nitrogen and yttrium addition is under consideration for fine grain size in the weld zone [72].

(ii) YAG laser welding

Laser welding has some similar, and some unique characteristics when compared to other welding processes. Like GTA welding, laser welding is a fusion process performed under inert cover gas. Like EB welding, laser welding is a high energy density beam process, where energy is targeted directly on the specimen. Laser differs from both GTA and EB in that it is achieved by the concentration of light waves. Thus, the laser welding can be applied to both electrically conductive and resistive materials. It does not require either a complete electrical circuit, or a vacuum chamber or shielding

for X-ray. In addition, laser welding can offer a cost advantage over EB welding in welding.

One of the largest advantages of the laser welding is the minimal amount of heat that is inputted during welding. The laser welding is capable of vaporizing metals with high melting point such as tungsten or non-metallic such as ceramics, because the energy density is so intense. The lasers can produce deep penetration welds by the keyhole technique. These benefits can result in the narrow welds, no distortion, minimal heat affected zones and excellent metallurgical quality. Especially, the YAG laser welding is a promising technique because of its flexibility for field, lenient requirement for atmospheric control, capability of deep penetration with less input, and remote operation capability. CNC automated weld machines with fiber optic beam delivery are also capable of handling small to large order quantities and precise positioning.

It should be noted that the blankets for fusion reactor are mainly composed of thin plates, their morphology is very complex and it is necessary to repair them by remote control. Thus, the YAG laser welding is a quite attractive technique for application to the fusion blanket.

Several research efforts for the laser welding on vanadium alloys have been carried out. It is necessary to control the environment during the welding for preventing the contamination with the impurities. In the previous study, the laser welding technology for vanadium alloys have been performed reducing the contamination by means of introducing argon gas [66-67]. Survey of the laser weldment with parameters such as power, traveling speed, pulse duration and frequency [66-67] and the properties of the weld metal and the base metal [68, 75] have been investigated for V-4Cr-4Ti alloy. The effect of the post welding heat treatment on the properties has also been investigated [23].

However, study on the effects of the welding condition for the high-grade welding technology is scarce. To optimize the welding parameters for vanadium alloys, estimation of various mechanical properties and mechanistic understanding on the impurity behavior are necessary. The heating history in the weld zone depends on the positions in the weldment. The change of the heat history will result in change of the impurity distribution. Thus, to characterize the properties of the weld metal and the HAZ, investigations for the microstructure and the impurity behaviors in the weld zone

are to be preceded.

1-5. Objectives of the present study

The purpose of this study is to establish a high-grade welding technology for V-4Cr-4Ti alloys. For this purpose, an environmental control box was fabricated to eliminate the contamination with the interstitial impurities, and then the YAG laser welding was carried out inside it.

The effect of the welding conditions on the mechanical properties of the weld zone, such as hardness, bending, tensile and charpy impact properties, and the impurity behavior in the weld zone by microstructural observation for the mechanistic understanding of the property change, based on the understanding of hardness and precipitation behavior by heat treatment were investigated.

As the basic study supporting the establishment of the welding technology, the understanding of the impurity behavior under the thermomechanical treatment processes is crucial. Thus, the effect of impurity levels on hardness and precipitation behavior by heat treatment was investigated. This study will be valuable for optimizing the fabrication and thermomechanical treatment conditions of the alloys, as well as for the welding development.

CHAPTER 2

Effect of impurities on the recrystallization and the precipitation behavior

2-1. Behavior of recrystallization and precipitation in vanadium alloys after cold rolling

In vanadium alloys, the precipitates induced by impurities and their distribution have a great effect on various properties. Thus, it is necessary to investigate the precipitation behavior to optimize the fabrication processes including thermomechanical treatments. The purpose of this study is to clarify the behavior of recrystallization and precipitation by annealing after cold working, for three kinds of V-4Cr-4Ti alloys, NIFS-HEAT-1, 2 and US 832665, with different levels of oxygen. The results will be discussed in relation to the redistribution of impurities.

2-1-1. Experimental procedures

Table 2-1 shows chemical composition of the V-Cr-Ti alloys used in this study. US 832665 is a 500 kg ingot fabricated by a US-DOE program [49-50]. The major difference in the composition of the three alloys is the level of oxygen. The thermomechanical treatment after melting for the NIFS-HEATs [51-53] was hot forging at 1423 K and hot or cold rolling. They were then cut into 10 mm after hot working. The US 832665 was a 3.8 mm thick plate, which was hot-extruded at 1423 K and warm-rolled at 673 K. All plates, NIFS-HEATs and US 832665, were cold-rolled to 90 % thickness reduction, into about 1 mm and 0.4 mm thick sheets, respectively.

After mechanical polishing and electro-polishing, the specimens were sandwitched with tantalum sheets and wrapped with zirconium getter foils, followed by annealing at the range of 473 to 1573 K for 1 hour in a vacuum ($<10^{-3}$ Pa). After annealing, micro-Vickers hardness tests were conducted at room temperature in the condition of load of 500 gf and loading time of 30 sec. Microstructural observations were also carried out using optical microscope, SEM (Scanning Electron Microscope) and TEM (Transmission Electron Microscope).

2-1-2. Effect of the heat treatment temperatures

(i) Recystallization behavior

Fig. 2-1 shows the hardness changes of each specimen as a function of the annealing

temperature. Fig. 2-1 shows no significant difference in the hardness curves for the three alloys, in spite of the difference in the oxygen content. The hardness of NIFS-HEAT-2 was lower than that of other two samples at most temperatures.

Table 2-1 Chemical composition of V-4Cr-4Ti alloys used (mass ppm for concentration).

	Cr*1	Ti*1	C	N	O
NIFS-HEAT-1	4.12	4.13	56	103	181
NIFS-HEAT-2	3.9	3.89	62	84	158
US 832665	3.8	3.9	80	85	310

*1: wt%

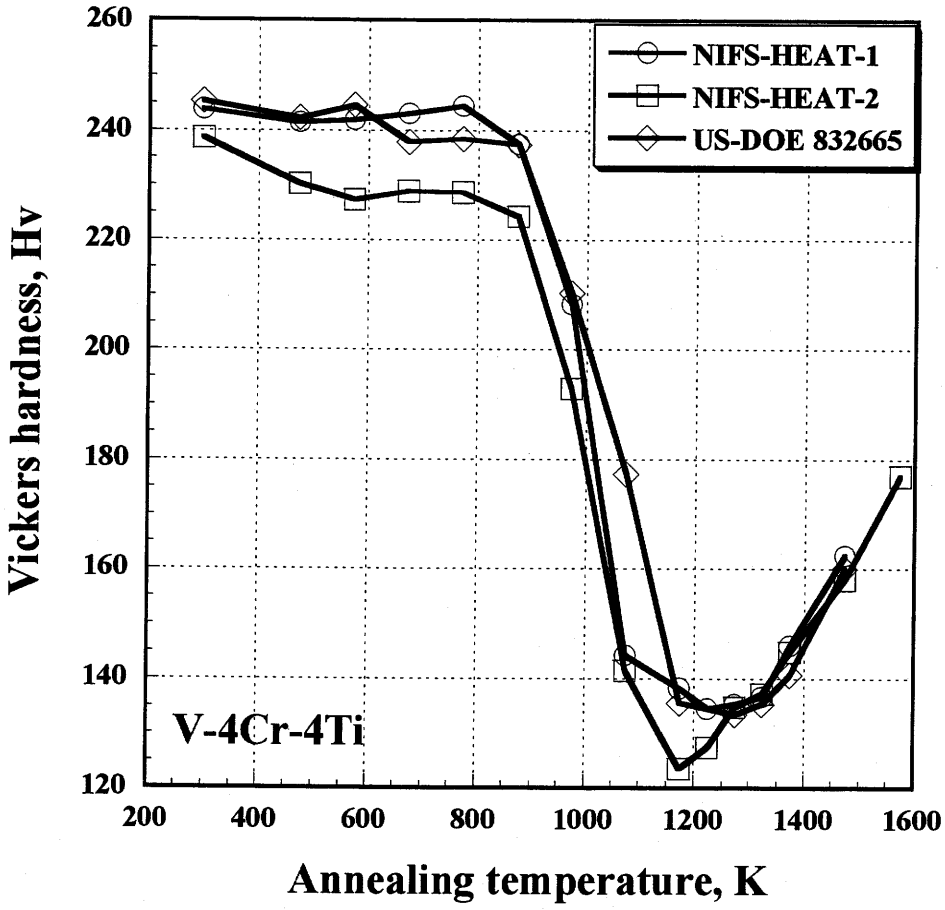

Fig. 2-1 Hardness change of the three alloys as a function of the annealing temperature. The annealing at each temperature was carried out for an hour.

Table 2-2 Size and aspect ratio of grains of the specimens annealed at various temperatures.

	Direction	1173 K		1273 K		1373 K		1473 K	
		Grain size	Aspect ratio	Grain size	Aspect ratio	Grain size	Aspect ratio	Grain size	Aspect ratio
NIFS-HEAT-1	Rolling	11.92	0.58	11.55	0.82	23.81	0.91	51.4	1
	Transverse	6.94		9.45		21.74		51.6	
NIFS-HEAT-2	Rolling	13.32	0.55	16.26	0.84	29.06	0.91	47.9	0.99
	Transverse	7.39		13.63		26.41		47.3	
US-DOE832665	Rolling	9.58	0.75	10.32	0.81	12.48	0.95	45	0.96
	Transverse	7.19		8.39		11.84		43	

(Grain size :μm)

Fig. 2-3 shows SEM image of NIFS-HEAT-1 annealed at 873 K for an hour. The microstructure observation revealed that recrystallization already started at 873 K. In this case, recrystallization took place partially with the size of recrystallized grains smaller than ten microns.

Fig. 2-4 shows the change of the grain size with annealing temperature. At 1173 K there was no great difference in grain size among the three alloys. However, in NIFS-HEATs grain size significantly increased with annealing temperature. On the other hand, the change in the grain size to annealing temperature is small for US-DOE 832665. Fig. 2-4 would imply that the rate of grain growth decreases with the increase of the impurity levels.

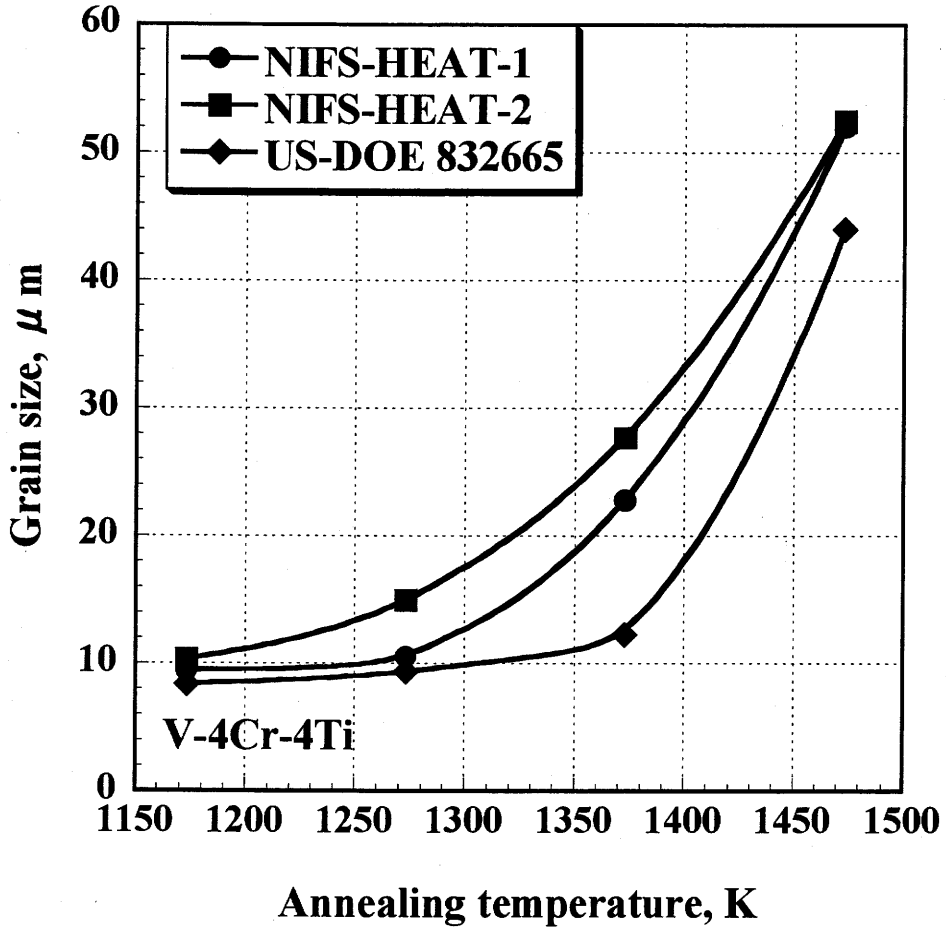

Fig. 2-4 Change of grain size from 1173 K to 1373 K in three alloys. The grain size increased with the decrease of the oxygen level.

(ii) Precipitation behavior

Fig. 2-5 indicates the precipitate distribution in the transverse plane of the three alloys annealed at 1273 K for an hour. In NIFS-HEATs, the precipitates were aligned along the rolling direction. On the other hand, the precipitates in US-DOE 832665 were uniformly aligned in the matrix.

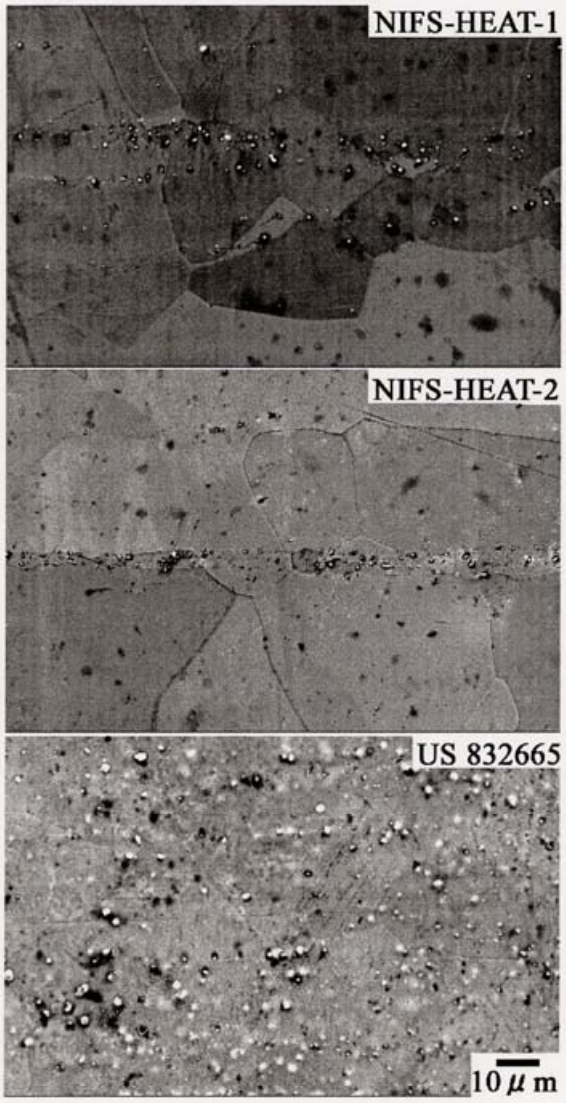

Fig. 2-5 Distribution of the precipitates in the transverse plane of the specimens annealed at 1273 K for 1 hour. The band structure of the precipitates was observed in NIFS-HEATs. On the other hand, the precipitates were distributed uniformly in US 832665.

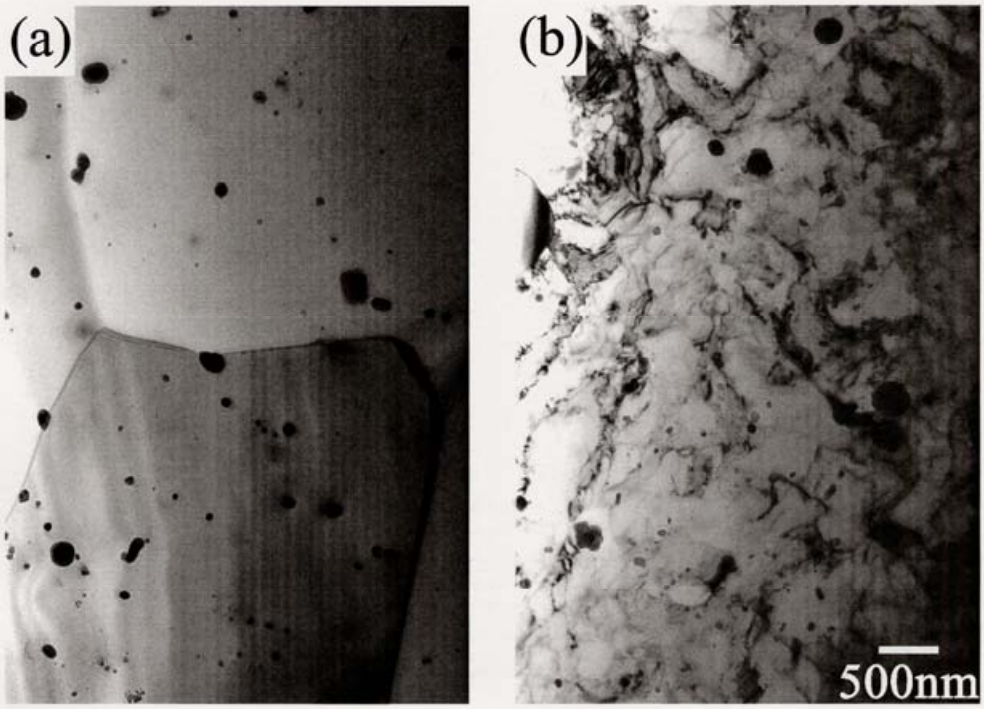

Fig. 6 Comparison of (a) NIFS-HEAT-1 and (b) US 832665 annealed at 1073 K for an hour after cold rolling. The recystallized grains without strains were observed in NIFS-HEAT-1. However, the strains still remained in US 832665. The large and small precipitates existed in both specimens.

Fig. 2-6 is the TEM images of NIFS-HEAT-1 and US 832665 annealed at 1073 K for an hour after cold rolling. In NIFS-HEAT-1, the recrystallized grains without strains were observed. On the other hand, the strains by cold rolling still remained in US 832665.

Fig. 2-7 is the TEM images of NIFS-HEAT-2 annealed at 1223 to 1473 K. In specimens annealed at 1223 and 1273 K, two kinds of precipitates (larger and smaller ones) were observed. Fig. 2-8 shows TEM-EDS analysis of matrix, large and small precipitates, respectively. Fig. 2-8 shows that the large and the small precipitates are Ti-rich and Ti-C-O complexes, respectively. As shown in Fig. 2-7, the small precipitates vanished by annealing at above 1373 K. Fig. 2-9 is the SEM images of NIFS-HEAT-2 annealed at 1273 to 1573 K. The large precipitates shown in Fig. 2-7 aligned along the rolling direction. These large precipitates have already been observed on the as-rolled

conditions. Large precipitates were observed in the specimens annealed up to 1473 K, but seem to be dissolved by annealing at 1473 K, as shown in Fig. 2-7 and 2-9. The large precipitates vanished after annealing at 1573 K, as shown in Fig. 2-9.

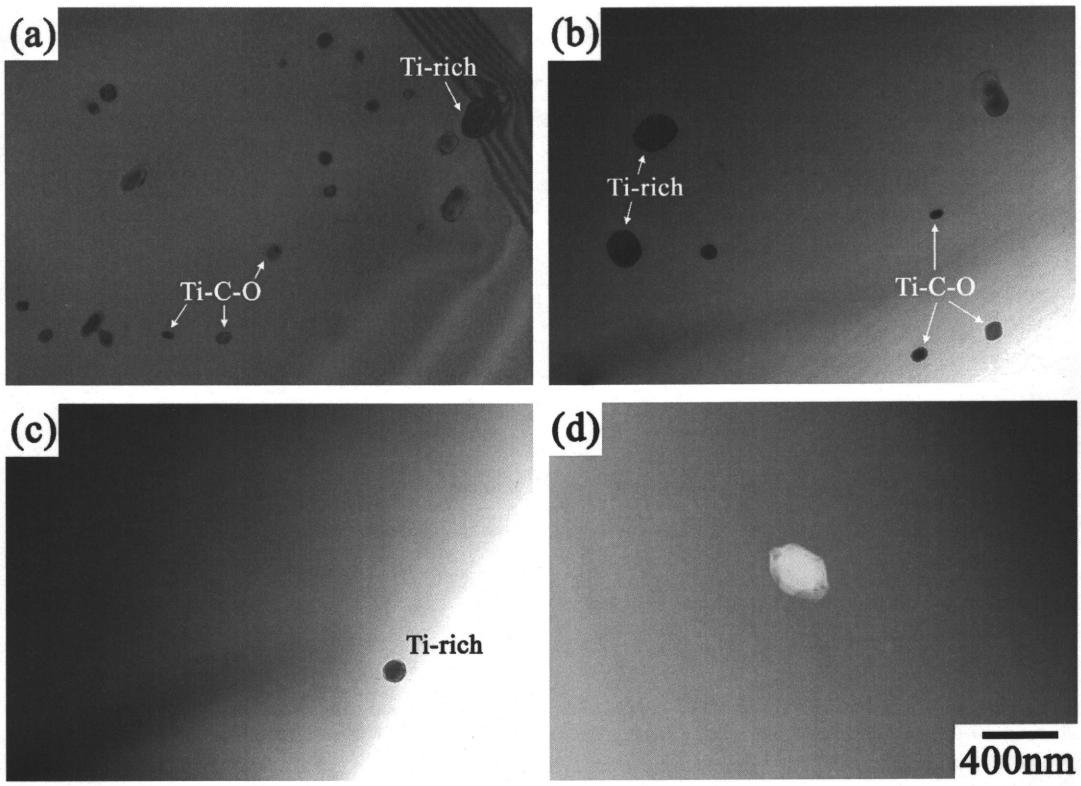

Fig. 2-7 TEM images of the NIFS- HEAT-2 specimens annealed at 1223 to 1473 K. Two kinds of precipitates were observed at 1223 and 1273 K. Only larger precipitates were observed at 1373 and 1473 K. (a) 1223 K (b) 1273 K (c) 1373 K (d) 1473 K

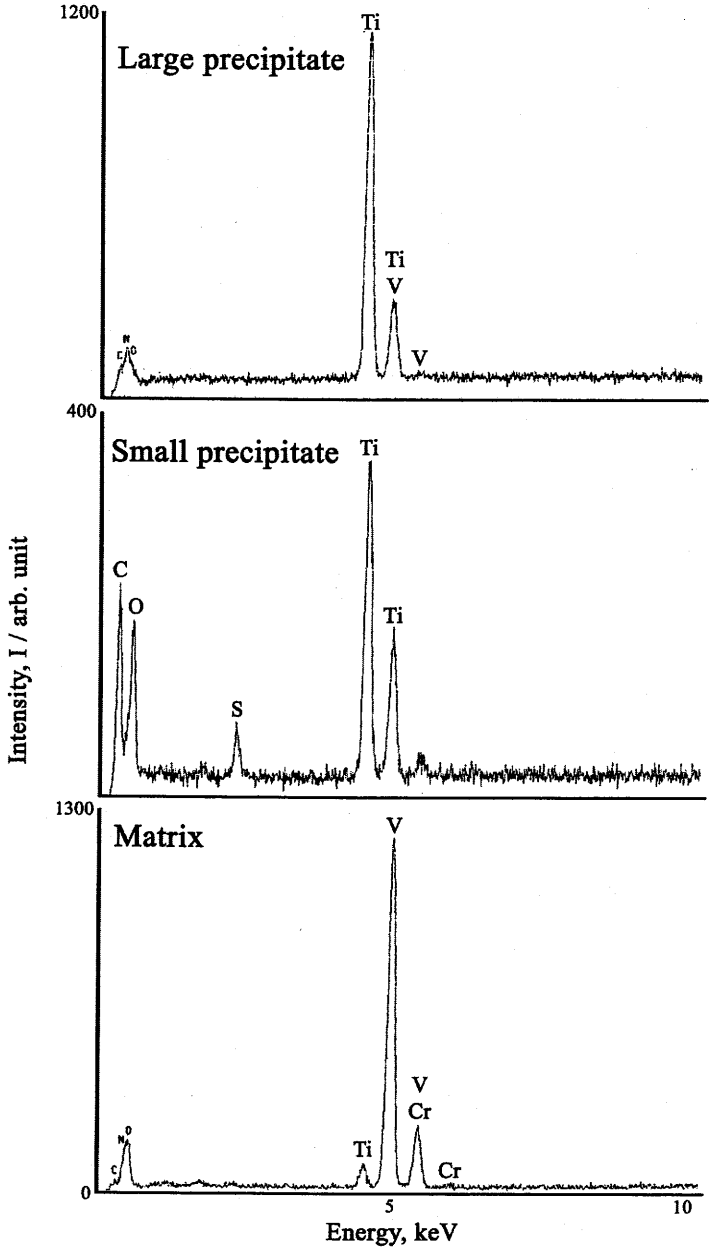

Fig. 2-8 TEM-EDS analysis on the precipitates and in the matrix. Analysis reveals that large precipitates were Ti-rich, and small were Ti-C-O. The peak of sulfur is thought to be originated from residual electrolyte (H2SO4) used for electro-polishing.

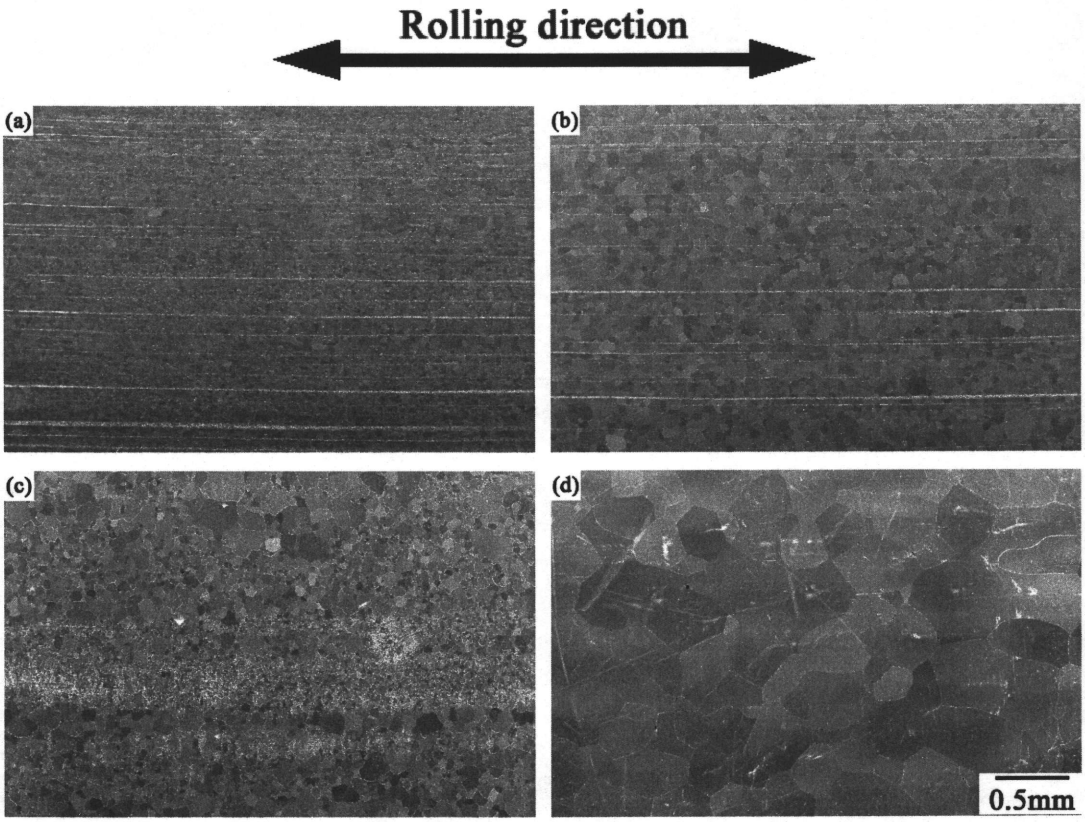

Fig. 2-9 SEM images of the NIFS- HEAT-2 specimens annealed at 1273 to 1573 K.
(a) 1273 K (b) 1373 K (c) 1473 K (d) 1573 K

Fig. 2-10 is the SEM images on the grain boundaries in NIFS-HEAT-2 annealed at 1273 to 1573 K. No precipitates were observed on the grain boundaries when annealed at 1273 K, but fine precipitates were formed on the grain boundaries at above 1373 K.

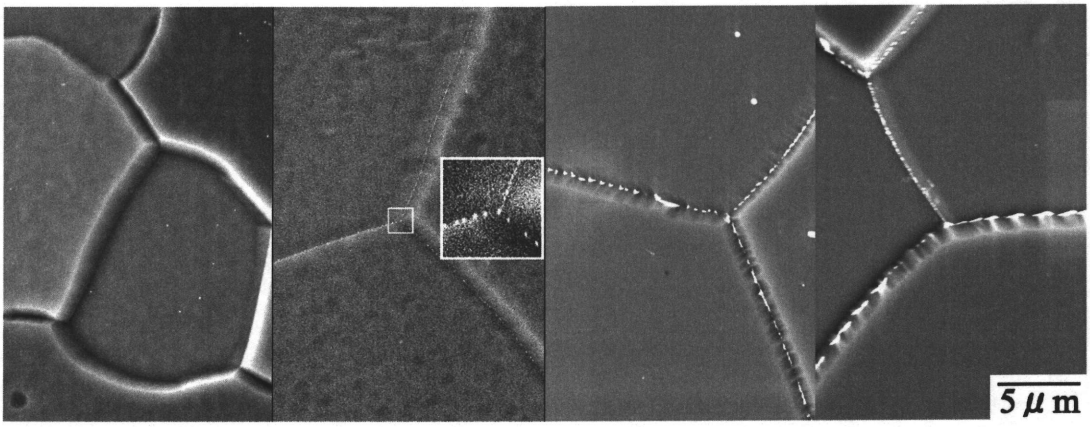

1273 K 1373 K 1473 K 1573 K

Fig. 2-10 SEM images on the grain boundaries in NIFS-HEAT-2.

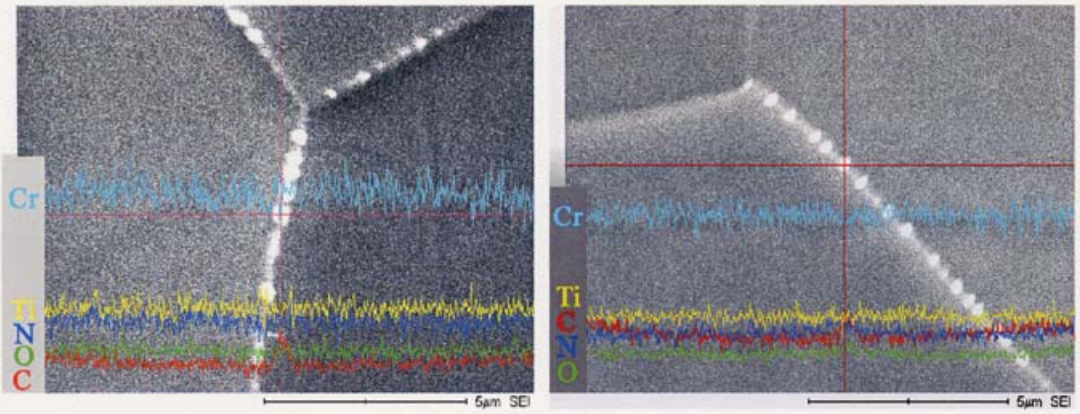

1373 K 1573 K

Fig. 2-11 Result of SEM-EDS analysis for precipitates on a grain boundary in NIFS-HEAT-2 annealed at 1373 and 1573 K for 1 hour.

Fig. 2-11 shows the result of compositional analysis with SEM-EDS (Energy Dispersive X-ray Spectroscopy) on a grain boundary including precipitates, for NIFS-HEAT-2 annealed at 1373 K and 1573 K. As shown in Fig. 2-11, it was confirmed that carbon content is higher at the precipitates. The concentration of chromium, titanium, oxygen and nitrogen was however almost homogeneous. In the case annealed at 1573 K, The enrichment of carbon, oxygen and nitrogen was observed, but the concentration of others was not recognized.

2-1-3. Discussions: Optimum heat treatment temperature for cold-rolled vanadium alloys

Two kinds of precipitates were observed in all specimens annealed at 973 to 1273 K. From the TEM-EDS analysis (Fig. 2-8), larger precipitates were identified to be Ti-rich and smaller were to be Ti-C-O compound. Only Ti-rich precipitates, however, were observed in the specimen annealed at 1473 K (Fig. 2-7), and vanished by annealing at1573 K (Fig. 2-9). SEM observation reveals that the distribution of Ti-rich precipitates were heterogeneous, as shown in Figs. 2-5 and 2-9.

It is likely that Ti-rich precipitates were already present after hot rolling, following the melting. In the previous study, annealing of as-melted NIFS-HEAT-2 at 1423 K for an hour resulted in the formation of the Ti-rich precipitates [76]. The band structure of the precipitates in NIFS-HEATs, as shown in Figs. 2-5 and 2-9, was considered to be formed, as a result of the elongation of the precipitate distribution parallel to the rolling direction induced by the rolling process.

It is reported that the precipitate bands were also observed in US832665 after hot extrusion [77]. In the present study, however, the precipitates were uniformly distributed. The collapse of the band structure of the precipitates in US-DOE 832665 is likely to be due to the high degrees of rolling (> 99% after hot extrusion) before annealing, relative to 90% for NIFS-HEATs. In the previous study, high thickness reduction by rolling (the degrees of cold rolling was about 99% after hot working) also resulted in the collapse of the band structure in NIFS-HEAT-2 [76].

The hardness recovery curve and initiation of recrystallization were not influenced significantly with the impurity level. From the result of the SEM observation, recrystallization already occurred at about 873 K, as shown in Fig. 2-2. At this temperature, hardness decrease also started in all specimens. In hardness curves shown in Fig. 2-1, NIFS-HEAT-1 became softened suddenly by annealing at 1073 K for 1 hour. Strain introduced by rolling did not remain in recrystallized grains in NIFS-HEAT-1 annealed at 1073 K, as shown in Fig. 2-6 (a). However, as shown in Fig. 2-6 (b), the strains introduced by rolling still remained in US 832665 annealed at 1073 K. The drastic decrease in hardness of NIFS-HEAT-1 annealed at 1073 K may be caused by the formation of recrystallized grains without strains.

The grain size was in order of NIFS-HEAT-2, NIFS-HEAT-1 and US-DOE 832665. The recrystallized grain size increased with decreasing impurity levels, as shown in Fig. 2-4. The grain size in the band structure of the precipitates was much smaller, as shown in Fig. 2-2. The grain size during the recrystallization process may be suppressed by the precipitates, because the secondary precipitates suppress the migration of the grain boundary. Ti-rich precipitates are likely to be enhanced with the increase of the impurity levels. Therefore, the smaller grain size of US-DOE 832665 may be due to the Ti-rich precipitates suppressing the grain coarsening.

Another characteristic of the precipitation behavior by annealing at above 1373 K is the formation of precipitates in grain boundaries (Fig. 2-10). As shown in Fig. 2-11, enrichment at the precipitates was observed for carbon, but not for chromium, titanium, oxygen or nitrogen. Therefore the precipitates formed at 1373 K on grain boundary were expected to be V-C precipitates. On the contrary, SEM-EDS reveals that the precipitates formed at 1573 K seem to be V (CNO) precipitates, as shown in Fig. 2-11.

Additional hardening in hardness curves was found by annealing above the temperature, in which hardness reached the minimum, as shown in Fig. 2-1. SEM and TEM analysis revealed that Ti-C-O and Ti-rich precipitates, observed at 1273 K, vanished by annealing at 1373 K and 1573 K, respectively. Instead, V-C or V (CNO) precipitates were formed on the grain boundaries. These results suggest that redistribution of impurities took place at above 1373 K. It is thought that increase in the hardness above 1273 K is due to the increase in solid solution impurities caused by the re-solution of the Ti-C-O or/and Ti-rich precipitates.

It is reported that the DBTT of a V-Cr-Ti alloys increases when the annealing temperature exceeds 1273 K [65]. It is expected that the increase of the DBTT is due to the increase in the solid solution impurities and the precipitates formed on grain boundaries. The present study strongly suggests that the annealing temperature for V-4Cr-4Ti should be 1273 K or below to obtain good mechanical properties.

2-1-4. Summary

The behavior of hardness recovery, recrystallization and precipitation was investigated, using three kinds of V-4Cr-4Ti alloys with different oxygen contents.

(1) Irrespective of the oxygen content, behavior of hardness curve and precipitation was similar with each other. Hardness decrease and recrystallization started around 873 K. In all specimens, annealing above 1273 K resulted in increase in hardness.

(2) The rate of grain growth decreased with the increase in the impurity level. The recrystallized grain size from 1173 K to 1473 K was significantly influenced by the distribution of the precipitates.

(3) Two kinds of precipitates were observed in all specimens at 973 to 1273 K. From the TEM analysis, larger precipitates were identified to be Ti-rich and smaller were Ti-C-O compounds. The Ti-C-O and Ti-rich precipitates disappeared by annealing at 1373 and 1573 K, respectively. V-C or V (CNO) precipitates were formed on grain boundaries, as a result. It is thought that increase of hardness above 1273 K is due to the re-solution of the Ti-C-O or/and Ti-rich precipitates, and resulting increase in the solid solution level of impurities. This is consistent with the reported DBTT shift by increasing the annealing temperature. Based on the results, the final annealing temperature for V-4Cr-4Ti is recommended to be 1273 K or below for the purpose of obtaining good mechanical properties.

(4) The band structure of the Ti-rich precipitates was observed in NIFS-HEATs, but not in US 832665. The absence of the band structure in the US 832665 seems to be due to its high total rolling degree after the melting. The band structure influences the recrystallization behavior. It is necessary to investigate the effect of the band structure on other properties of the alloys.

2-2. Effect of the impurity level on the precipitation behavior

As mentioned in the 2-1 section, annealing above 1573 K resulted in additional hardening, caused by the dissolution of the precipitates, Ti-C-O or/and Ti-rich compounds. In the previous researches, the effect of the impurity level and the precipitates on hardness and mechanical properties in vanadium and its alloys was reported [55, 60-63]. However, there were scarce reports on the effects of each impurity separately, such as oxygen and nitrogen, on hardness and the precipitation.

For systematic understanding of the impurity effects, investigation of model alloys with a wide variation of the impurity levels is necessary as well as the comparative characterization of the large heat alloys. The purpose of this study is to clarify the precipitation behavior with heat treatment history and impurity levels for various large heats and model V-4Cr-4Ti alloys.

2-2-1. Preparation of the model alloys with the various oxygen and nitrogen levels

i) Fabrication of the model alloys

V-4Cr-4Ti model alloys doped with various levels of oxygen and nitrogen were fabricated by button arc melting. Each of them was melted on a laboratory scale (60 g). Raw vanadium large ingot was produced by industrial scale (25 kg) electron beam melting. Vanadium specimens with various oxygen and nitrogen levels were prepared by arc-melting, doping high-purity V_2O_5 powder and nitrogen gas, respectively. And then high-purity chromium and titanium were alloyed to 4 % in weight.

The prepared raw materials were alloyed by arc-melting for one minute in the arc conditions of 400 A and 16 V under argon environment. Before the melting, a vanadium getter material was arc-melted for one minute in the arc conditions of 420 A and 17.5 V to prevent the contamination from the environment and the tungsten electrode. The alloy specimens were overturned and melted for uniform melting. Finally, the back of the specimens was smoothened for 20 to 30 seconds in the arc conditions of 170 A and 15 V.

The chemical compositions of the V-4Cr-4Ti model alloys fabricated are shown in Table 2-3. The major difference in the composition among HP, VA-O-1 and VA-O-2 is

the level of oxygen. The other model alloys were made for examining the effect of nitrogen level.

Table 2-3 Interstitial impurity contents in the alloys used

Alloy Designation	Wt%		mass ppm		
	Cr	Ti	C	N	O
HP	3.94	3.81	75	88	44
VA-O-1	3.98	4.11	56	115	244
VA-O-2	3.95	3.94	89	125	513
VA-N-1	3.94	4.09	75	362	49
VA-N-2	3.92	3.89	86	734	46
VA-N-3	3.99	4.08	99	1070	74
NIFS-HEAT-1	4.12	4.13	56	103	181
US 832665	3.8	3.9	80	85	310

ii) Experimental procedures

The arc-melted buttons were cut into 10 mm thick slabs, followed by rolling process. HP, VA-O-1 and VA-N-10 were cold-rolled to a reduction of 90% in thickness. On the other hand, cracks occurred and propagated during the rolling in the case of VA-O-2, VA-N-2 and VA-N-3. The warm rolling at 673 K was carried out for these three specimens to a reduction of more than 80% in thickness.

Table 2-3 also shows the impurity levels of NIFS-HEAT-1 and US 832665, a 500 kg heat fabricated by the US-DOE program [49]. The thermomechanical treatments after melting for NIFS-HEAT-1 and US-DOE 832665 were hot forging, hot and cold rolling, and hot extrusion and warm rolling, respectively. The dimension of as-received NIFS-HEAT-1 and US 832665 was 10 mm and 4mm thick plate, respectively. The two large heats were cold-rolled to a reduction of 90% in thickness.

All the sheets including the model alloys were mechanically polished and electro-polished. Electro-polishing was performed for 4 minutes and 30 seconds below 10 degrees centigrade in the electrolytic solution of 20% sulphuric acid and 80% methanol, followed by annealing at 1373 K for an hour in a vacuum ($<10^{-6}$ Torr.) to

dissolve the impurities and for removal of dislocations introduced by cold rolling. The specimens were then heat-treated again from 873 to 1373 K for an hour to investigate the impurity behaviour. Vickers hardness testing and microstructure observation with optical microscope, scanning electron microscope (SEM) and transmission electron microscope (TEM) were carried out after annealing.

2-2-2. Effect of the annealing temperature on hardness change and microstructural developments

Fig. 2-12 shows the hardness of oxygen-doped V-4Cr-4Ti model alloys and two large heats, NIFS-HEAT-1 and US 832665, as a function of heat treatment temperature. For these alloys, the nitrogen and carbon levels ranged from 85 to 125 mass ppm and from 56 to 80 mass ppm, respectively. As shown in Fig. 2-12, the hardness has its peak at 973 K for all alloys. In model alloys, hardness increased with increasing the oxygen level. On the other hand, the peak hardness of the two large heats has an opposite dependence on the oxygen level.

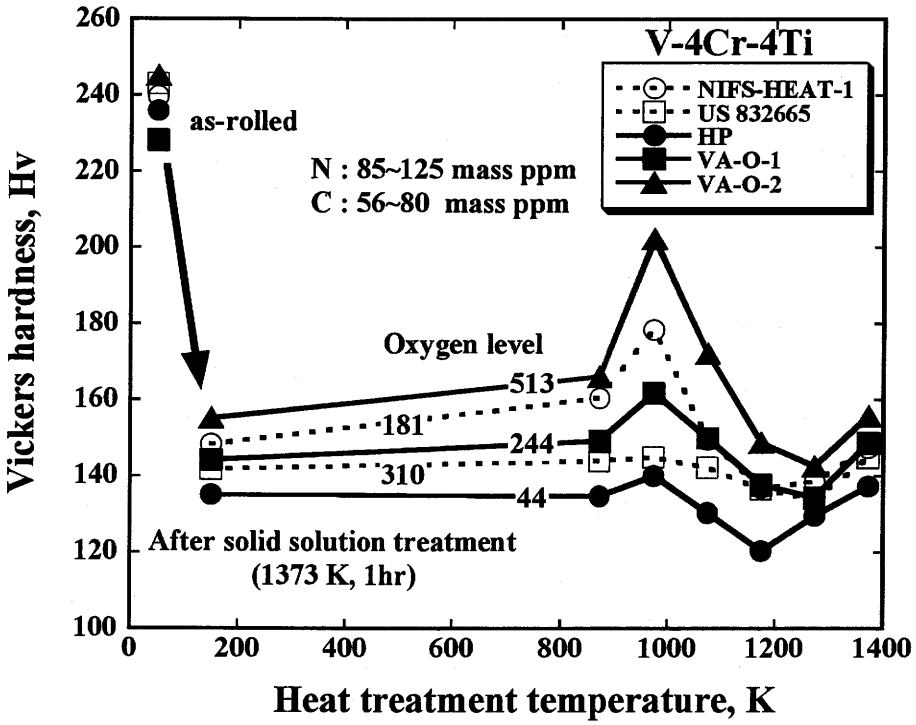

Fig. 2-12 Effect of heat treatment temperature on hardness for alloys with various oxygen levels.

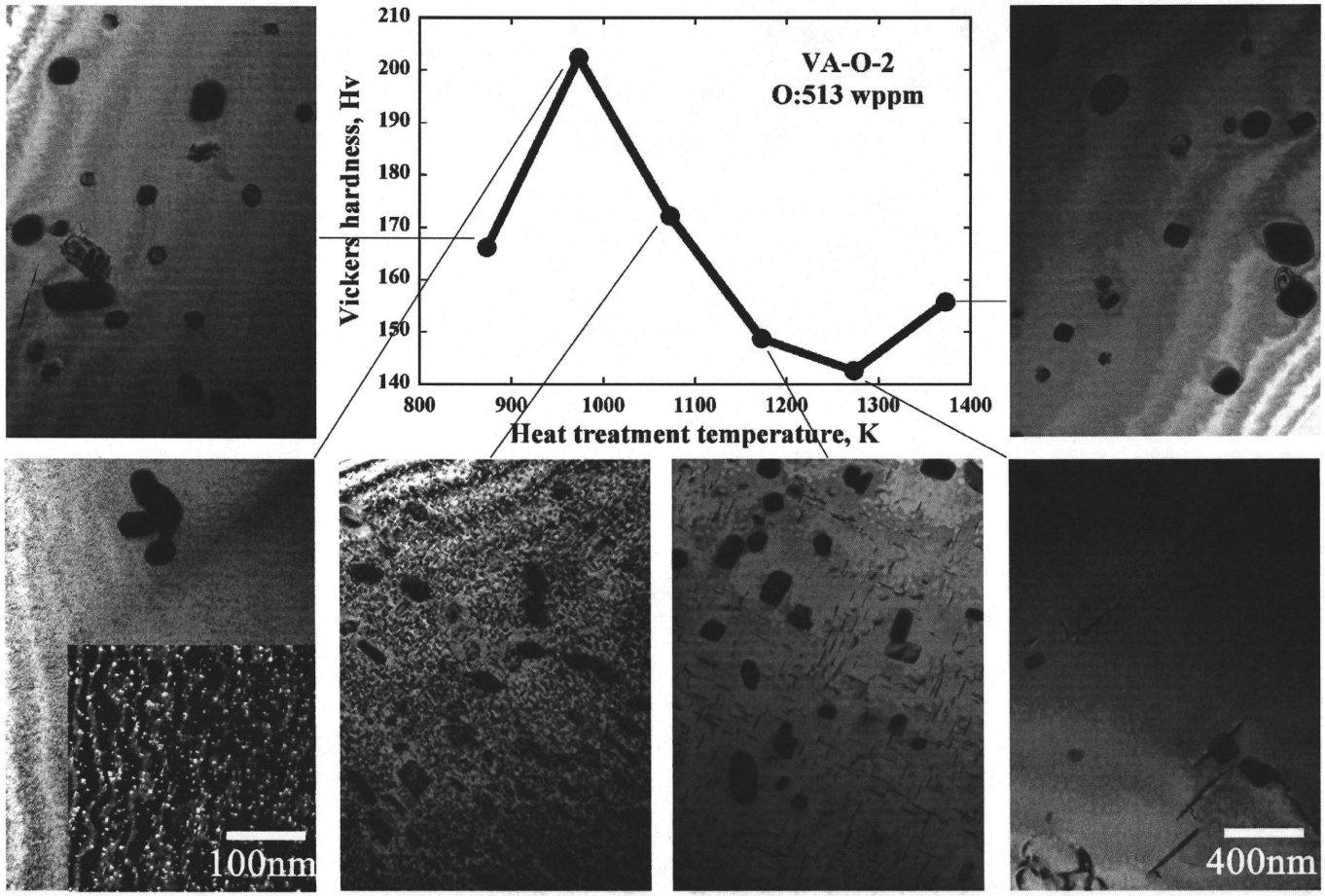

Fig. 2-13 Hardness and microstructure with heat treatment temperature in VA-O-2.

The peak of hardness was identified at 973 K, where fine precipitates appeared.

Fig. 2-13 indicates the relation between hardness change and microstructure development with the heat treatment temperature for VA-O-2. Two kinds of precipitates, large and fine ones, were observed, as shown in Fig. 2-13. The hardness was highest at 973 K when a high density of fine precipitates was observed. The hardness decreased with annealing temperature above 973 K, which corresponds to the coarsening and the decrease in the precipitate density. Heat treatment at 1373 K resulted in disappearance of the fine precipitates and an increase in hardness. On the other hand, large precipitates were observed in all cases of the heat treatment temperatures from 873 to 1373 K.

Fig. 2-14 shows the hardness of nitrogen-doped V-4Cr-4Ti alloys as a function of heat treatment temperature. Unlike the oxygen-doped model alloys, the hardness peak was not observed by annealing at any temperature. Hardness did not change significantly with annealing temperature.

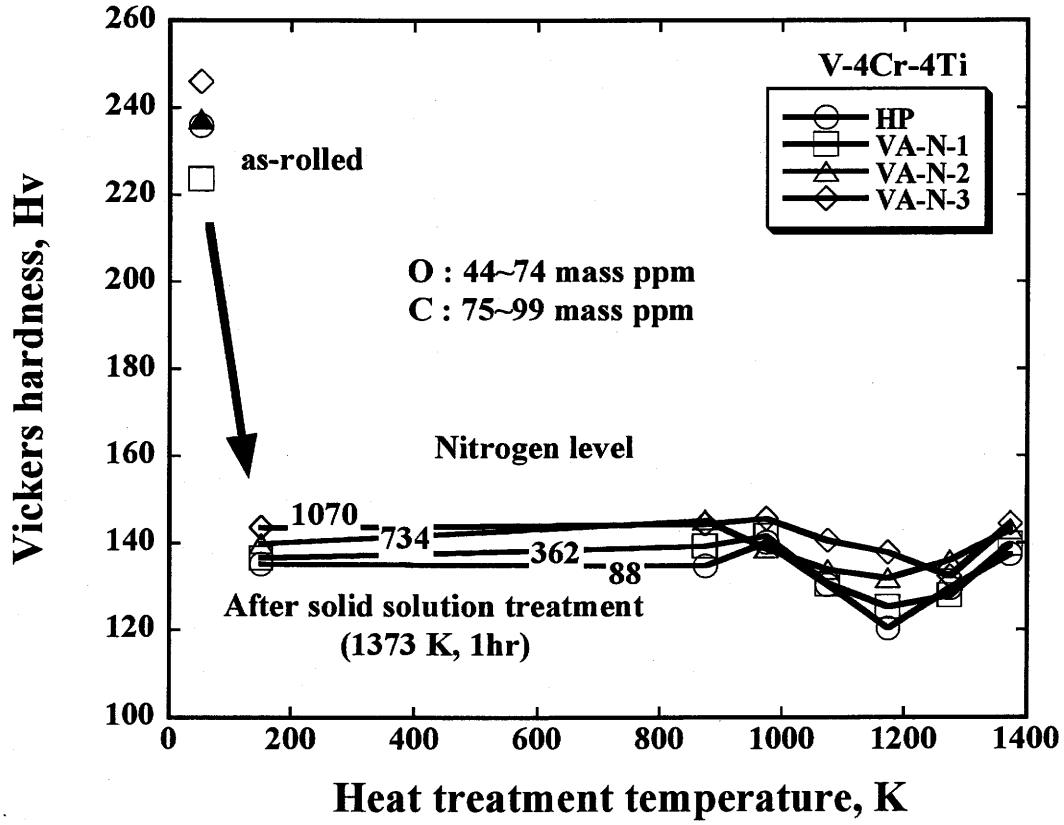

Fig. 2-14 Effect of heat treatment temperature on hardness for alloys with various nitrogen levels.

Fig. 2-15 shows the dark and bright field TEM images of the model alloys annealed at 973 K. Fine precipitates were formed by annealing at 973 K in VA-O-1and VA-O-2, which are the oxygen-doped alloys. However, the fine precipitates were not observed for HP and the nitrogen-doped V-4Cr-4Ti model alloys, VA-N-2 and VA-N-3, where oxygen level is low, as shown in Table 2-3.

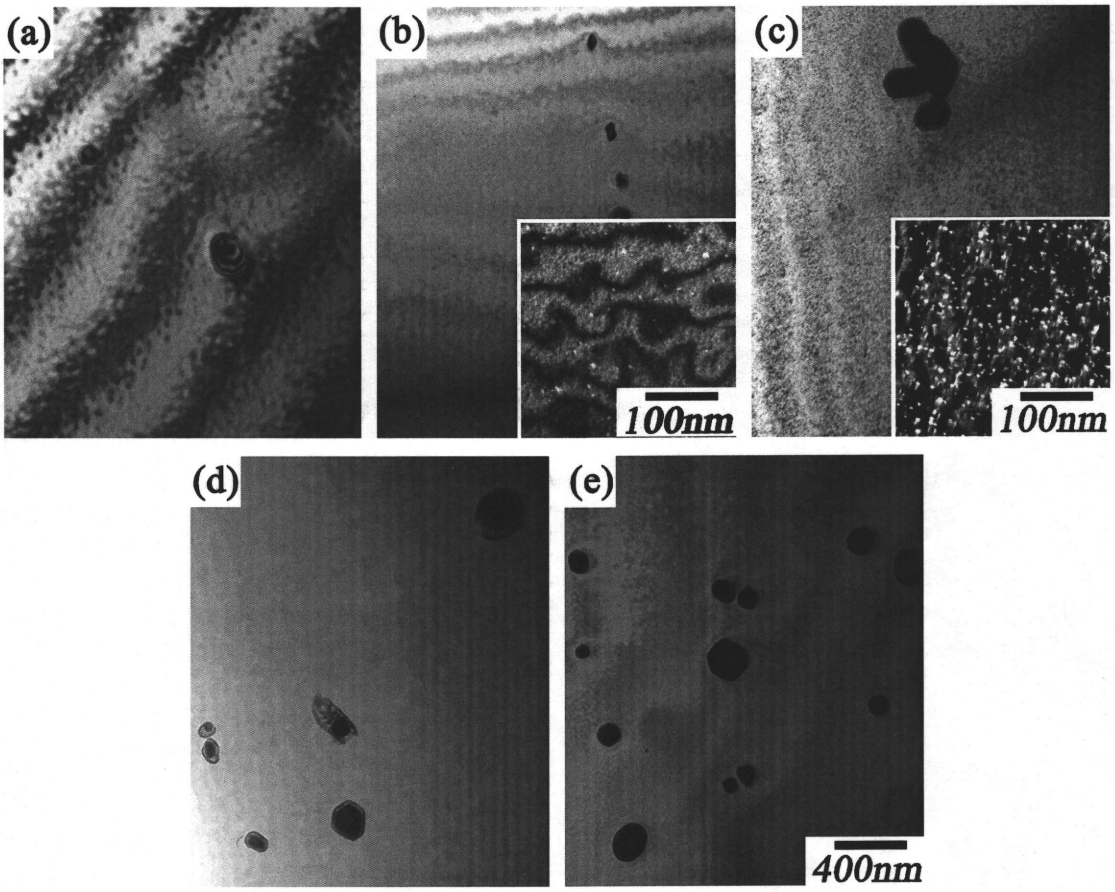

Fig. 2-15 Dark and bright field TEM images of the oxygen-doped and nitrogen-doped model alloys annealed at 973 K. (a) HP (b)VA-O-1 (c) VA-O-2 (d) VA-N-2 (e) VA-N-3

Fig. 2-16 shows the microstructural developments with the heat treatment temperature for the large scale heats, (a) NIFS-HEAT-1 and (b) US 832665. In the two alloys, the fine precipitates were formed by annealing at 973 K, and the growth of the fine precipitates occurred with the increase in the heat treatment temperature,. The fine precipitates, which were observed from 973 to 1273 K, disappeared by annealing at 1373 K.

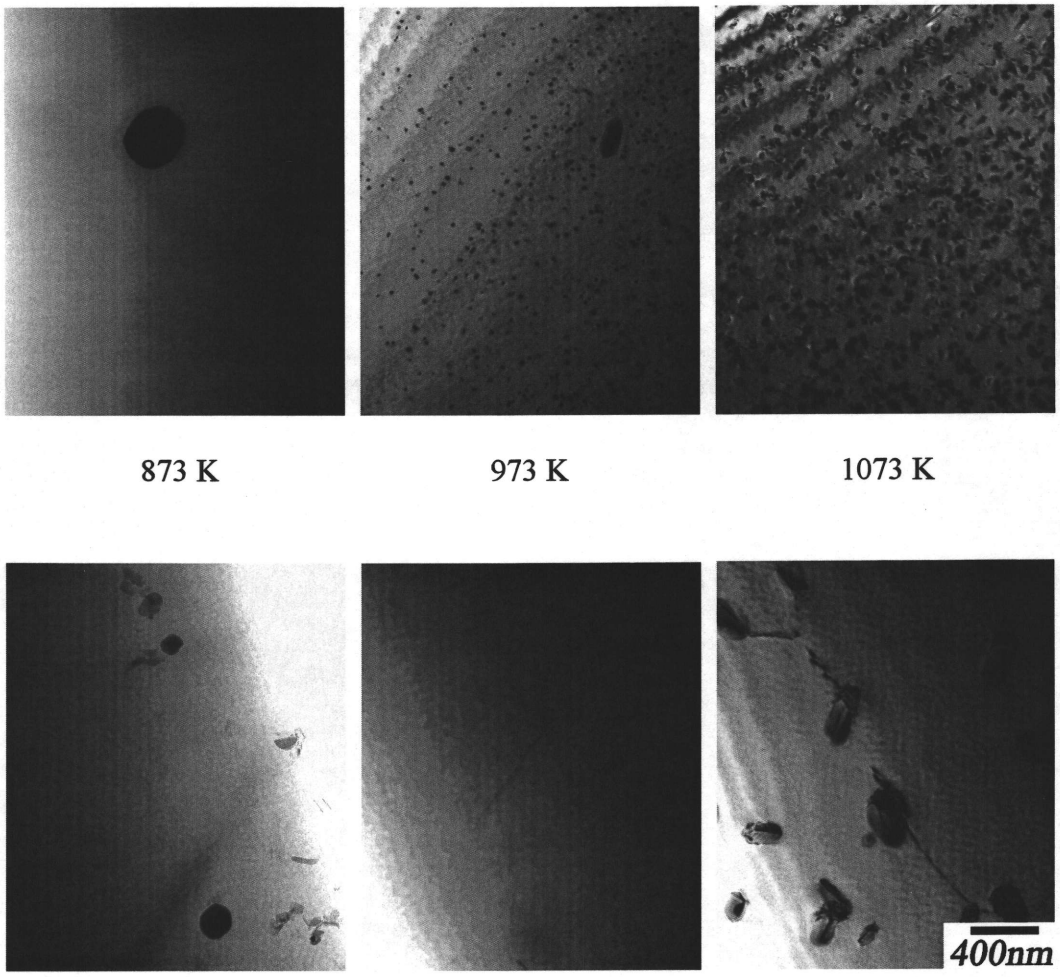

Fig. 2-16 Microstructural developments with the heat treatment temperature for the large scale heat, (a) NIFS-HEAT-1.

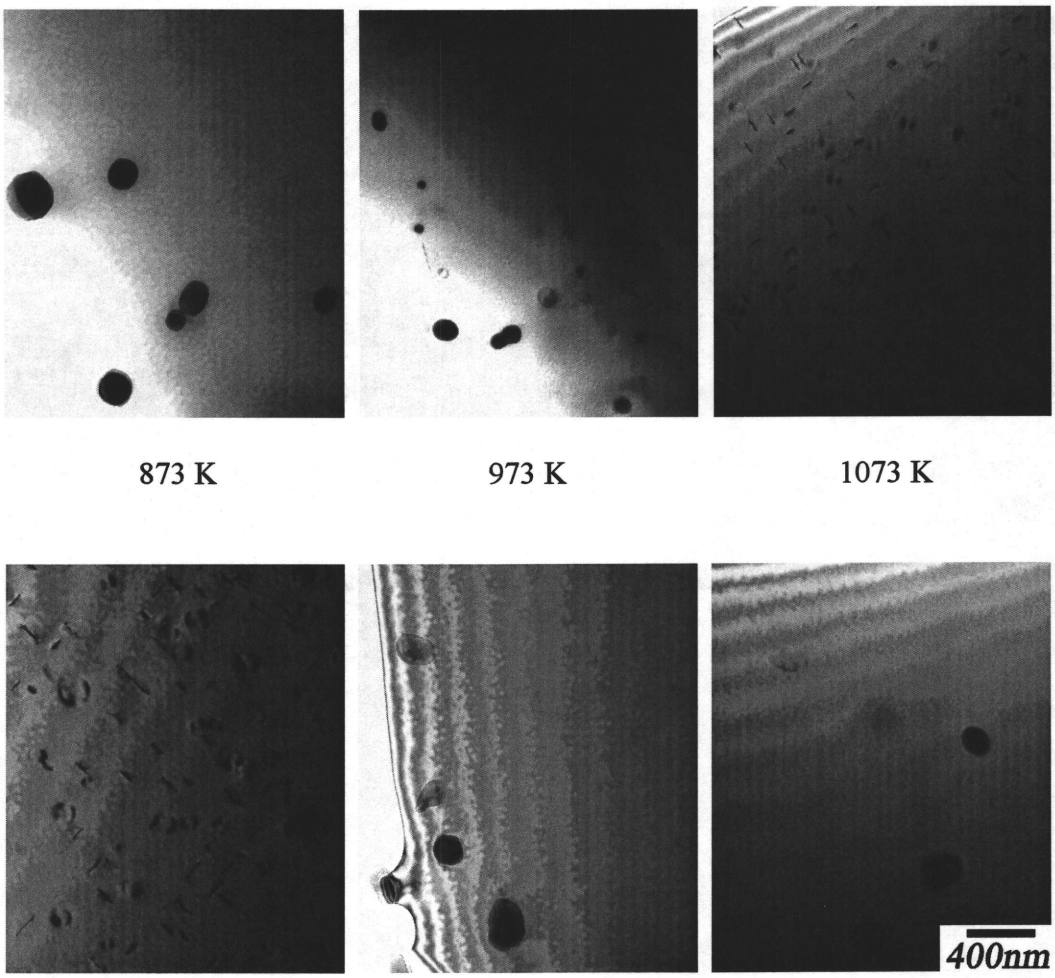

Fig. 2-16 Microstructural developments with the heat treatment temperature for the large scale heat, (b) US 832665.

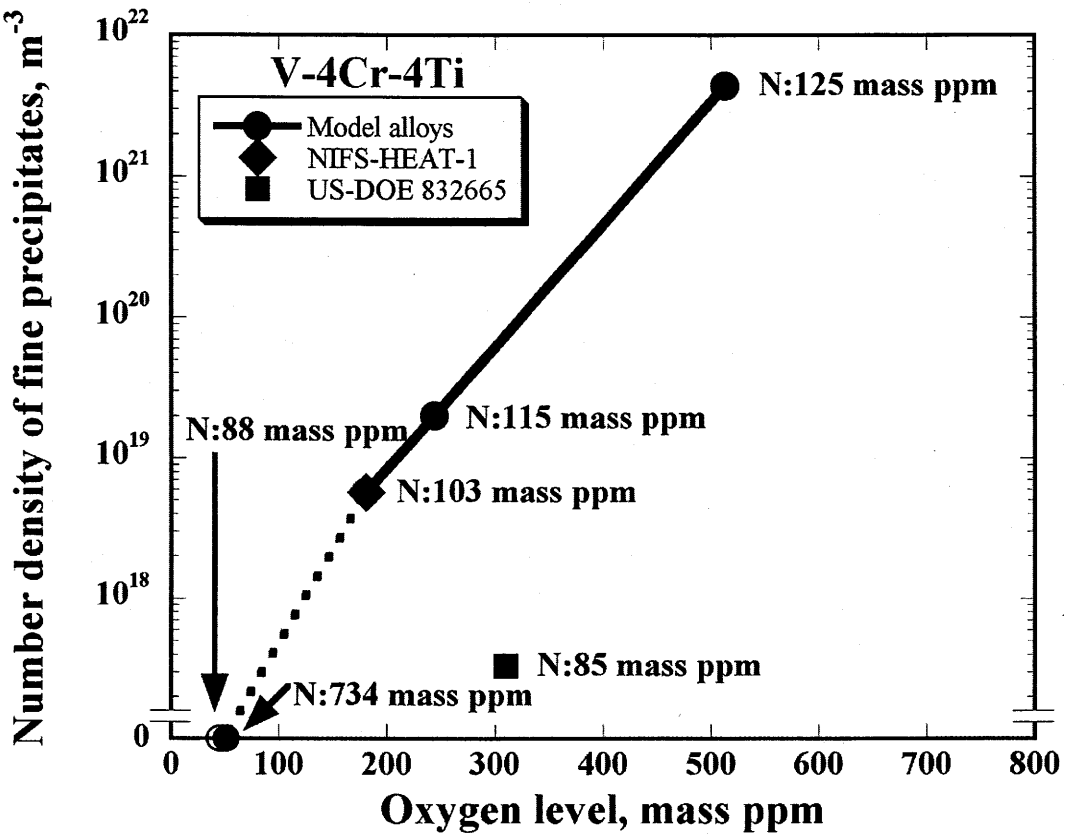

Fig. 2-17 Number density of the fine precipitates with oxygen and nitrogen levels of V-4Cr-4Ti annealed at 973 K.

Fig. 2-17 indicates the number density of the fine precipitates, derived from the TEM micrographs shown in Fig. 2-13, 15 and 16, with oxygen levels for the V-4Cr-4Ti model alloys annealed at 973 K. In model alloys, the density of the fine precipitates, which were shown in Fig. 2-15 and 2-16, increased with increasing the oxygen level. However, the density of the fine precipitates did not change in the nitrogen-doped models.

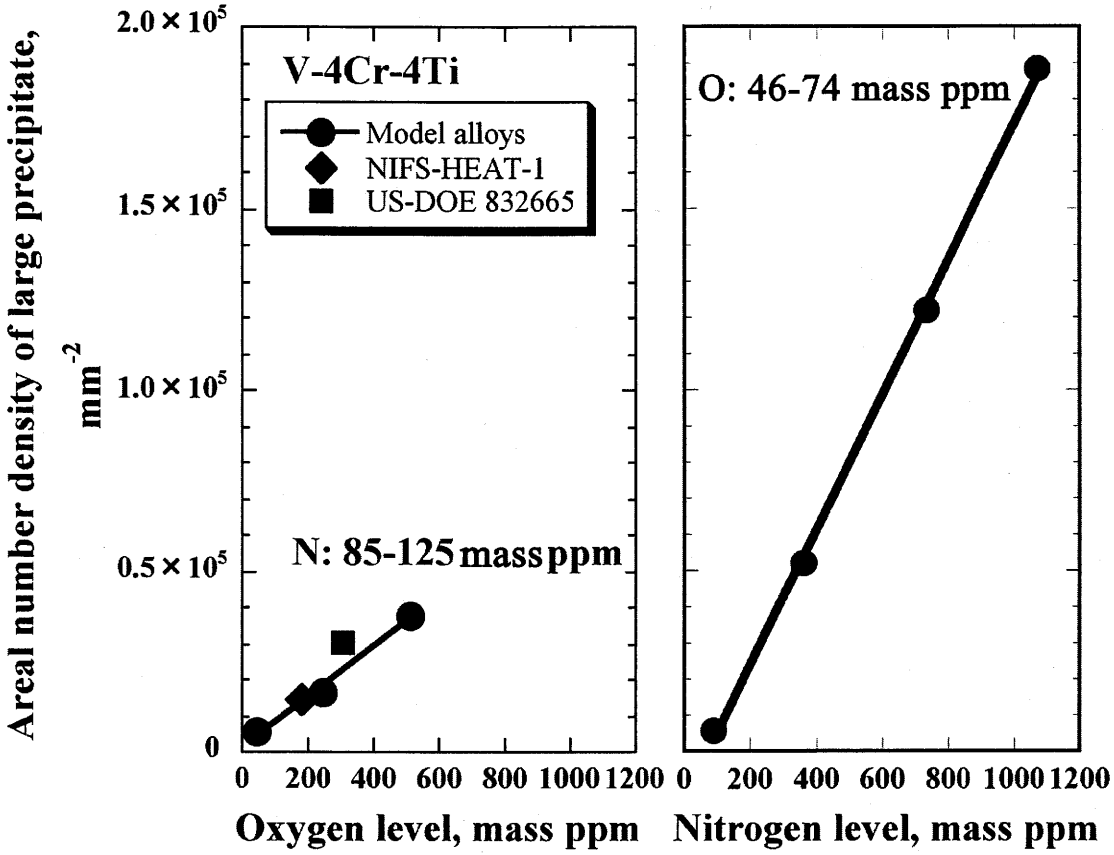

Fig. 2-18 Change of large precipitates with oxygen and nitrogen levels for model V-4Cr-4Ti alloys annealed at 1373 K.

Fig. 2-18 indicates the change of the areal number density of the large precipitates, with oxygen and nitrogen levels for V-4Cr-4Ti alloys annealed at 1373 K. The areal number density of the precipitates increased linearly with increasing the impurity levels. The change in the areal number density of precipitate for nitrogen-doped V-4Cr-4Ti alloys was larger than that of the oxygen-doped V-4Cr-4Ti alloys.

Fig. 2-19 is the results of the SEM-EDS line analyses on the large precipitates in HP, VA-O-2, VA-N-3 and NIFS-HEAT-1, after annealing at 1373 K for one hour. In all the specimens, the peak of Ti, C, N and O was observed. Especially, the peak of O and N in VA-O-2 and VA-N-3 was higher than those of other impurities, respectively.

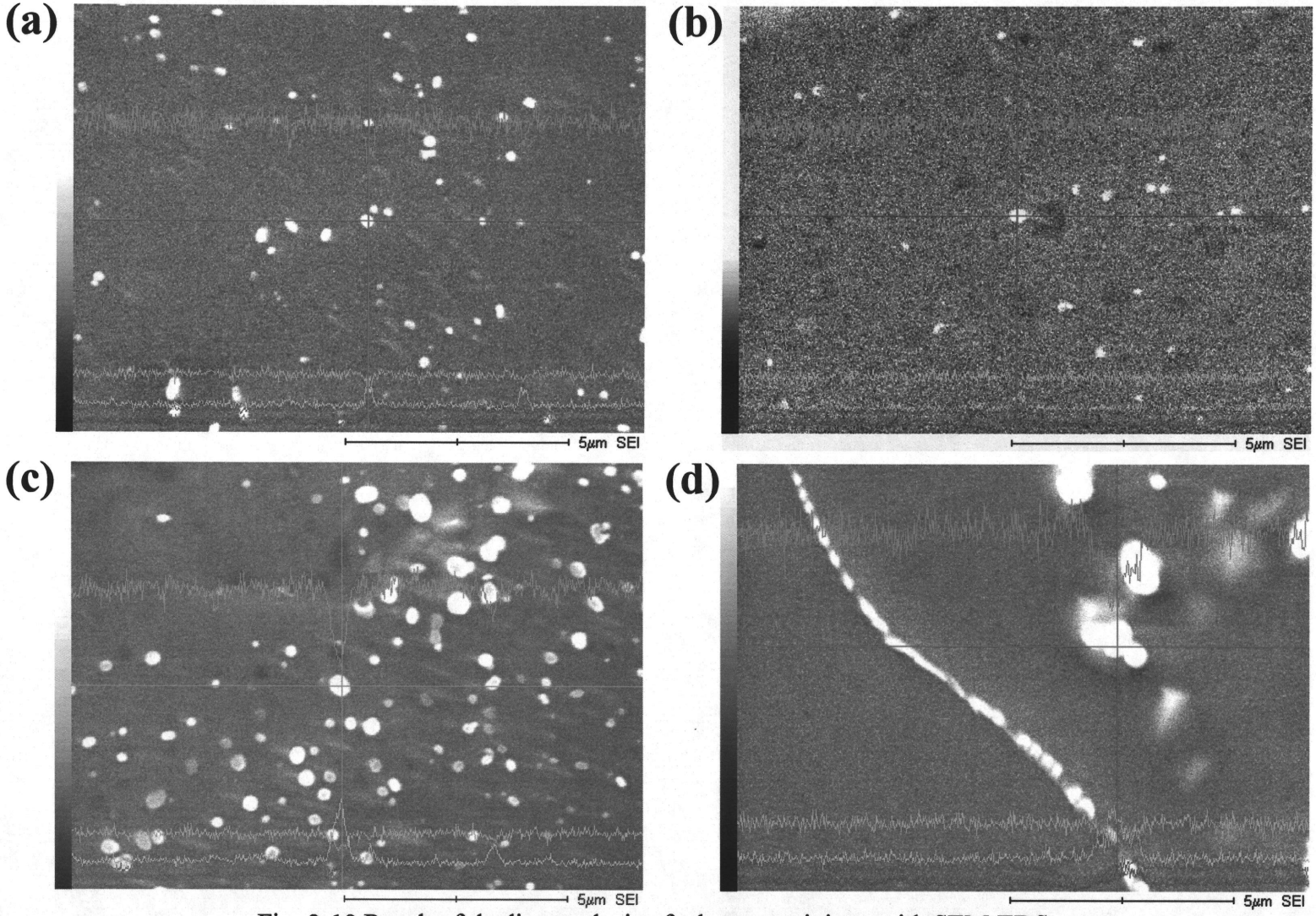

Fig. 2-19 Result of the line analysis of a large precipitate with SEM-EDS.
(a) HP (b) VA-O-2 (c) VA-N-3 (d) NIFS-HEAT-1

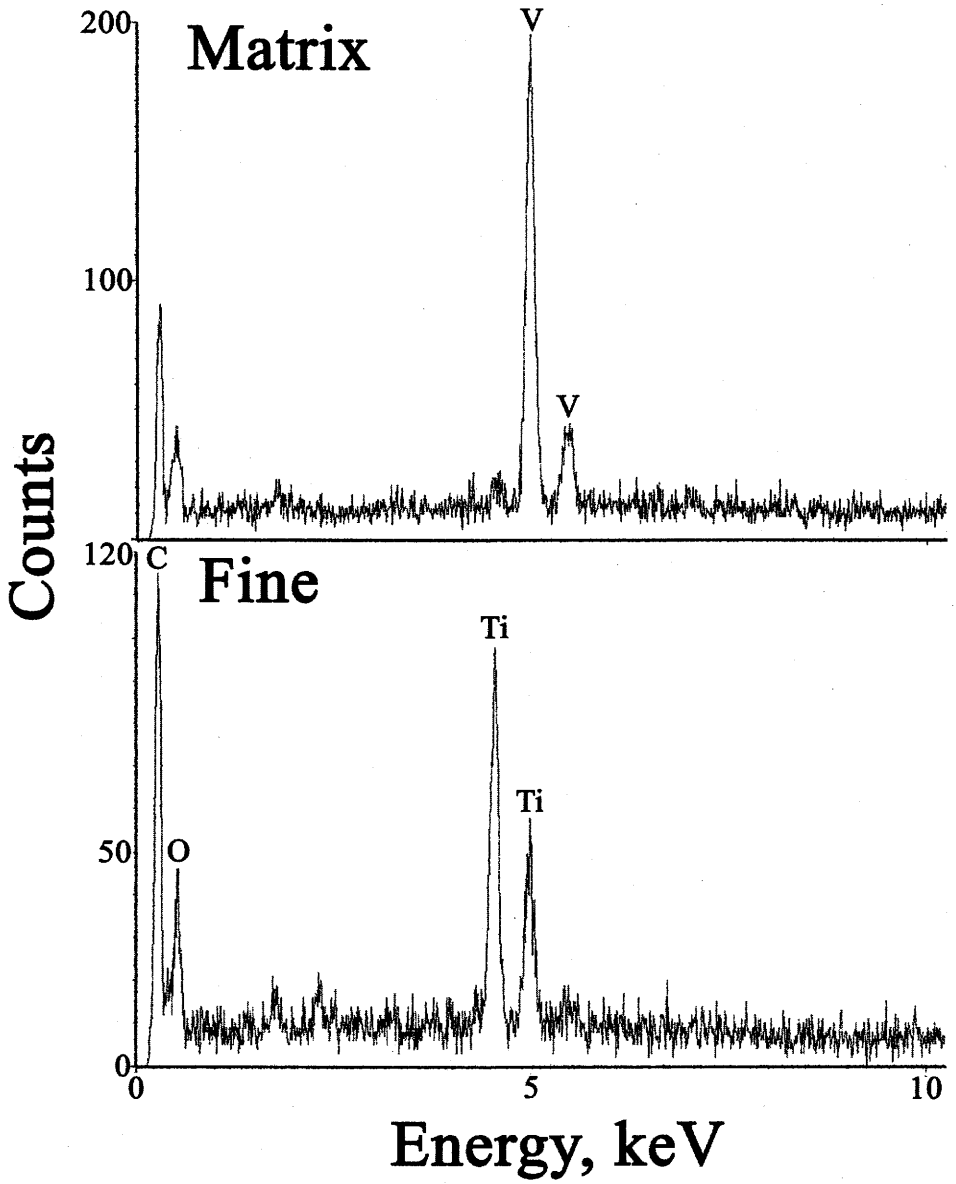

Fig. 2-20 TEM-EDS analysis of the matrix and a fine precipitates in VA-O-2 annealed at 1173 K for one hour.

Fig. 2-20 indicates the results of the TEM-EDS analyses of the matrix and a fine precipitate in the VA-O-2 annealed at 1173 K for one hour. The peak of vanadium, C and O was observed in the matrix. On the other hand, the peak of Ti, C and O in a fine precipitate was much higher than that of the matrix. Fig. 2-20 indicates that the fine precipitates are Ti-C-O complexes.

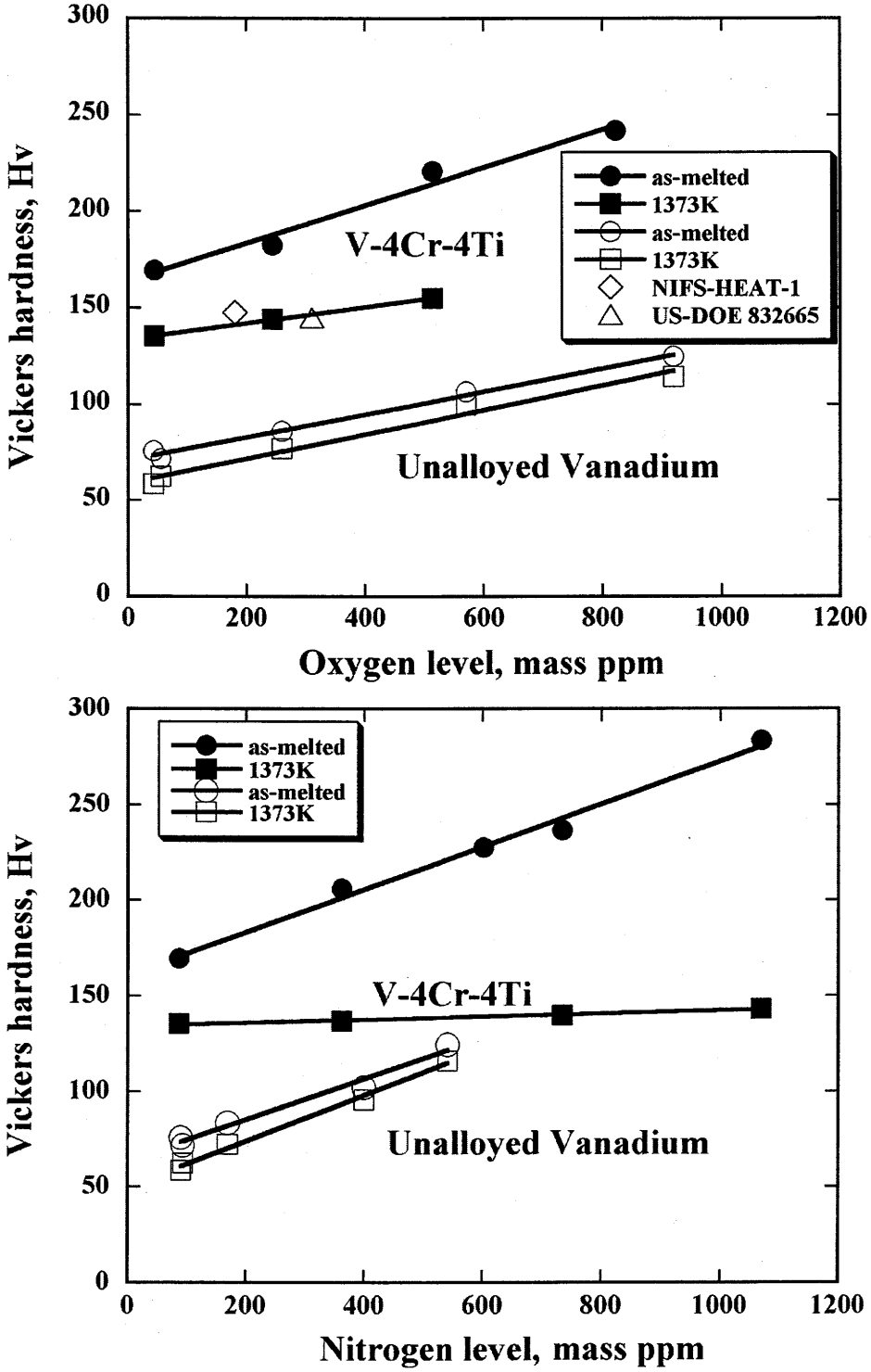

Fig. 2-21 Effect of oxygen and nitrogen level on the hardness.

2-2-3. Discussions: Impurity behavior in V-4Cr-4Ti alloys

Fig. 2-21 compares the effect of oxygen and nitrogen level on hardness in model V-4Cr-Ti alloys as melted and as annealed at 1373 K. The data for unalloyed vanadium were also plotted for comparison. In the as melted conditions, the increment in hardness with the increase in the oxygen and nitrogen levels for unalloyed and alloyed vanadium was similar. Fig. 2-21 shows that the increase in hardness with the oxygen level after annealing at 1373 K is smaller than that for as-melted condition in the case of V-4Cr-4Ti, although the hardness for the two heat treatment conditions is almost the same in the case of unalloyed vanadium. For V-4Cr-4Ti, the increase in hardness with the nitrogen level after annealing at 1373 K is even smaller. The reason for the reducd effect of the oxygen and nitrogen level on the hardness in the case of annealing at 1373 K is that the large precipitates, in which oxygen or nitrogen was contained as shown in Fig. 2-19, were formed during initial process of its fabrication and stabilized by annealing at 1373 K. The difference in the dependence of the hardness on oxygen and nitrogen levels is considered to imply a difference in the impurity level in the matrix. The positive dependence of the hardness on oxygen level suggests that some fraction of oxygen should be in solid solution in the matrix after annealing at 1373 K. Fig. 2-12 and 2-20 show that the fine precipitates were mainly composed of Ti, C and O, and their formation and dissolution resulted in the hardness change with annealing temperatures. This fact indicates some fraction of O exists in the matrix after annealing at 1373 K. Note that the fine precipitates are dissolved at 1373 K as shown in Fig. 2-13 and 2-16. The resolution of the fine precipitates is thus thought to be the source of the oxygen at 1373 K, resulting in the additional hardening by solid solution of oxygen into the matrix.

Very weak dependence of the hardness on nitrogen level suggests that almost all nitrogen should be contained in the large precipitates. This idea of the impurity partitioning into large and fine precipitates is consistent with the experimental results shown in Figs. 2-12 to 2-20.

For the two large heats, NIFS-HEAT-1 and US 832665, oxygen level of US 832665 is higher than that of the NIFS-HEAT-1. However, the density of fine precipitates of US 832665 formed by annealing at 973 K was lower than that of the NIFS-HEAT-1, as

shown in Fig. 2-17, which resulted in decrease in the degree of hardening, as shown in Fig. 2-12. The reason seems that compared with NIFS-HEAT-1, US 832665 was more repeatedly annealed at 1323-1343 K during the rolling procedures. It is known that the large precipitates were formed during these procedures [22-24]. Repeated annealing may have resulted in increase in the density of large precipitates, in which impurities (C, N and O) are contained, as shown in Fig. 2-18. As the result, impurity level in the matrix of US 832665 may become lower than that of the NIFS-HEAT-1.

2-2-4. Summaries

The effect of impurity levels on hardness and precipitation behavior by heat treatment after solid solution treatment at 1373 K was investigated for some model and large heat V-4Cr-4Ti alloys with different oxygen and nitrogen levels.

1. Large and fine precipitates were observed in the matrix. The large precipitates are stable in all heat treatments to 1373 K, but the fine precipitates appeared at 973 K and vanished at 1373 K. The main composition of the fine precipitates was Ti, C and O.

2. The density of the large precipitates increased with nitrogen level.

3. The hardness after annealing at 1373 K is a positive and a very weak function of oxygen and nitrogen level, respectively, implying that some fraction of the oxygen is in solid solution and most of the nitrogen is in the large precipitates.

4. These data show that, in V-4Cr-4Ti alloys, most of the nitrogen impurities are included into the large precipitates by annealing at 1373 K and are stable during the following heat treatments. Some fraction of the oxygen impurities will be in large and fine precipitates. The oxygen in the fine precipitates will be released into matrix by annealing at 1373 K, resulting in the increase in hardness.

5. The two large heat alloys are different from the model alloys in the dependence of precipitation and hardness on the impurity levels. The history of the thermomechanical treatment may be responsible for the difference.

2-3. Summary of the impurity behavior in vanadium alloys

The understanding of the impurity behavior under the thermomechanical treatment processes is very important for optimizing the fabrication and the thermomechanical treatment conditions. The separated effect of the impurities on the hardness and the precipitation behavior by heat treatment after solid solution treatment at 1373 K or cold rolling was clarified and summarized in Fig. 2-22 and 2-23.

Two kinds of precipitates were observed at 1273 K. From the TEM analysis, larger precipitates were identified to be Ti-rich and smaller were Ti-C-O compounds. Ti-C-O precipitates are stable at 973 to 1273 K. Ti-rich precipitates were observed up to 1473 K, and vanished by annealing at 1573 K.

Impurities exist in the Ti-rich precipitates and in the matrix after the hot/cold rolling or solid solution heat treatment. Oxygen and carbon seems to be in the Ti-rich precipitates and in the matrix. On the contrary, nitrogen is likely to be almost in the Ti-rich precipitates. Oxygen and carbon existing in the vanadium alloys were combined with Ti and formed the fine precipitates, Ti-C-O, resulting in the hardness peak at 973 K. The formation of these fine precipitate is attributed to the hardening of the vanadium alloys, induced by the precipitate hardening. Hardness was recovered with increasing the annealing temperature due to the decrease in the density of the precipitates.

At temperature of 1373 K, re-solution of Ti-C-O precipitates resulted in the re-distribution of oxygen and carbon: oxygen was re-dissolved into the vanadium, resulting in the increase in hardness and carbon was combined with vanadium and precipitated on the grain boundaries.

Ti-rich precipitates were also dissolved by annealing at 1573 K. Some fraction of the impurities existing in the Ti-rich precipitates was dissolved into the matrix and other formed the V (CNO) on the grain boundaries. Thus, the increase in hardness and the degradation of the mechanical properties is attributed to increase in the impurity level of vanadium, derived from the re-solution of the Ti-rich precipitates. The formation and growth of the precipitates on grain boundaries also may be harmful to the mechanical properties. Hence, thermomechanical and annealing temperature will be optimized at 1273 K or below according to the balance between the precipitation hardening and the solid solution hardening.

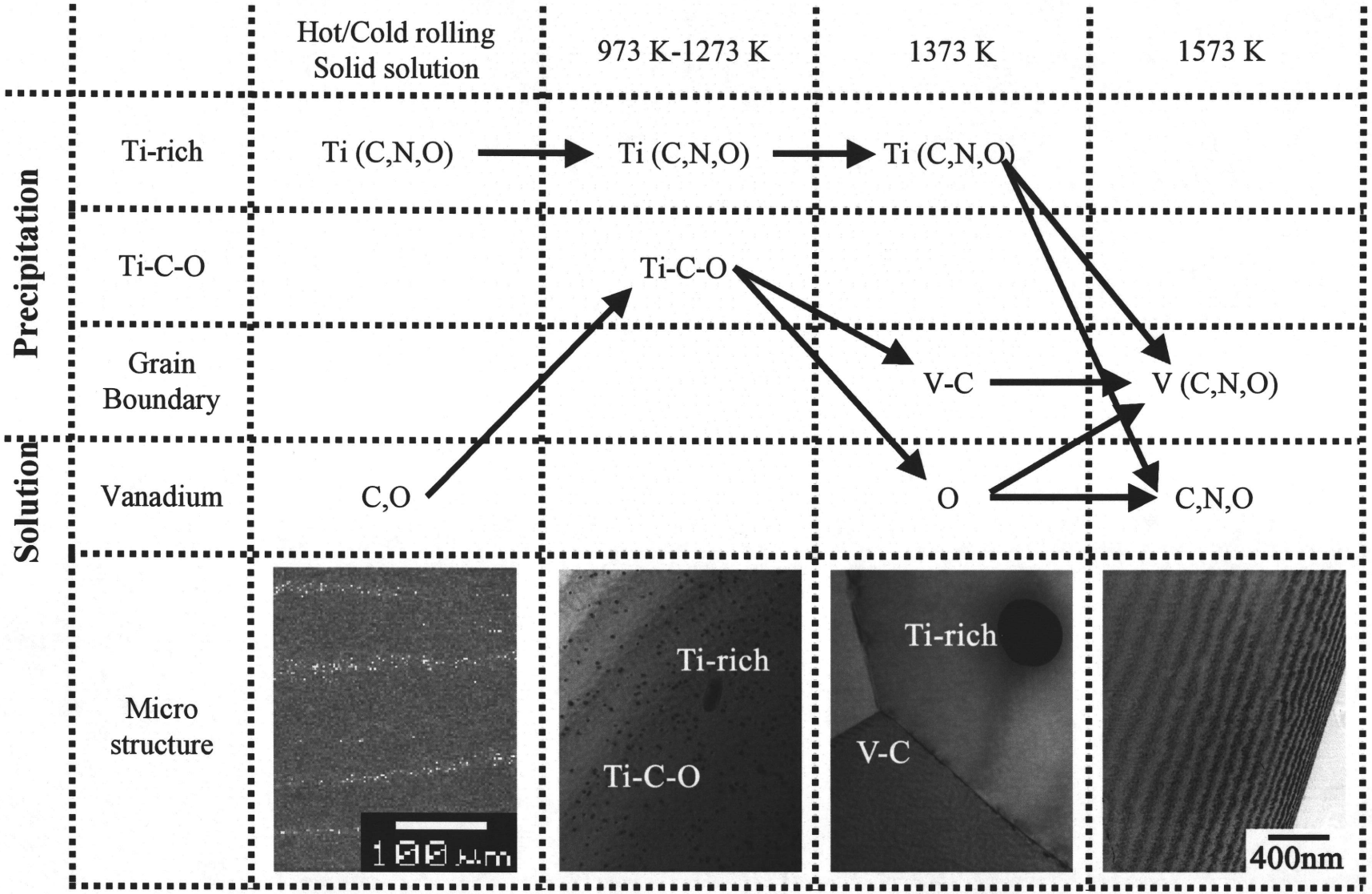

Fig. 2-22 Effect of the impurity behavior on the microstructural development.

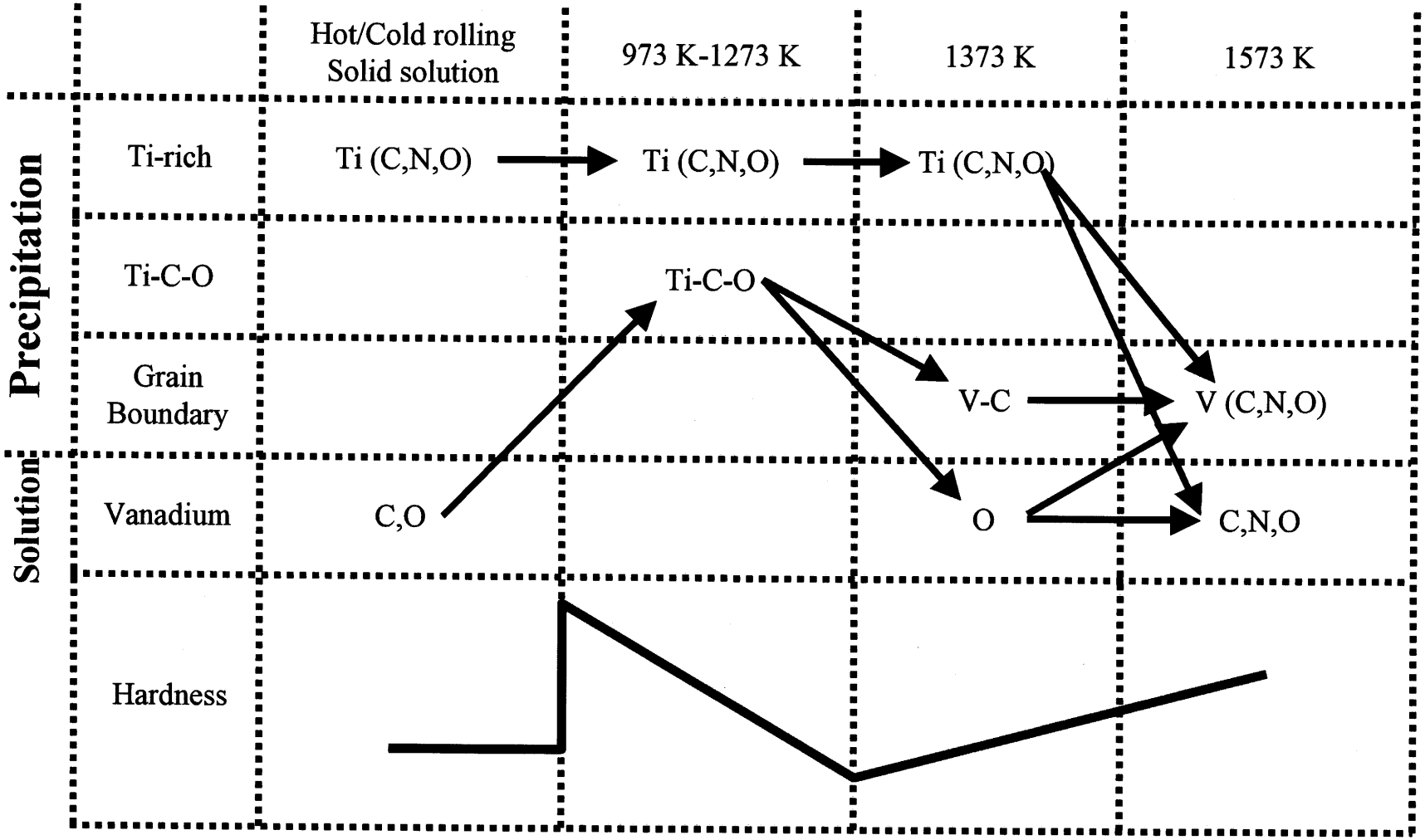

Fig. 2-23 Effect of the impurity behavior on hardness.

CHAPTER 3

Establishment of the Welding Technology for Vanadium Alloys using YAG Laser

3-1. Development of the laser welding technology for pure vanadium and its alloys

3-1-1. Control of welding environments

i) Fabrication of the environmental control box

To prevent the contamination with interstitial impurities, such as hydrogen, oxygen, nitrogen, carbon, etc. an environmental control box capable of supplying high-purity argon gas (99.9999%), and ventilating the fume was designed and fabricated, as shown in Fig. 3-1. The environmental control box has two nozzles for cleaning the specimen and two gas suppliers for substitution of the atmosphere. The gas introduced through the nozzles 1 and 2 blows out the fume produced during the welding process on the top (nozzle 1) and the bottom (nozzle 2) surface, respectively.

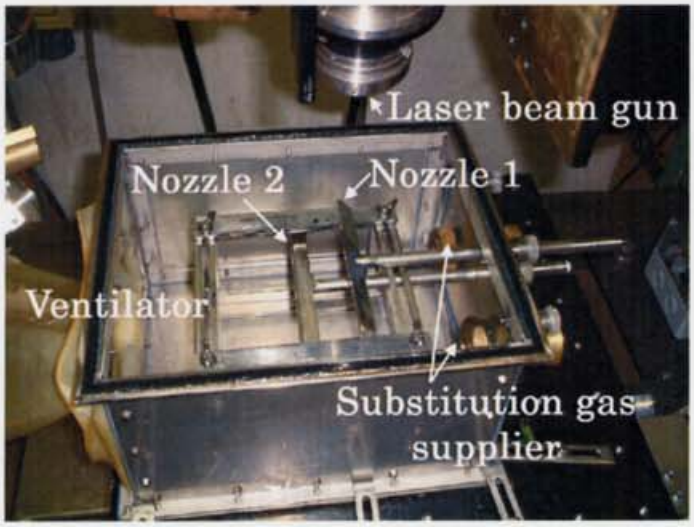

Fig. 3-1 Inside of an environmental control box designed and fabricated for the present experiment.

ii) Experimental procedures

In this study, the specimen plates of 4 mm thick are prepared for laser welding by cold-rolling unalloyed vanadium to the reduction of 60% in thickness and 4-mm-thick high-purity V-4Cr-4Ti alloy, NIFS-HEAT-2, annealed at 1273 K for two hours.

Unalloyed vanadium was chosen as a material because the hardness of unalloyed vanadium is sensitive to the impurity level and was evaluated systematically [55].

During the welding, each nozzle supplied argon gas from 50 to 200L/min. The flow rate of the substitution gas varied from zero to 500 L/min in total. The laser beam came in the box through the quartz glass window with the thickness of 2.3 mm.

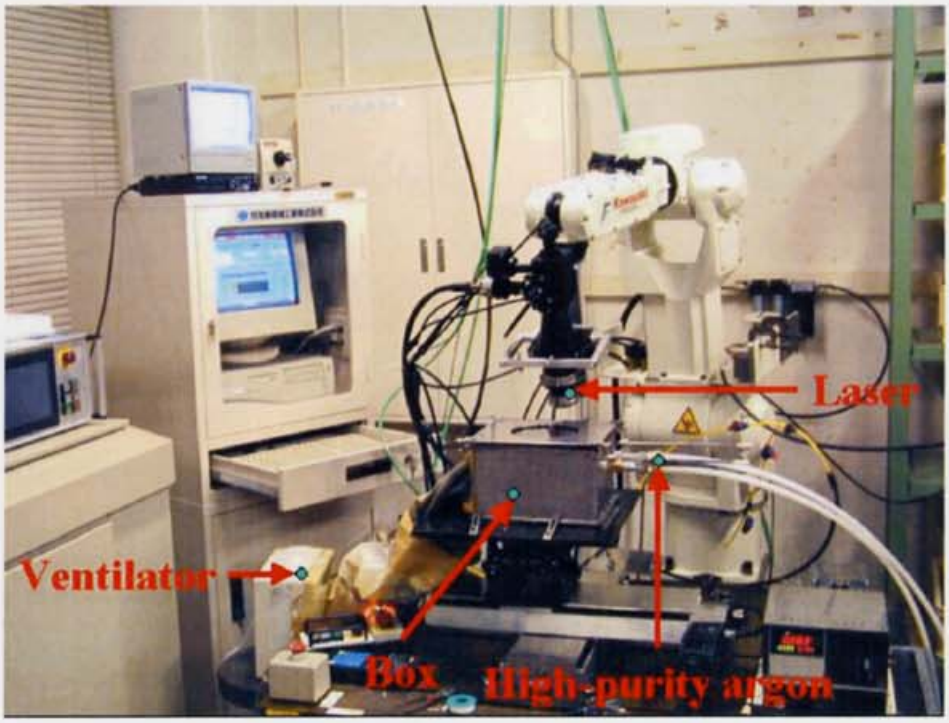

Fig. 3-2 YAG laser welding apparatus used in the present study.
This machine is in the Hiroshima University.

In the case of unalloyed vanadium, bead-on-plate welds were produced on the 4 mm-thick plate, using 2.0 kW YAG laser machine, as shown in Fig. 3-2, on the welding condition of 1.8kW continuous wave and traveling speed of 0.5 m/min. In the case of NIFS-HEAT-2, the laser welding was performed under the welding condition of the average power of 1.8 kW and traveling speed of 0.2 m/min. Focal point was positioned at the surface of the specimen, in which spot size of the laser light was 0.5 mm in diameter.

To estimate the pickup of interstitial elements in the weldments, chemical analysis

and hardness measurement after the post-weld heat treatment at 673 and 1273 K for an hour were carried out. Hardness was measured on the condition of load of 100 gf and loading time of 30 seconds. Microstructural observations were also carried out.

3-1-2. Effect of environmental control on the contaminations during the welding

i) Effect of the flow rate of the substitution gas on hardness

Fig. 3-3 shows the outward appearance of the beads for three welding environments. When welded in the air and with supplying the argon gas of 50 L/min each with two nozzles, the bead was colored due to contamination with impurities. However, by use of the additional supply of the substitution gas of 300 L/min the color due to the contamination was not detected.

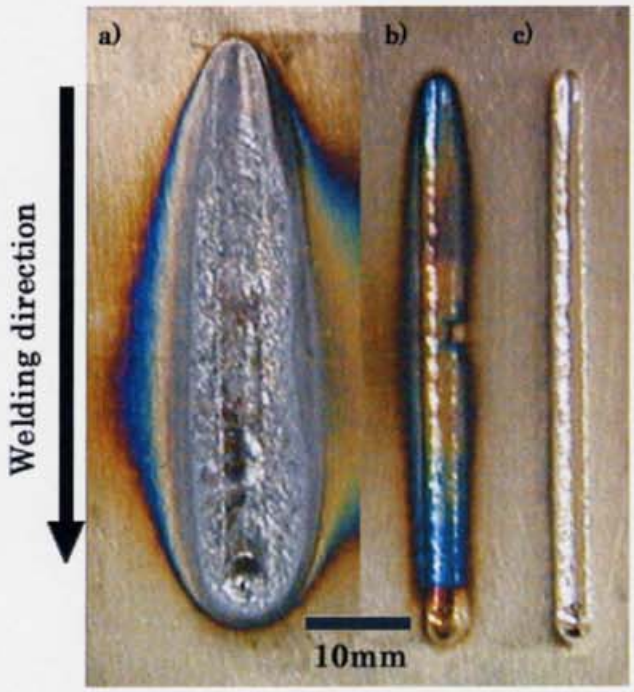

Fig. 3-3 The outward appearance of the weld beads for three cases of the welding environment.

a) in the air

b) nozzles:100 L/min, substitution:0 L/min

c) nozzles:100 L/min, substitution:300 L/min

Fig. 3-4 shows the cross sectional microstructure of the weld zone on the condition of the laser power of 1.8 kW and welding speed of 0.5 m/min. Microstructure observation showed that the grains in the weldment are elongated as a result of the heat transfer during the re-solidification. On the other hand, the grains in heat-affected zone (HAZ) are smaller and equiaxed. The penetration depth was about 2.4 mm, and porosities were observed at the bottom of the weldment.

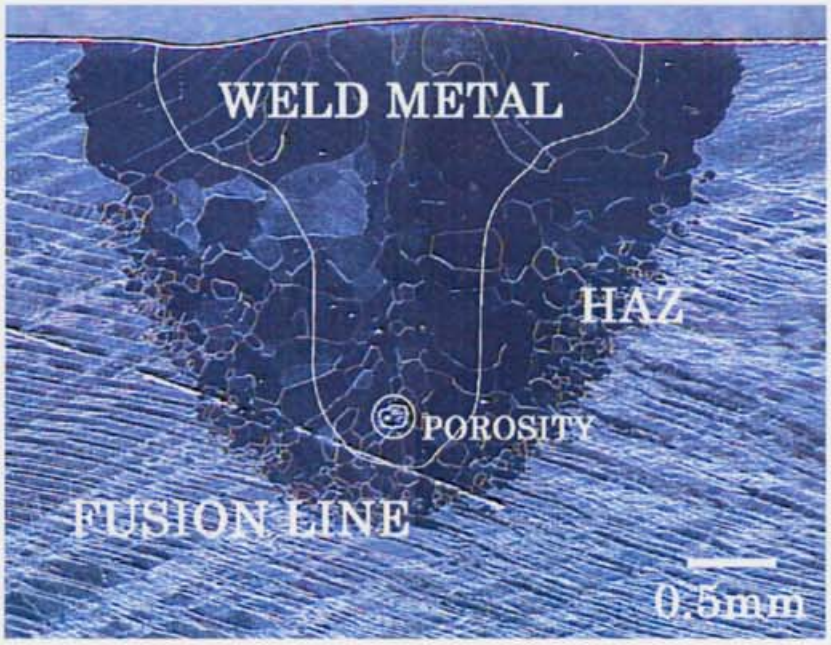

Fig. 3-4 Cross sectional microstructure of the weld zone.

Fig. 3-5 indicates the hardness change with the depth into weld zone from the surface of the bead. Hardness was measured at the center of the bead. Fig. 5 indicates that there was little change in hardness above the flow rate of the substitution gas of 100 L/min. The relatively small variation in hardness to the depth of 2.2 mm from the surface followed by a sudden drop, in the case without the substitution gas supply, implies that impurities introduced from the surface during the welding were almost homogeneously distributed as a result of mixture driven by thermal convection.

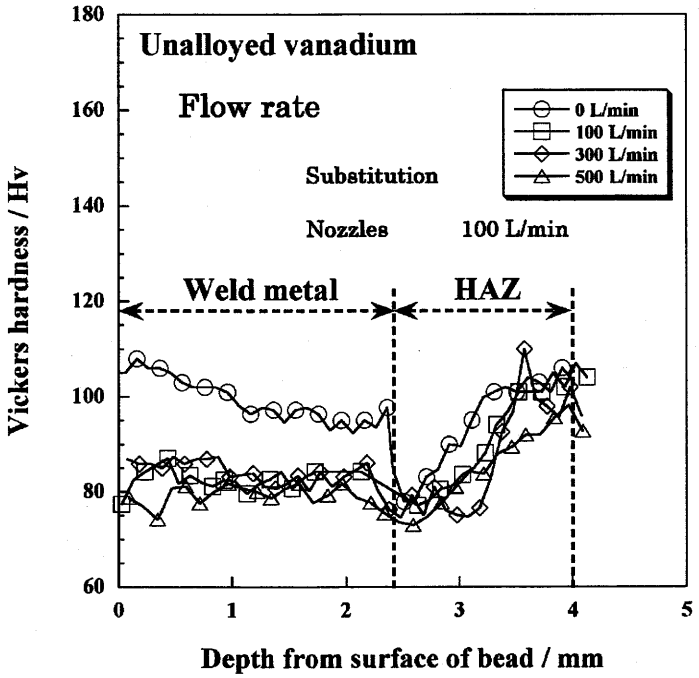

Fig. 3-5 Effect of the flow rate of the substitution gas on depth profile of hardness.

Fig. 3-6 shows the hardness of the specimen as-weld and annealed at 673 K and 1273 K for an hour in a vacuum ($<10^{-6}$ Torr) in the cases with and without the substitution gas supply. The hardness was measured at 1.2 mm thick from the surface of the bead. The hardness of the weld zone was significantly decreased, relative to the hardness of the base metal before annealing regardless of the supply of substitution gas. The decrease in hardness was due to the recovery of the dislocations induced by the cold rolling.

In the both cases with and without the supply of substitution gas, annealing at 673 K did not change hardness. The decrease of hardness in the base metal of the both specimens by annealing at 1273 K is the result of the recovery of the dislocations induced by the cold rolling. The hardening at and near the center of the weldment relative to that of the base metal after annealing at 1273 K is small and large in the cases with and without the substitution gas supply, respectively. In the case with the substitution gas supply, hardening at and near the center of the the weldment was due to the thermal stress introduced during the welding. The reason is that the hardness decreased as low as that of the base metal after annealing at 1273 K. The significant

increase in hardness at and near the center of the weldment in the case without the substitution gas supply seems to be due to contamination.

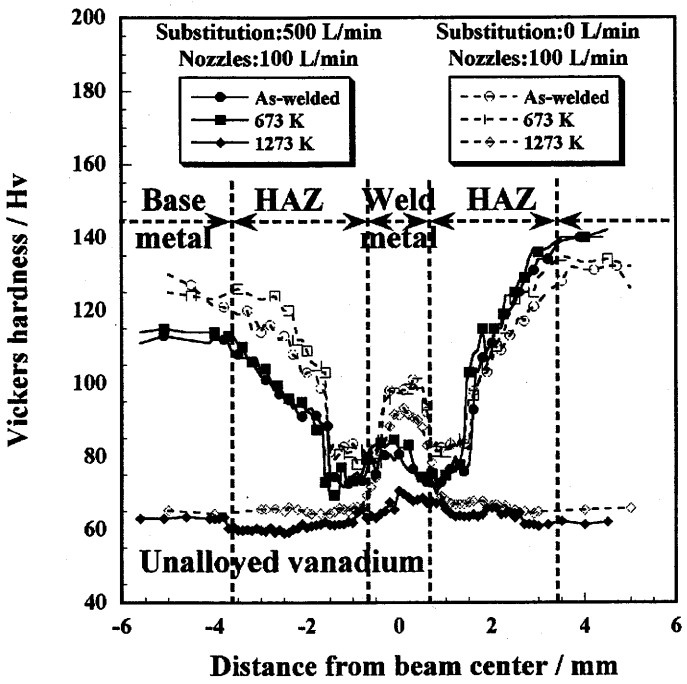

Fig. 3-6 Effect of the post-weld heat treatment on hardness.
Hardness was measured at 1.2 mm in depth position.

Table 3-1 Oxygen and nitrogen levels before and after the laser welding in various flow rate of the substitution gas. (mass ppm)

Flow rate (L/min)		0	100	200	300	500
	Before	After				
O	69	85	76	106	105	82
N	94	170	93	81	92	115

Table 3-1 indicates the result of chemical analysis before and after laser welding. The samples for the analysis were extracted from the molten zones. Without the substitution gas supply, the nitrogen level in the weldment increased significantly. The

reason seems to be that nitrogen was picked up from the air remaining in the environmental control box during the laser welding. The contamination of impurities, such as oxygen or nitrogen, was very small with the flow rate of 100 L/min and above.

ii) Effect of the quartz glass window on hardness

Fig. 3-7 indicates the hardness change with the depth into weld zone from the surface of the bead in the cases with and without the quartz glass window. Hardness was measured at the center of the bead. The laser welding was performed without the quartz glass window on the condition of the flow rate of the substitution gas of 500 L/min. In the case of no-glass, hardness increased remarkably to the depth of about 2.2 mm. In the case without the glass window, sudden drop of hardness was observed similar to the case without the substitution gas supply shown in Fig. 3-5.

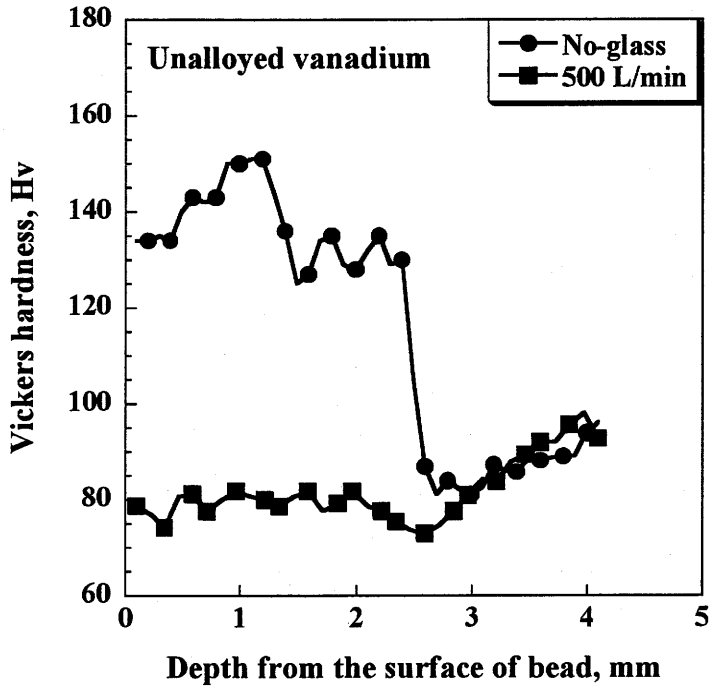

Fig. 3-7 the hardness change with and without the quartz glass window.

Fig. 3-8 shows the hardness of the specimen as-welded and annealed at 1273 K for an hour in a vacuum ($<10^{-6}$ Torr) in the cases with and without the quartz glass window.

The hardness was measured at 1.2 mm thick from the surface of the bead. In the case without the glass window, increase of hardness in the as-welded weld zone was remarkable, and the hardness in the weld zone did not recover by annealing at 1273 K. In the both cases, hardness in the base metal decreased significantly, due to the recovery of the dislocations induced by the cold rolling, as is shown in Fig. 3-6.

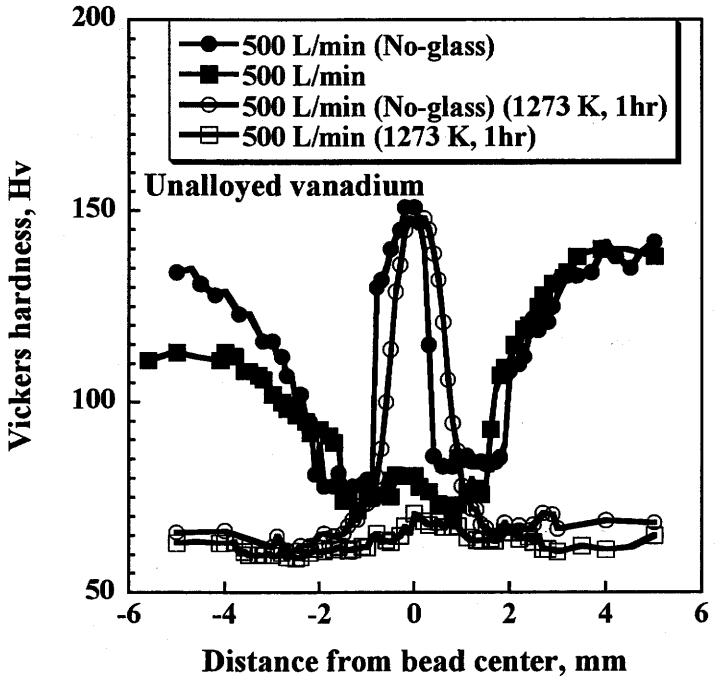

Fig. 3-8 Hardness comparison of the specimen as-welded and annealed at 1273 K.

Hardness increase in the weld zone shown in Fig. 3-7 and 3-8 seems to be due to the contamination with impurities. Increase in hardness due to the contamination without the glass window was larger than any other welding conditions shown in Fig. 3-5. The reason may be that the impurities were continuously supplied into the weld zone from the air during the welding process.

iii) Effect of the flow rate of nozzles on the contaminations

Fig. 3-9 shows the outward appearance of the beads for three welding environments, supplying the argon gas from 100 to 200L/min each with two nozzles without the substitution gas supply. In the case with supply of 100 L/min, the bead was colored due to contamination with impurities. However, Increase in the flow rate of each nozzle to above 150 L/min prevented the bead from coloring due to the contamination.

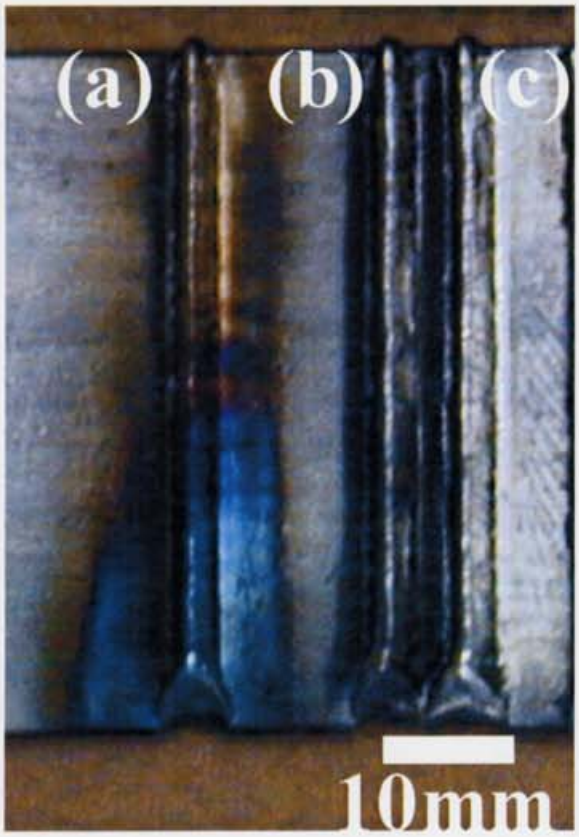

Fig. 3-9 Outward appearance of the beads for three welding environments.

(a) 100 L/min each nozzle

(b) 150 L/min each nozzle

(c) 200 L/min each nozzle

Table 3-2 Impurity level before and after welding on various gas conditions.

Gas conditions		Impurity compositions (mass ppm)		
		C	N	O
Before welding	1	49	125	143
	2	52	132	133
	3	52	121	141
	Average	**51**	**126**	**139**
Each nozzle: 100 L/min	1	39	161	151
	2	42	169	159
Substitution: 0 L/min	3	-	164	150
	Average	**41**	**165**	**153**
Each nozzle: 150 L/min	1	41	124	131
	2	38	133	141
	3	-	140	133
Substitution: 0 L/min	4	-	159	145
	Average	**40**	**139**	**138**
Each nozzle: 200 L/min	1	41	145	137
	2	40	140	144
Substitution: 0 L/min	3	-	143	147
	Average	**41**	**143**	**143**

Table 3-2 indicates the result of chemical analyses of the weld metals welded on the various welding environments. When welded with supplying the gas with the flow rate of 100 L/min for each nozzle and without the substitution gas supply, nitrogen and oxygen level after the welding increased. Increase in the flow rate of each nozzle can prevented the weldment from the contamination with impurities, such as oxygen and nitrogen, as shown in Table 3-2.

3-1-3. Discussions: Estimations on the contamination with impurities during the welding process

It is known that hydrogen may be introduced during welding of vanadium alloys, enhancing the hardness [78-79]. The hardening by hydrogen, however, was shown to recover by annealing at 673 K in vacuum [78-79]. The fact that hardness did not change by annealing at 673 K, as shown in Fig. 3-6, implies that contamination with hydrogen was negligibly small in the present study.

Since the precipitate was not formed in unalloyed vanadium unlike vanadium alloys, the impurities picked up during the laser welding are expected to exist as interstitials in the fusion zone. In the previous study, hardness increase with increasing the impurity levels in unalloyed vanadium and its alloys was quantitatively evaluated [55].

Table 3-3 shows the hardness change, which is the average hardness of the area of the specimen, extracted for the chemical analysis, relative to the hardness of full-annealed base metal (65Hv). The Table 3-2 also shows the predicted hardness change according to the impurity level and the previous hardness measurement of vanadium doped with oxygen and nitrogen [55]. Here ΔHv of 0.06 Hv per 1 mass ppm O and 0.12 Hv per 1 mass ppm N were used for the prediction.

Table 3-3 Hardness change with impurity levels and post-weld heat treatment. The predicted hardness change according to the impurity level and the previous measurements [55] are also listed.

	Each nozzle: 50 L/min Substitution: 500 L/min	Each nozzle: 50 L/min Substitution: 0 L/min
Chemical analysis (mass ppm)	Oxygen: 82 Nitrogen: 115	Oxygen: 85 Nitrogen: 170
Predicted ΔHv according to [55]	3.3	10
ΔHv (as-welded)	12	29
ΔHv (annealed at 673 K)	15	28
ΔHv (annealed at 1273 K)	2	19

As shown in Table 3-3, there is no difference in the hardness between as-welded and annealed at 673 K. This fact indicates that the pick-up of hydrogen in welding process did not occur. Hardness change as-welded and annealed at 673 K is much larger than the predicted values. The hardness increase after welding is due to the introduction of impurities, dislocations and thermal stress during the welding process. Annealing at 1273 K results in the recovery of the dislocations and thermal stress introduced, resulting in the decrease in hardness. The reason is that in pure vanadium, hardness change related to the formation of the precipitates with annealing temperature, as mentioned in chapter 2, does not occur because of the absence of Ti contents.

In the case of supplying the substitution gas, the value of hardness increase is in good agreement with that by the prediction. However, without the substitution gas, measured hardness was higher than predicted. The impurity segregation may be responsible for the excessive hardness.

From the relations between the increase of hardness and the pick-up of the impurities, the present result indicates that the substitution gas supply with the flow rate for the substitution gas of 100 L/min is enough for preventing the contamination during the welding.

3-1-4. Summary

To develop the laser welding technology for vanadium and its alloys without the contamination of impurities, YAG laser welding was carried out with controlling the welding environment.

1. The contamination of impurities during the welding process can be predicted using unalloyed vanadium and with hardness measurements.

2. Simple environmental control box with the nozzles for blowing out the fume and the supply of substitution gas made it possible to obtain the weld zone reducing the contamination of the impurities.

3. By increase in the flow rate of each nozzle or/and the substitution gas, the contaminations with impurities can be reduced.

3-2. Estimation of the mechanical properties of the weldments

3-2-1. Bead appearances with welding parameters

(i) Experimental procedures

High-purity V-4Cr-4Ti alloy (NIFS-HEAT-2) fabricated by the National Institute for Fusion Science was used for the specimen, and prepared by annealing at 1273 K for 2 hours before the welding. Bead-on-plate welds were produced on the 4 mm-thick plate, using 2.0 kW YAG laser. Welding parameters such as average power (1.2-1.8 kW), laser wave mode, traveling speed (0.1-0.7 m/min), etc. were controlled to obtain the optimum welding conditions for 4 mm-thick plate. The laser welding was performed in the condition that the pulse duration and the frequency were 5 millisecond and 100 Hz, respectively. In this case the laser beam was on for 5 milliseconds and then was off for 5 milliseconds.

To characterize the weldment, mechanical properties of the joint, such as tensile, bending and charpy impact properties, were investigated. Bead-on-plate welds were produced on the 4 mm-thick plate under the welding condition of the average power of 1.6 and 1.8 kW, and traveling speed of 0.33 and 0.2 m/min, respectively. The welding condition of 1.6 kW and 1.8 kW was called as the low input and the high input cases, respectively. A tensile specimen of 3-mm-thick slab shape with parallel portion of 10 mm in length and 4 mm in width was machined from the weld zone. Tensile test was carried out at strain rate of 5×10^{-3}/s at room temperature. A bend specimen was 50 mm in length, 8 mm in width and 3 mm in thickness. Charpy impact test was carried out at the range of 77 K to 298K. The specimen had a notch and was 25.4 mm in length and 3.3 mm in both width and thickness. The notch was made at an angle of 30° machined to 0.66 mm in depth, and was machined in the weld metal so that the crack was propagated parallel to the welding direction.

(ii) Full penetration for 4-mm thick V-4Cr-4Ti alloy

Table 3-4 shows the result of chemical analysis before and after the laser welding. The samples were extracted from the base metal and the molten zone, respectively. There was little change in the impurity levels before and after the welding, which indicates that the contamination of the weld metal is small.

Table 3-4 Impurity levels before and after the laser welding. (mass ppm)

	H	C	N	O
Before	29	51	123	139
After	35	49	129	158

Fig. 3-10 indicates the conditions of penetration for 4 mm sheet V-4Cr-4Ti alloy in the various welding conditions. Partial penetration means that the 4 mm full penetration was achieved partially on a bead. Full penetration was possible in some cases of the welding parameters. The wide range of full penetration was acquired with increasing the average power and decreasing the traveling speed. We could not get the full penetration in the condition of average power of 1.2 kW and the traveling speed of 0.1 m/min because the quartz glass was colored.

As shown in Fig. 3-10, the wide range of full penetration was acquired with increasing the average power and decreasing the traveling speed. Even if the traveling speed is very slow, full penetration could not be obtained, when the average power was below 1.4 kW, because of the increase in the energy absorption by the quartz glass. In the present experiment, it is necessary to apply more than 1.4 kW in average power to obtain the full penetration.

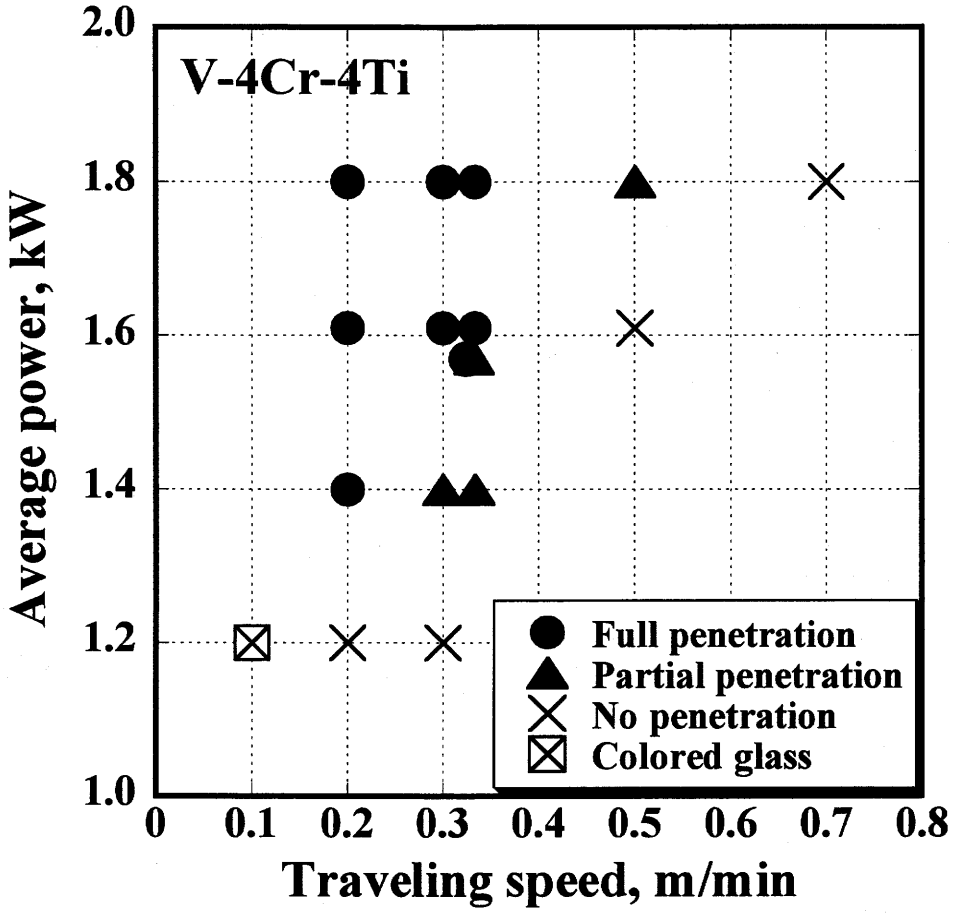

Fig. 3-10 Full penetration for 4 mm sheet V-4Cr-4Ti alloy in the various welding conditions.

Fig. 3-11 indicates the cross sectional microstructure of the weld zone produced on the various welding conditions. The grains in the weld metal were elongated to the center in the middle of specimens and to the upper or the bottom in the outer regions in all specimens. The upper and lower parts of the weld metal and the HAZ became wide when increasing the average power from 1.4 to 1.8 kW at the same traveling speed of 0.2 m/min. (a, b and c) and when decreasing the traveling speed from 0.33 to 0.2 m/min at the same average power of 1.6 kW. (b, d and e) The grain growth in the center of region (1) was more remarkable than that of any other area.

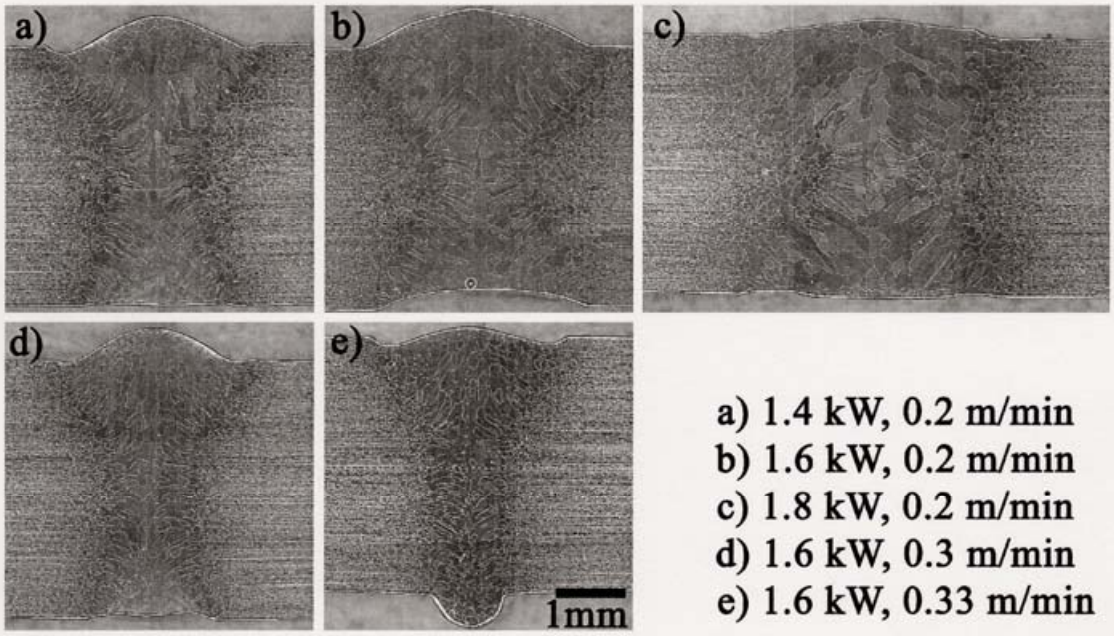

Fig. 3-11 Dependence of the cross sectional microstructure with welding conditions.

As shown in Fig. 3-11, the grain growth and the extension of HAZ were accelerated with increasing the introduced energy during the welding. Increase of the power at the same traveling speed made the top and the bottom of the weld zone wide. The reason must be that the energy remaining after full penetration was consumed for extending the weld zone, because the heat removal is slower through the surface than through the base metal.

Fig. 3-12 shows the positional difference of microstructure and hardness. Hardening occurred in the weld metal and the HAZ. The epitaxial grain growth in the weld metal was observed. The weld metal solidified into a columnar grain structure, and the grain size was much larger than any other place. The banded-structure precipitates, which were observed in the base metal before welding, were dissolved in the weld metal and in the inner region of the HAZ. Thus, the HAZ is divided into two regions; region (1) and (2). Region (1) in the HAZ was designated from the weld line to the boundary of the resolution of the banded-structure precipitates. Region (2) ranged from the boundary of the resolution of the banded-structure precipitates to that of the hardening. Grain growth was observed in the

weld metal and in region (1), and the grain size in region (1) changed with the distance from the weld metal. In region (2), there was no difference in grain size and the banded-structure precipitates from those in the base metal.

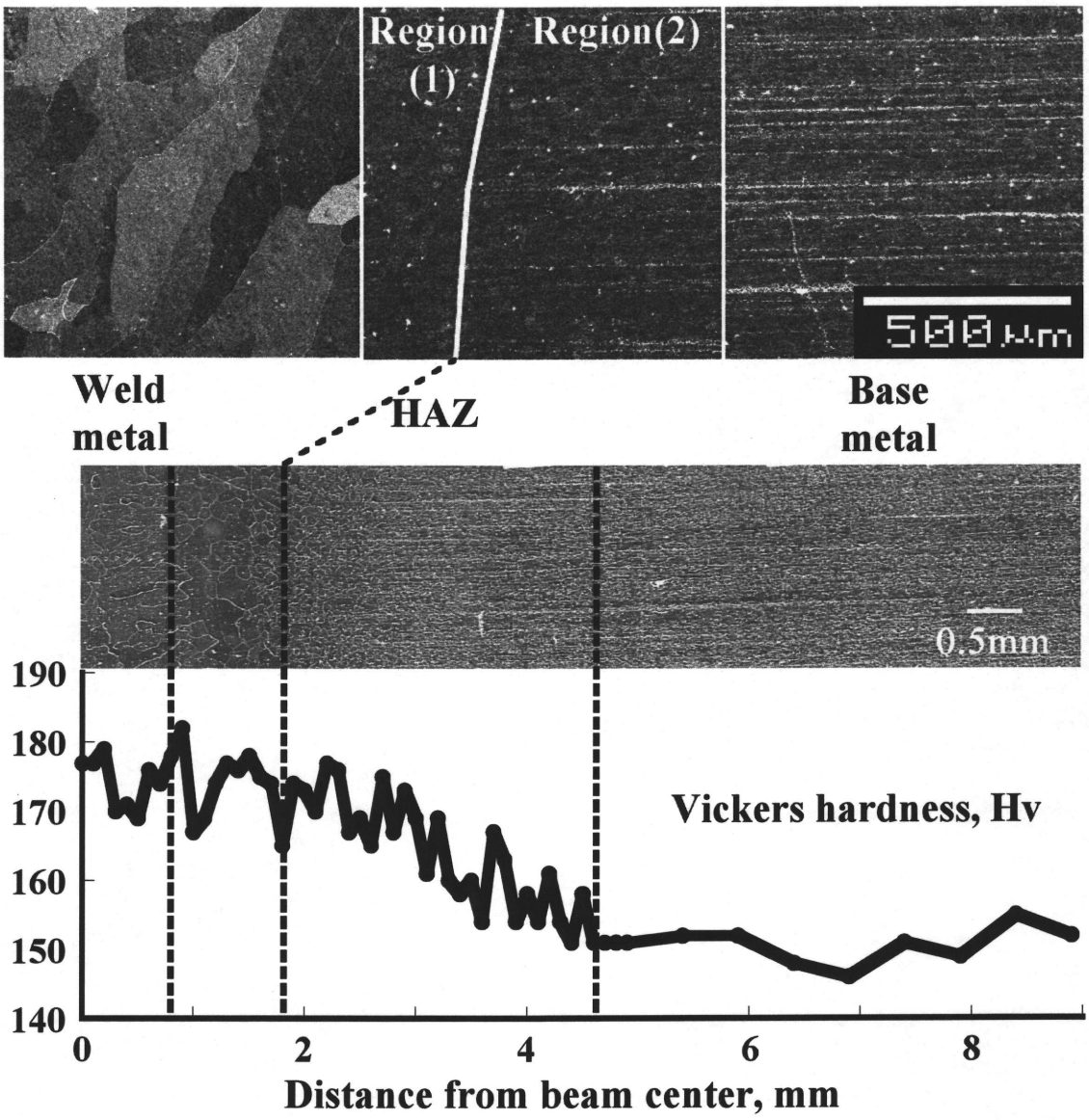

Fig. 3-12 Positional difference of microstructure and hardness.

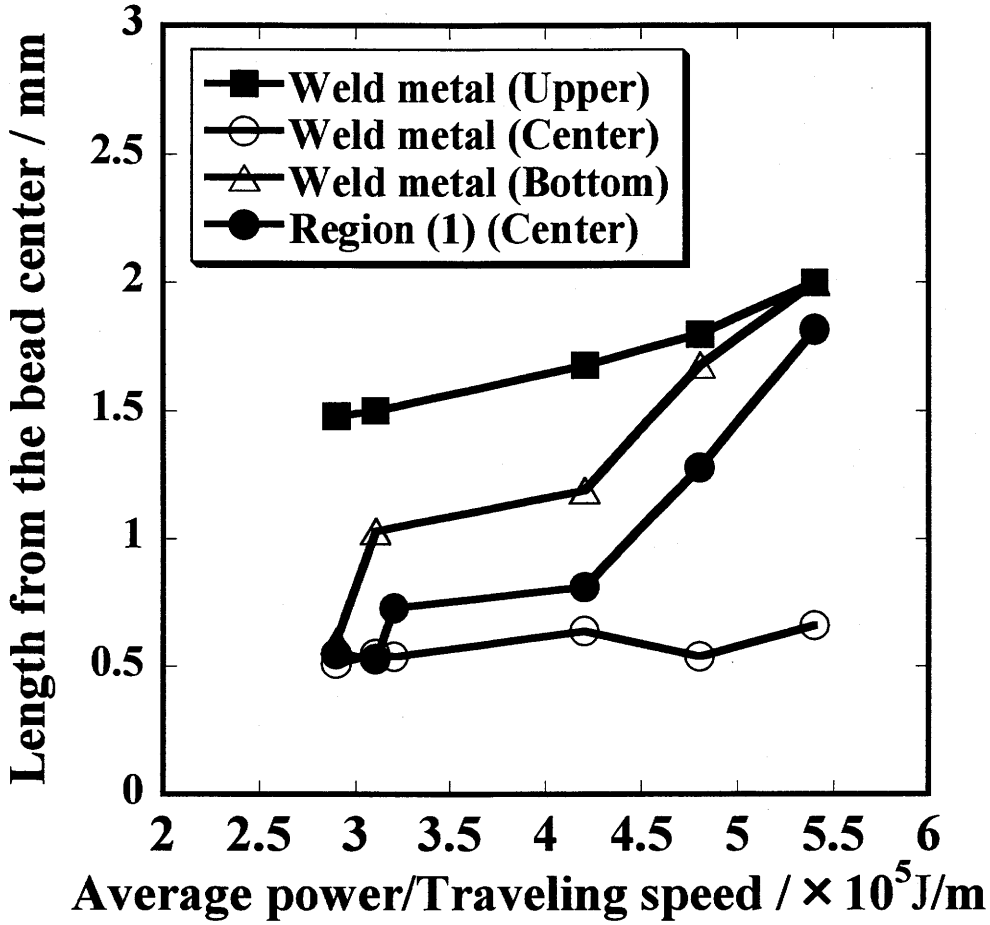

Fig. 3-13 Relations between the width of weld metal and Region (1), and the input energy.

Fig. 3-13 shows the width of weld metal and HAZ region (1) with the introduced energy (average power / traveling speed). The width of weld metal was measured on the three points, the upper, the middle and the bottom of the plate cross section. The width of region (1) was measured only at the center of the cross section, because the grain growth was most remarkable at the center. The width of weld metal in the upper and the bottom increased with increasing the introduced energy. Especially, the change of width in the bottom was significant. There was little difference in the width of weld metal in the middle, as shown in Fig. 3-11. The width of region (1) increased remarkably with increasing the input energy.

3-2-2 Impurity behavior in the weld zone

Microstructure and hardness change in the cases of the low and high input power are shown in Fig. 3-14: the welding condition of the average power of 1.6 and 1.8 kW, and traveling speed of 0.33 and 0.2 m/min, respectively. The width in the weld metal and the heat-affected zone (HAZ) increased with the increase in the input power.

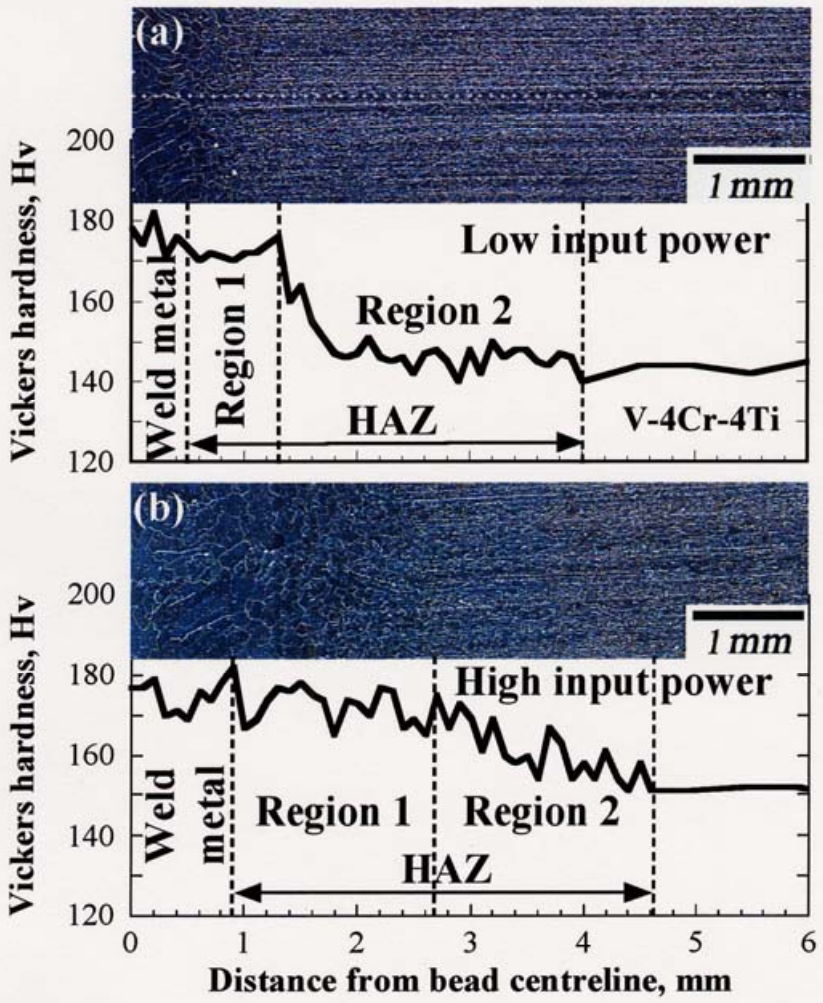

Fig. 3-14 Microstructure and hardness change with welding conditions.

(a) low input power (average power of 1.6 kW and traveling speed of 0.33)

(b) high input power (average power of1.8 kW and traveling speed of 0.2 m/min)

from the bead center in the case of the low input power. Hardness of the base metal was about 140 Hv. On the other hand, the grain growth occurred significantly in the Region (1) and hardness decreased gradually over the wide range in the case of the high input power.

Fig. 3-15 shows microstructural development with a distance from the center of weld metal, in the case of the low input power. Two kinds of precipitates, large and small ones, were observed in the base metal before welding. There were no precipitates in the weld metal and at 1 mm from the center of the weld metal, where the grain growth occurred, and, instead, dislocations introduced by the heat stress during the cooling were observed. The large precipitates were observed in 1.8 mm from the center of weld metal, where the small precipitates were not observed, however. Both kinds of precipitates were observed at 4.4 mm, as is the case for the base metal before the welding.

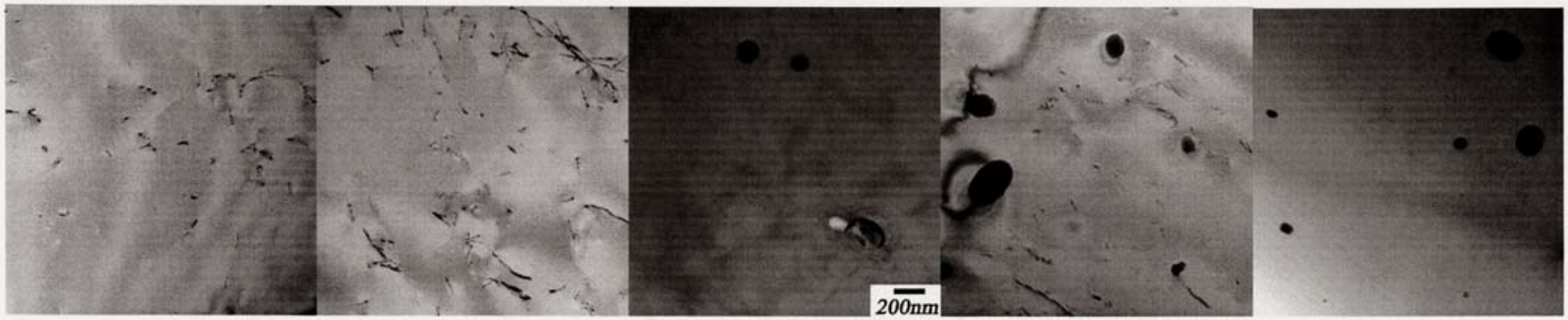

Fig. 2 Microstructural development of the weld metal with a distance from the bead centerline in the case of the low power density.

(a) weld metal (b) 1 mm (c) 1.8 mm (d) 4.4 mm (e) base metal

3-2-3 Effect of the input power on the mechanical properties of the weld metal

Fig. 3-16 shows the outwards and the surface of the weld zone observed after the bending test. There were many wrinkles introduced in the weld metal during the bending, but in either case of the welding conditions, no crack was detected in the weld zone after the bending test.

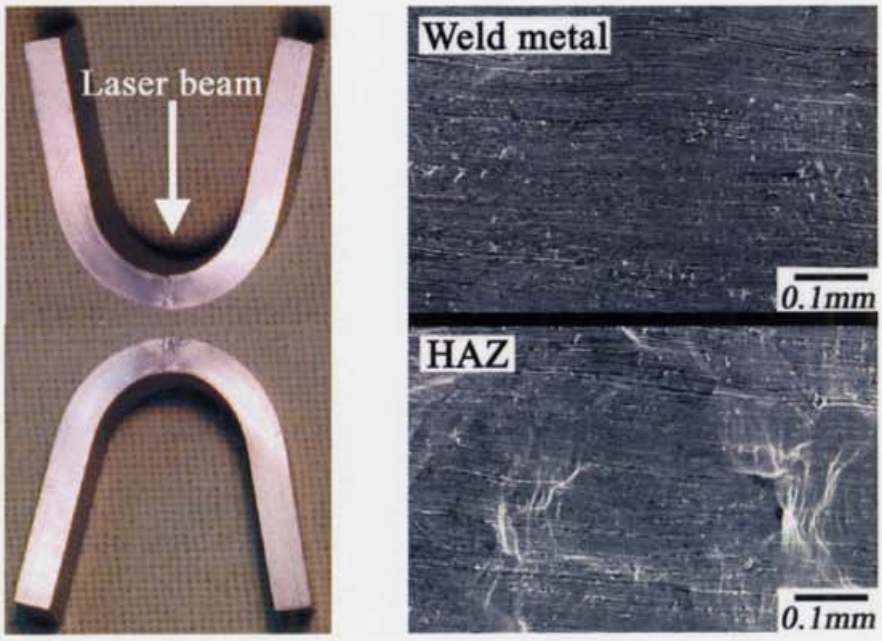

Fig. 3-16 Outwards and the surface of the weld zone after the bend test in the low input power.

Fig. 3-17 shows the load-displacement curves for the base metal and the weldment, and the appearance of the specimens after the tensile test. In the both cases of input power, the specimens were fractured in the base metal during the tensile test. The tensile strength of the weldment for the low input power (418 MPa) was slightly higher than that of the base metal (402 MPa). The total elongation of the weldment (40.3%) was, on the other hand,

slightly smaller than that of the base metal (49.3%). Fractography revealed that the specimen fractured with ductility.

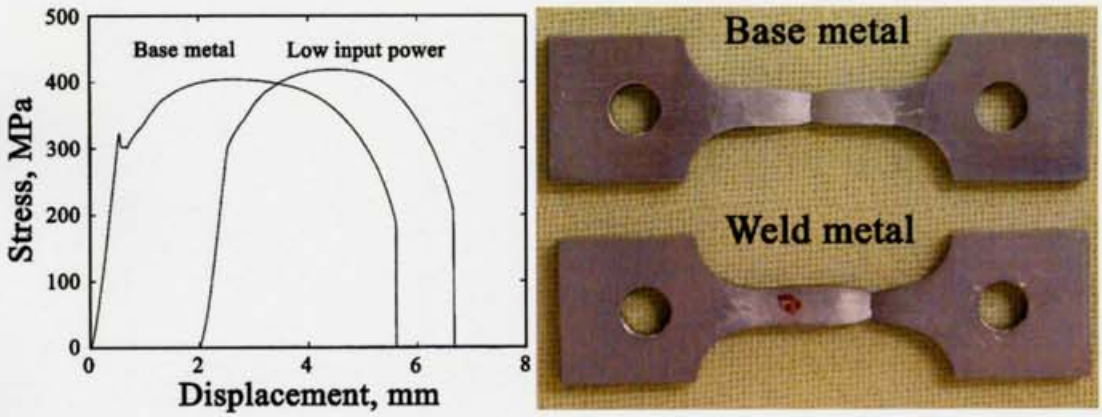

Fig. 3-17 load-displacement curves for the base metal and the weldment, and the specimen appearance

The change of the absorption energy of the weld metal as a function of the test temperature was shown in Fig. 3-18. In the case of the high input power, absorption energy of the weld metal was significantly lower than that of the base metal at all test temperatures. However, in the case of the low input power, the absorption energy of the weld metal was as high as that of the base metal.

Fig. 3-19 shows the fractographic photographs for charpy specimens tested at 77 K and 221 K. In the case of the high input power, brittle fracture under the notch nucleated and propagated with little plastic deformation at 77 K. On the other hand, in the case of low input power and the test temperature at 77 K, some ductile fracture was found under the notch, and the fracture mode turned to a brittle fracture. In the case of the test temperature at 221 K, the fracture mode was mostly a plastic deformation and a ductile fracture. In the both cases, all brittle fracture was intergranular. In all specimens, the fracture mode turned from the brittle fracture to the ductile fracture, with the crack propagation.

fracture mode turned from the brittle fracture to the ductile fracture, with the crack propagation.

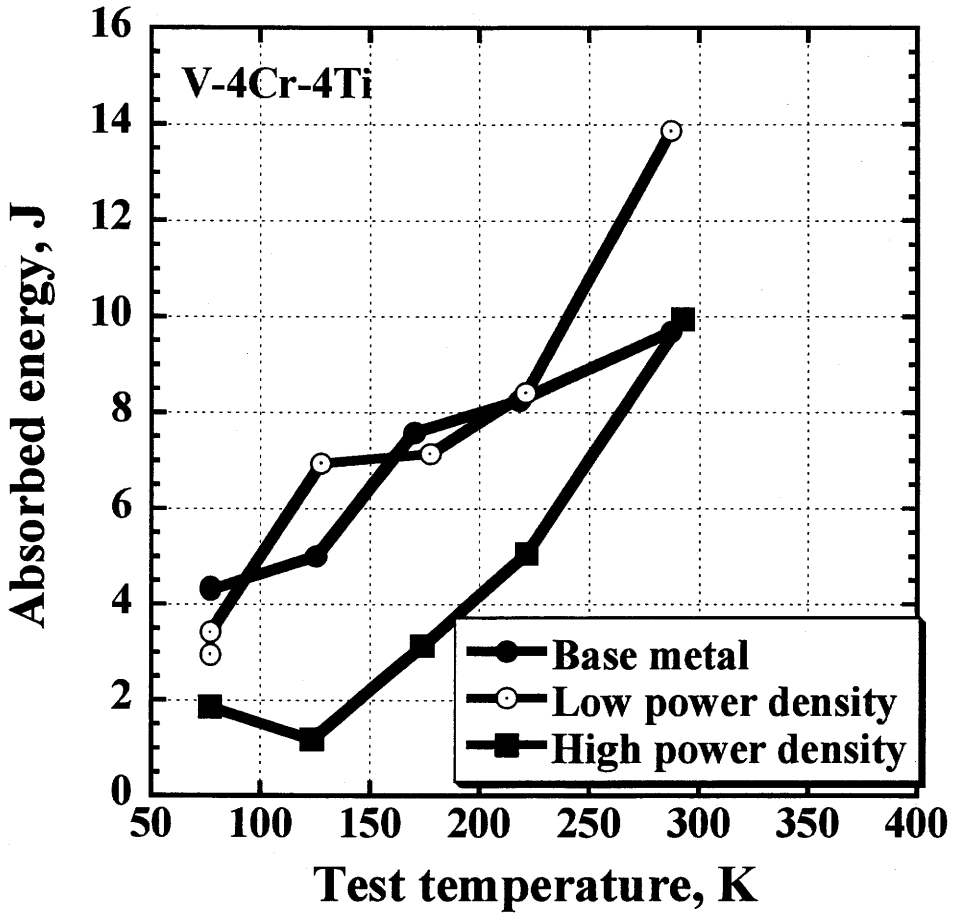

Fig. 3-18 Change the absorption energy as a function of test temperature.

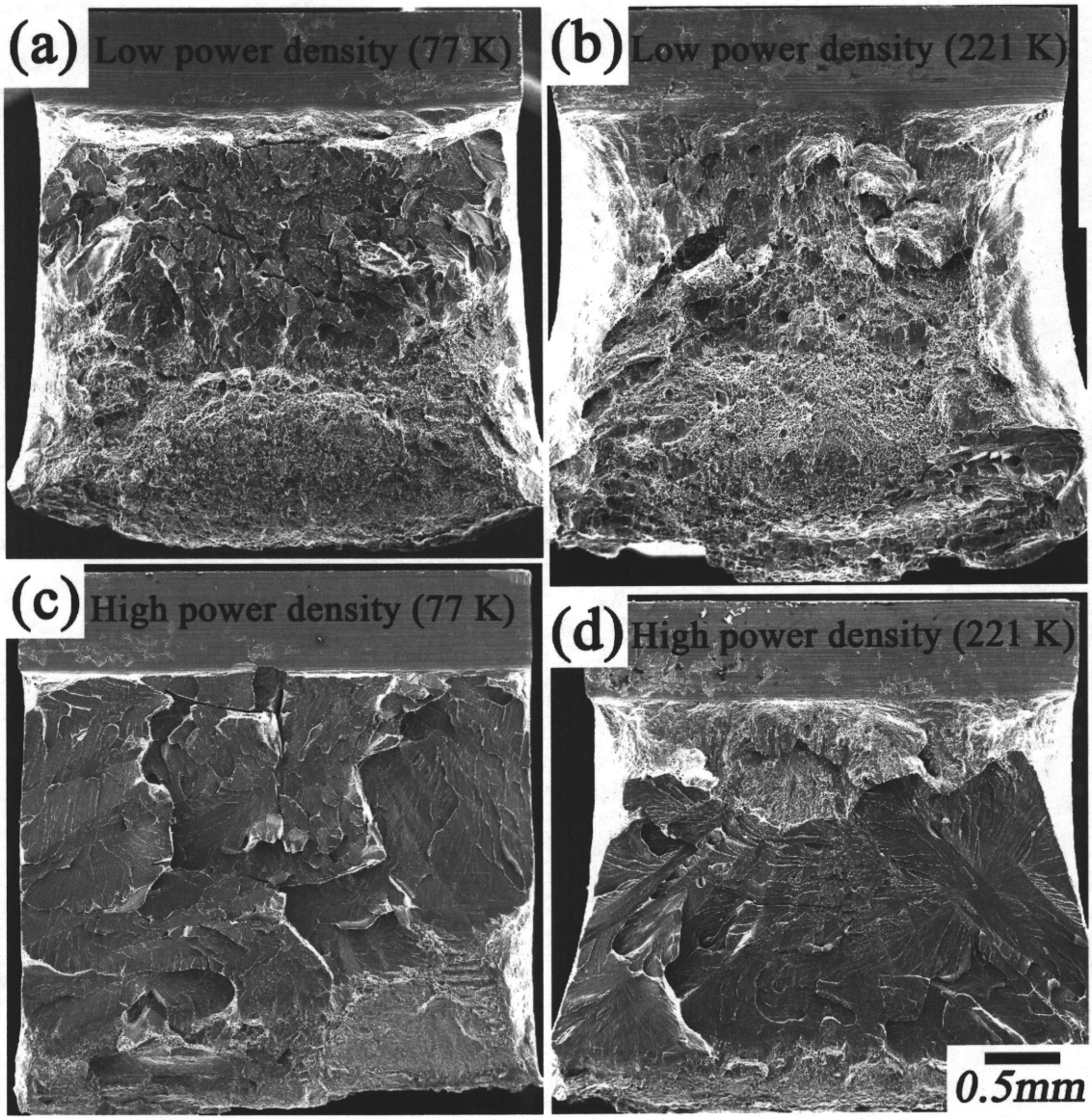

Fig. 3-19 Fractographic photographs for charpy specimens tested at 77 K and 221 K.

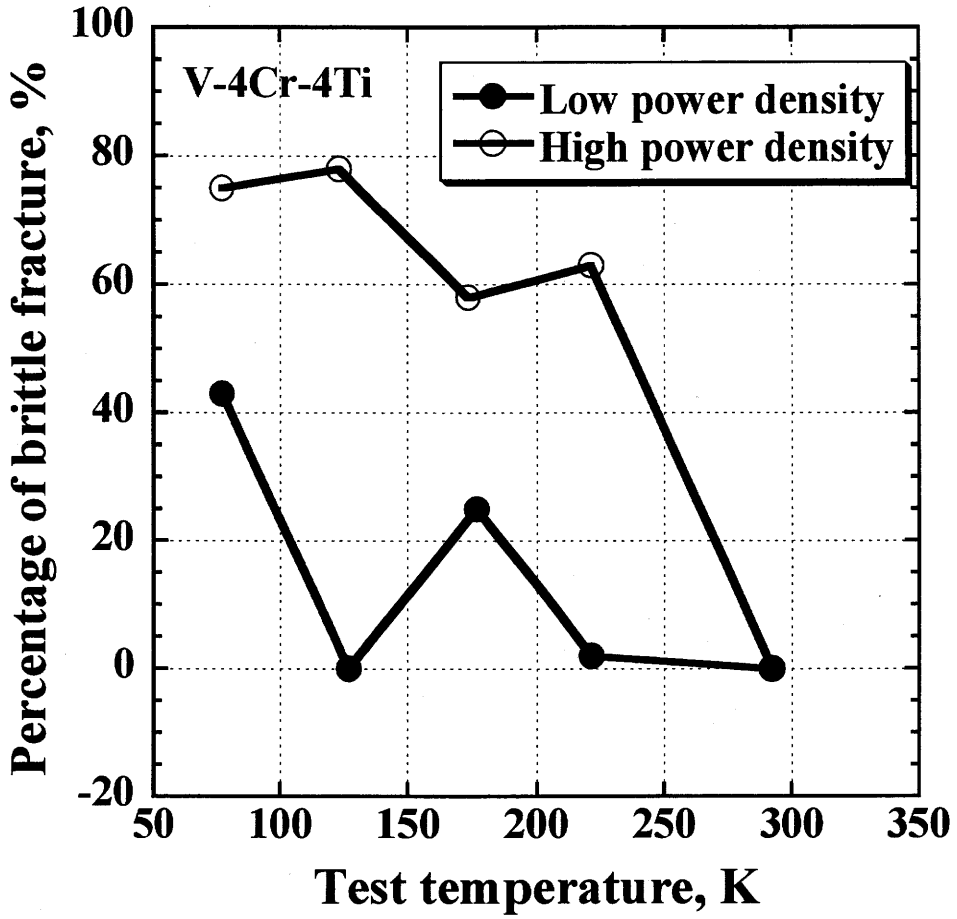

Fig. 3-20 Change in percentage of brittle fracture with the test temperature.

Fig. 3-20 shows percentage of brittle fracture with the test temperature. The both specimens fractured in ductile manners at room temperature. However, in both specimens, percentage of the brittle fracture had a tendency to increase with the decrease in the test temperature. Especially, in the case of the high input power, percentage of brittle fracture increased drastically at 221 K. In the case of the low input power, the specimen tested at 127 K fractured totally in a ductile manner.

3-2-4 Discussions

The hardness of the weld metal and the HAZ, shown in Fig. 3-14, is thought to relate with the impurity behavior. It is well known that, in unalloyed vanadium and its

alloys, increase in the impurity level results in increase in hardness [55]. Since there is small contamination by impurities such as hydrogen, oxygen, nitrogen, as shown in Table 3-4, the hardening is attributed to the state and distribution of the impurities. As shown in Fig. 3-14 (a) and 3-15, no precipitate was observed in the weld metal and the Region (1), where hardness increased significantly. Large and small precipitates were observed in the base metal before welding, as shown in Fig. 3-15. The large precipitates were identified as Titanium-rich, including the impurities of N, O and C, and the small ones were Titanium-Oxygen-Carbon compounds in chapter 2. In the previous study, the annealing at above 1373 K was shown to result in hardening, which was induced by the dissolution of the precipitates, as mentioned in Chapter 2. Thus, it seems that the dissolution of both the large and the small precipitates into the vanadium alloy during the welding process resulted in the hardening of the weld metal and the Region (1).

In pure vanadium, increase in nitrogen and oxygen by 1 mass ppm resulted in increase in hardness by about 0.12 and 0.06 Hv, respectively [55]. According to the chemical composition shown in Table 3-4, nitrogen and oxygen level in the weld metal, where no precipitates were observed, is estimated to be 129 and 158 mass ppm, respectively. Converting these impurity levels to the hardness, the hardness is estimated to increase by about 25 Hv. In the region of 2 to 4 mm from the centerline of weld metal (Region (2)), only small precipitates disappeared. In the previous study, the dissolution of these small precipitates resulted in hardness increase by about 10 Hv. These estimates are in good agreement with the results of the present experiments. Hence, hardness increase in the weld metal and the HAZ can be explained quantitatively by the dissolution of the precipitates.

From the fact that there was no crack in the weld zone after the bending test, as shown in Fig. 3-16, it is demonstrated that the weld zone has a good ductility. In the tensile test, the specimen fractured in the base metal, as shown in Fig. 3-17. This shows that there was no softening in the weld zone by the welding. From the results of bending and tensile test, soundness and good ductility of the weld zone are confirmed.

The width of the weld metal and the HAZ, and the grain size increased with the increase in the introduced input power, as shown in Fig. 3-14. The reason may be that the cooling rate of the weld zone became low with the increase in the input power.

Absorption energy of the weld metal decreased with the increase in the input power, as shown in Fig. 3-18. As shown in Fig. 3-19, the nucleated crack seems to propagate easily through the large grains, resulting in the wide brittle fracture region in the case of the high input power. (Fig. 3-20) From the results of tensile test, elongation of the weld zone was smaller than that of the base metal. Thus, to obtain the high absorption energy, it will be effective to make the width of weld zone narrow. It is recommended to reduce the low input power in condition that the full penetration of the weld zone is achieved.

3-2-5 Summary

The microstructural development and the impurity behavior in the weld zone, and the effect of the welding condition on the hardness and the properties of bending, tensile and charpy impact were investigated for the laser weld joints of V-4Cr -4Ti alloys.

1. It was made possible to obtain the weldments reducing the contamination with the impurities during the welding, with a simple environmental control box having nozzles for blowing out the fume and supplying the substitution gas.

2. Increase in hardness of the weld zone is due to the dissolution of large and small precipitates. In the weld metal, dissolution of both large and small precipitates resulted in remarkable hardening. Only small precipitates disappeared at a distance from the weld metal, resulting in the small hardening. The hardening was quantitatively explained by the previous experiments on the impurity effects in the pure vanadium and V-4Cr -4Ti alloys.

3. Soundness of the weld joint was confirmed by estimating mechanical properties. In the tensile test of the joint, decrease in tensile strength did not occur but total elongation decreased slightly in the weld zone.

4. The absorption energy of the weld metal produced by the low input power was as high as that of the base metal. Decrease in the absorption energy in the case of the high input power seems to be due to the increased width of the weld metal and the HAZ and the increased grain size in the weld zone. To improve the absorption energy of the weld metal, it is effective to decrease the input power for reducing the grain size and the width of the weld metal and the HAZ.

CHAPTER 4

Conclusions

The purpose of this study is to establish a high-grade welding technology for V-4Cr-4Ti alloys. For this purpose, the effect of the welding conditions on the mechanical properties of the weldment was investigated. Also investigated was the impurity behavior in the weld zone by microstructural observation for the mechanistic understanding of the property change. As a basic study supporting the mechanistic understanding, hardness and precipitation behavior by heat treatment was also carried out for V-4Cr-4Ti.

4-1. Impurity behavior

1. The effect of the oxygen and nitrogen on the hardness and the precipitation behavior was clarified independently by heat treatment at various temperatures after solid solution treatment at 1373 K.

2. Impurities exist in both the solid solution and the precipitates. Two kinds of precipitates were observed: large and small precipitates. They were identified as Ti-rich and Ti-C-O, respectively.

3. Some fraction of oxygen and carbon was in the small precipitates. These precipitates were formed at 973 to 1273 K. The hardening at above 1373 K is attributed to the increase in the impurity levels in the matrix induced by the re-solution of the precipitates, and the formation of V-C precipitates on grain boundaries. On the other hand, nitrogen exists mostly in the large precipitates, which is stable up to 1373 K. The large precipitates were dissolved by annealing at 1573 K, resulting in the formation of V (CNO) on grain boundaries and in further hardening.

4. Thermomechanical and annealing temperature will be optimized at 1273 K or below, according to the balance between the precipitation hardening and the solid solution hardening. Heat treatment at above 1273 K will result in the degradation of the properties.

4-2 Development of the high-grade laser welding technology

1. It was made possible to obtain the weldments reducing the contamination with the impurities during the welding, with a simple environmental control box having nozzles for blowing out the fume and supplying the substitution gas.

2. Increase in hardness of the weld zone is due to the dissolution of large and small precipitates. In the weld metal, dissolution of both large and small precipitates resulted in remarkable hardening. Only small precipitates disappeared at a distance from the weld metal, resulting in the small hardening. The hardening was quantitatively explained by results of the study on the impurity behavior.

3. Soundness of the weld joint was confirmed by estimating mechanical properties. In the tensile test of the joint, decrease in tensile strength did not occur but the total elongation decreased slightly in the weld zone.

4. The absorption energy of the weld metal produced by the low input power was as high as that of the base metal. Decrease in the absorption energy in the case of the high input power seems to be due to the increased width of the weld metal and the HAZ, and the increased grain size in the weld zone. To improve the absorption energy of the weld metal, it is effective to decrease the input power for reducing the grain size and the width of the weld metal and the HAZ.

References

[1] K. Tokimatsu, J. Fujino, Y. Asaoka, Y. Ogawa, K. Okano, T. Yoshida, R. Hiwatari, S. Konishi, S. Nishio, K. Yamaji, Y. Kaya, IAEA-CN-77/SEP/03, in proc. of 18th IAEA Fusion energy Conference, Sorrento, Italy, 2000.

[2] K. Yamaji, J. Fujino, K. Osada, Environmental Economics and Policy Studies, 3 (2), 159-171.

[3]「2002 年度　エネルギーと環境　―子孫にツケを回さない経済社会を目指して―」、産業技術会議　(2002)

[4] K. Tokimatsu, J. Fujino, S. Konishi, Y. Ogawa, K. Yamaji, Energy Policy, in press.

[5] Proccding of ITER Materials Assessment Meeting, Garching, Germany, 1997.

[6] M. Seki, R. Matera, F. Tavassoli, J. Davis, D. Smith, J. Nucl. Mater., 271-272 (1999) 569.

[7] Report of the 4th IEA Working Group Meeting on SiC/SiC for Fusion Applications, Frascati, Italy, 2000.

[8] Report of the 5th IEA Workshop on Vanadium Alloys for Fusion Applications, Tokyo, Japan, 2000.

[9] G. Aiello, L Giancarli, H. Golfier, J.-F. Maire, Fus. Eng. Design, in press.

[10] S.J. Zinkle, N.M. Ghoniem, Fus. Eng. Design, 51-52 (2000) 55-71.

[11] A.–A.F. Tavassoli, J. Nucl. Mater., 302 (2002) 73-88.

[12] D.L. Smith, S. Majumdar, M. Billone, R. Mattas, J. Nucl. Mater., 283-287 (2000) 716-720.

[13]「核融合実用炉を目指した材料開発の現状」、National Institute for Fusion Science, (1993), 6.

[14] M.I. Solonin, J. Nucl. Mater., 258-263 (1998) 30-46.

[15] E.E. Bloom, J. Nucl. Mater., 258-263 (1998) 7-17.

[16] D.L. Smith, M.C. Billone, S. Majumdar, R.F. Mattas and D.-K. Sze, J. Nucl. Mater., 258-263 (1998) 65-73.

[17] 日米科学技術協力・JUPTER 計画成果報告書、National Institute for Fusion Science, (2000), 50.

[18] A. Hishinuma, A. Koyama, R.L. Klueh, D.S. Gelles, W. Dietz, K. Ehrlich, J. Nucl. Mater., 258-263 (1998) 193-204.

[19] R.L. Klueh, D.J. Alexander, J. Nucl. Mater., 218 (1995) 151-160.

[20] G.R. Odette, G.E. Lucas, J. Nucl. Mater., 117 (1983) 264-275.

[21] B.L. Cox, F.W. Wiffen, J. Nucl. Mater., 85-86 (1973) 901-905.

[22] D. R. Diercks, B. A. Loomis, J. Nucl. Mater., 141-143 (1986) 1117-1124.

[23] H. M. Chung, B. A. Loomis, D. L. Smith, J. Nucl. Mater., 239 (1996) 139-156.

[24] M. L. Grossbeck, J. F. King, D. J. Alexander, P. M. Rice, G. M. Goodwin, J. Nucl. Mater., 258-263 (1998) 1369-1374.

[25] S.J. Zinkle, N.M. Ghoniem, Fus. Eng. Design, 51-52 (2000) 55-71.

[26] Karl Ehrlich, E.E. Bloom, T. Kondo, J. Nucl. Mater., 283-287 (2000) 79-88.

[27] K. Shiba, A. Hishinuma, A. Kohyama, K. Masamura, Japan Atomic Energy Research Institute- Tech., 97-038, 1997.

[28] A. Kohyama, Y. Kohno, K. Asakura, H. Kayano, J. Nucl. Mater., 212-215 (1994) 684-.

[29] K. Ehrlich, S. Kelzenberg, H.-D. Rohrig, L. Schafer, M. Schirra, J. Nucl. Mate., 212-215 (1994) 678-.

[30] P.J. Maziasz, J. Nucl. Mater., ICFRM9

[31] S. Ukai, M.Fujiwara, J. Nucl. Mater., 307-311 (2002) 749-757

[32] R. Lindau, A. Moeslang, M. Shira, P. Schlossmacher,

[33] B.A. Loomis, H.M. Chung, L.J. Nowicki, D.L. Smith, J. Nucl. Mater., 212-215 (1994) 799-803.

[34] H. Matsui, K. Fukumoto, D.L. Smith, H.M. Chung, W. van Witzenburg, J. Nucl. Mater., 233-237 (1996) 92-99.

[35] R.J. Kurtz, K. Abe, V.M. Chernov, V.A. Kazakov, G.E. Lucas, H. Matsui, T. Muroga, G.R. Odette, D.L. Smith, S.J. Zinkle, J. Nucl. Mater., 283-287 (2000) 70-78.

[36] S.J. Zinkle, H. Matsui, D.L. Smith, A.F. Rowcliffe, E. van Osch, K. Abe, V.A. Kazakov, J. Nucl. Mater., 258-263 (1998) 205-214.

[37] D.k. SZe, Fus. Technol., 21 (1992) 2099-

[38] S. Malang, H.U. Borgstedt, E.H. Farnum, K. Natesan, I.V. Vitkovski, Fus. Eng. Design, 27 (1995) 570-586.

[39] R.H. Jones, C.H. Henager, Jr. and G.W. Hollenberg, J. Nucl. Mater., 191-194 (1992) 75-.

[40] S. Sharafat, R.H. Jones, A. Kohyama, P. Fenici, Fus. Eng. Design, 29 (1995) 411-420.

[41] H.M. Chung, B.A. Loomis, D.L. Smith, Fus. Eng. Design, 29 (1995) 455-464.

[42] B.A. Loomis, L.J. Nowicki, D.L. Smith, J. Nucl. Mater., 212-215 (1994). ICFRM6

[43] H.M. Chung, B.A. Loomis, D.L. Smith, J. Nucl. Mater., 212-215 (1994). ICFRM6

[44] M. Satou, K. Abe, H. Kayano, J. Nucl. Mater., 179-181 (1991) 757-.

[45] M. Satou, K. Abe, H. Matsui, J. Nucl. Mater., 191-194 (1992) 938-.

[46] T. Shibayama, I. Yamagata, H. Kayano, C. Namba, J. Nucl. Mater., 258-263 (1998) 1361-1868.

[47] M. Satou, T. Chuto, K. Abe, J. Nucl. Mater., 283-287 (2000) 367-371.

[48] M. Fujiwara, M. Satou, A. Hasegawa, K. Abe, J. Nucl. Mater., 283-287 (2000) 1311-1315.

[49] T. Muroga, T. Nagasaka, A. Kawabata, S. Sakurai, M. Sagara, J. Nucl. Mater. 283-287 (2000) 711.

[50] T. Nagasaka, T. Muroga, M. Imamura, S. Tomiyama, M. Sakata, Fusion Technology 39 (2001) 659-663.

[51] T. Muroga, T. Nagasaka, M. Imamura, in: Fusion Energy 2000, 18th Conference Proceeding, Sorrento, October 2000, FTP1/09.

[52] H. M. Chung, H. C. Tsai, D. L. Smith, R. Peterson, C. Curtis, C. Wojcik, R. Kinney, Fusion Materials Semiannual Progress Report for period, DOE/ER-0313/17, 1994, 178.

[53] W. R. Johnson and J. P. Smith, J. Nucl. Mater. 258-263 (1998) 1425-1430.

[54] M.M. Potapenko et al., in: Report of the 5th IEA Workshop on Vanadium Alloys for Fusion Applications, Tokyo, Japan, 2000, p. 142.

[55] T. Nagasaka, H. Takahashi, T. Muroga, T. Tanabe, H. Matsui, J. Nucl. Mater., 283-287 (2000) 816-821.

[56] T. Nagasaka, M.L. Grossbeck, T. Muroga, J.F. King, Fus. Technol., 39 (2001) 664-668.

[57] Y. Wu, T. Muroga, Q. Huang, Y. Chen, T. Nagasaka, A. Sagara, J. Nucl. Mater., 307-311 (2002) 1026-1030.

[58] B.A. Loomis, L.J. Nowicki, D.L. Smith, Fusion Reactor Materials, Semiannual Progress Report, DOE/ER-0313/17, 1994, 187-193.

[59] B.A. Loomis, R.H. Lee, D.L. Smith, J.R. Peterson, J. Nucl. Mater., 155-157 (1988) 631.

[60] J. Gazda, B.A. Loomis, L.J. Nowicki, D.L. Smith, S. Danyluk, Fusion Reactor Materials, Semiannual Progress Report, DOE/ER-0313/15, 1993, 232-239.

[61] A.N. Gubbi, A.F. Rowcliffe, W.S Eatherly, Fusion Reactor Materials, Semiannual Progress Report, DOE/ER-0313/18, 1995, 187-201.

[62] D.T. Hoelzer, M.K. West, S.J. Zinkle, A.F. Rowcliffe, J. Nucl. Mater., 283-287 (2000) 616-621.

[63] Huaxin Li, M.L. Hamilton, R.H. Jones, Fusion Reactor Materials, Semiannual Progress Report, DOE/ER-0313/18, 1995, 215-235.

[64] H.M. Chung, J. Gazda, L.J. Nowicki, J.E. Sanecki, D.L. Smith, Fusion Reactor Materials, Semiannual Progress Report, DOE/ER-0313/15, 1993, 207-218.

[65] K. Fukumoto, T. Morimura, T. Tanaka, A. Kimura, K. Abe, H. Takahashi, H. Matsui, J. Nucl. Mater., 239 (1996) 170-175.

[66] K. Natesan, C.B. Reed, Z. Xu, D.L. Smith, Fusion Materials Semiannual Progress Report, DOE/ER-0313/25 (1998) 64-68.

[67] Z. Xu, C.B. Reed, K. Natesan and D.L. Smith, Fusion Materials Semiannual Progress Report, DOE/ER-0313/26 (1999) 49-53.

[68] Y. Yan, D.L. Smith, Z. Xu, H. Tsai, T. Nagasaka and T. Muroga, Fusion Materials Semiannual Progress Report, DOE/ER-0313/29 (2000) 41-44.

[69] H.M. Chung, J.-H. Park, R.V. Strain, K.H. Leong, D.L. Smith, J. Nucl. Mater., 258-263 (1998) 1451-1457.

[70] J.P. Smith, W.R. Johnson, P.W. Trester, J. Nucl. Mater., 258-263 (1998) 1420-1424.

[71] Y.X. Gan, H.A. Aglan, R.V. Steward, B.A. Chin, M.L. Grossbeck, J. Nucl. Mater., 299 (1998) 157-164.

[72] M.L. Grossbeck, J.F. King, T. Nagasaka, S.A. David, J. Nucl. Mater., 307-311 (2002) 1590-1594.

[73] J.R. DiStefano, J.H. DeVan, D.H. Röhrig, L.D. Chitwood, J. Nucl. Mater., 273 (1999) 102-110.

[74] J.R. DiStefano, J.H. DeVan, J. Nucl. Mater., 249 (1997) 150-158.

[75] Y. Yan, H. Tsai, A.D. Storey, D.L. Smith and Z. Xu, Fusion Materials Semiannual Progress Report, DOE/ER-0313/28 (2000) 17-23.

[76] T. Nagasaka, N. J. Heo, T. Muroga, M. Imamura, presented at the 6th Int. Symp. on Fusion Nuclear Technology, San Diego, 2002.

[77] Y. Yan, H. Tsai, D. L. Smith, Fusion Materials Semiannual Progress Report, DOE/ER-0313/27 (1999) 23-31.

[78] M.L Grossbeck, J.F. King, Fusion Materials Semiannual Progress Report,

DOE/ER-0313/26 (1999) 44-48.

[79] T. Nagasaka, T. Muroga, M.L Grossbeck, T. Yamamoto, J. Nucl. Mater., 307-311 (2002) 1595-1599.

PAPERS

1. N.J. Heo, T. Nagasaka, T. Muroga, and H. Matsui, Effect of impurity levels on precipitation behavior in the low-activation V-4Cr-4Ti alloys, Journal of Nuclear Materials, 307-311 (2002) 620-624.

2. N.J. Heo, T. Nagasaka, T. Muroga, A. Nishimura, K. Shinozaki, and N. Takeshita, Development of laser welding technology for vanadium and its alloys, J. of Plasma Fusion and Research (JPFR Series Vol. 5), in press

3. N.J. Heo, T. Nagasaka, T. Muroga, A. Nishimura, K. Shinozaki, and N. Takeshita, Metallurgical and mechanical properties of laser weldment for low activation V-4Cr-4Ti alloy, Fusion Engineering Design, 61-62 (2002) 749-755.

4. T. Nagasaka, N.J. Heo, T. Muroga, and M. Imamura, Examination of fabrication process parameters for improvement of low activation V-4Cr-4Ti alloy, Fusion Engineering Design, 61-62 (2002) 757-762.

5. N.J. Heo, T. Nagasaka, and T. Muroga, Recrystallization and precipitation behavior of the low activation V-4Cr-4Ti alloys after cold rolling, Journal of Nuclear Materials, accepted.

6. N.J. Heo, T. Nagasaka, T. Muroga, A. Nishimura, K. Shinozaki, and H. Watanabe, Mechanical properties of laser weldment of V-4Cr-4Ti alloy, Fusion Science and Technology, contributed.

PRESENTATIONS

1. N.J. Heo, T. Nagasaka, T. Muroga and H. Matsui, Recovery and recrystallization behavior of the reference high-purity low-activation V-Cr-Ti alloy (NIFS-HEAT-1) after cold rolling, The Japan Institute of Metal Fall Meeting, 2000, Nagoya, Japan.

2. N.J. Heo, T. Nagasaka, T. Muroga and H. Matsui, Recovery and recrystallization behavior of the reference high-purity low-activation V-Cr-Ti alloy (NIFS-HEAT-1) after cold rolling, Proceedings of the 5th IEA and JUPITER Joint Workshop on Vanadium Alloys for Fusion Application, 2000, Tokyo, Japan.

3. N.J. Heo, T. Nagasaka, T. Muroga and H. Matsui, Effect of impurity levels on precipitation behavior in the low-activation V-4Cr-4Ti alloys, The Japan Institute of Metal Spring Meeting, 2001, Tokyo, Japan.

4. N.J. Heo, T. Nagasaka, T. Muroga and H. Matsui, Effect of impurity levels on precipitation behavior in the low-activation V-4Cr-4Ti alloys, The 10th International Conference on Fusion Reactor Materials, 2001, Baden-Baden, Germany.

5. N.J. Heo, T. Nagasaka, T. Muroga, A. Nishimura, K. Shinozaki and N. Takeshita, Development of laser welding technology for vanadium and its alloys, The 12th International Toki Conference on Plasma Physics and Controlled Nuclear Fusion, 2001, Toki, Japan.

6. N.J. Heo, T. Nagasaka, T. Muroga, A. Nishimura, K. Shinozaki and N. Takeshita, Impact properties of laser weldment for low activation V-4Cr-4Ti alloy, The Japan Institute of Metal Spring Meeting, 2002, Tokyo, Japan.

7. N.J. Heo, T. Nagasaka, T. Muroga, A. Nishimura, K. Shinozaki and N. Takeshita, Metallurgical and mechanical properties of laser weldment for low activation V-4Cr-4Ti alloy, The 6th International Symposium on Fusion Nuclear Technology, 2002, San Diego, California, USA.

8. T. Nagasaka, N.J. Heo, T. Muroga, and M. Imamura, Examination of fabrication process parameters for improvement of low activation V-4Cr-4Ti alloy, The 6th

International Symposium on Fusion Nuclear Technology, 2002, San Diego, California, USA.

9. N.J. Heo, T. Nagasaka, T. Muroga, A. Nishimura, K. Shinozaki, and H. Watanabe, Development of laser welding technology for vanadium alloys, Japan Welding Society Spring Meeting, 2002, Tokyo, Japan.

10. N.J. Heo, T. Nagasaka, T. Muroga, A. Nishimura, K. Shinozaki, and H. Watanabe, Mechanical properties of laser weldment of V-4Cr-4Ti alloy, The 15th Technology of Fusion Energy (Embedded Topical Meeting of ANS Winter Meeting), 2002, Washington DC, USA.

ACKNOWLEDGEMENTS

I would like to express my best appreciation to Prof. Takeo Muroga, Prof. Arata Nishimura and Dr. Takuya Nagasaka of National Insititute for Fusion Science (NIFS) for helpful guidance and discussion on this study. Especially, it is my honor to thank Prof. Muroga for providing many opportunities for national and international presentations for me. I also extend my sincere thanks to other members of Fusion Engineering Research Center (FERC), NIFS for their many advices.

I am also thankful to Prof. Kenji Shinozaki of Hiroshima University for many discussions on this study and assistance in the YAG laser welding.

I also wish to acknowledge the helps of Prof. Hideki Matsui of Institute for Materials Research (IMR), Tohoku University for the button arc melting, chemical analysis and charpy test.

Thanks should also go to Prof. Hideo Watanabe of Research Institute for Applied Mechanics, Kyusyu University for TEM observations of the specimens.

The financial support by Tajimi-Nishi Rotary Club, International Rotary of Japan is gratefully acknowledged.

I am also grateful to Prof. C.Y. Kang, H.J Kim and other Professors of Department of Metallurgical Engineering, Pukyong National University (Korea) for many helps and advices. I am also thankful to alumni of Nagoya University.

Finally, I would like to express my appreciation to my parents, my sisters and brothers for supporting my doctoral course with endless love and consideration.